

Design, Fabrication, and Mechanical Property Analysis of 3D Nanoarchitected Materials

Thesis by

Lucas R. Meza

In Partial Fulfillment of the Requirements for the Degree of
Doctor of Philosophy



CALIFORNIA INSTITUTE OF TECHNOLOGY

Pasadena, California

2016

(Defended May 4, 2016)

© 2016

Lucas R. Meza

All Rights Reserved

Acknowledgements

Caltech is a truly remarkable institution, and I am lucky to have been a part of it. There are very few places that can offer the access to resources and opportunities I have been afforded here, and the people I've met throughout my time here have helped shape and build my identity both as a scientist and as a person. I am truly indebted to this place I've been privileged enough to call my home.

I would like to thank my advisor, Professor Julia Greer, for her enthusiastic support and guidance throughout my time at Caltech. The freedom she has given me to pursue the innumerable research projects I have worked on and the constant encouragement she has provided are what has allowed me to accomplish all that I have. Julia is the reason that I initially decided to come to Caltech, and I'm happy to say it's a decision I haven't looked back on.

I am extremely grateful to Professors Guruswami (Ravi) Ravichandran, Sergio Pellegrino and Dennis Kochmann both for agreeing to be on my thesis committee and for teaching the excellent classes that laid the groundwork for my knowledge of solid mechanics and my future research work. I am particularly grateful to Dennis for his research guidance throughout the number of collaborations we have had.

Thank you to both Robert Maaß and Dongchan Jang for being incredible research mentors and helping shape my early development as a researcher here. Thank you also to Frank Greer, Seok-Woo Lee, Satyajit Das, Alex Zelhofer, Nigel Clarke, and many others for being exceptional collaborators and helping make so much exciting work possible.

Thank you to all of my labmates and officemates: Wendy, Lauren, Rachel and Viki for always making the office a fun place to hang out and an interesting place to talk about research,

Alessandro, Ottman, Arturo and Carlos for the long research discussions we've had, Daryl, Ryan and Mike for their relentless entertainment, and to all the other members of the Greer group I've been lucky enough to get to know.

I would like to thank all the people who helped make so much of this work possible, including the excellent staff at the Kavli Nanoscience Institute, Nick Strandwitz and Fan Yang in the Lewis group, many members of the Atwater group, Carol Garland, and all the other people I've gotten help from over the years. The collaborative research environment engendered here at Caltech has been incredibly supportive, and much of what I have been able to do during my time here would not have been possible if so many people weren't so willing to help.

I have had the incredible opportunity to work with and mentor a number of outstanding students during my time here. Thank you David Lam, Andre Comella, Puikei Cheng, Kim Liu, and so many other undergraduate and high school students for all your hard work, and I wish you all the best of luck in your future careers.

Thanks to Brandon, Chengyun, Brock, and Hyun-Sik for their continued friendship and fun lunchtime discussions. Thanks to Mike for helping encourage me to come here and always being a good friend. Thanks to the whole RA group for always being fun to hang out with and for helping me to keep my sanity as an RA. And thanks to all of the people that I've met through soccer, rock climbing and ultimate for making my time here so much more enjoyable.

I'd like thank the whole of Blacker for taking me in and giving me a place to live for the last two years. Getting to know you all has been an incredible experience, and you really made the house feel like a home to me.

Thank you to my girlfriend Angelica for your patience and understanding in helping me through this process. I know it's been a long one, but it really means a lot to have you there for me. Thank you to my family whose continued support and encouragement has really helped motivate me through this process. While I may not admit it out loud, I've always been secretly happy when you get excited and want to show off my work, and it means a lot knowing that you're proud of me for it.

Lastly, I want to acknowledge the huge number of funding sources that have made this work possible: the Dow-Resnick Innovation Fund at Caltech, DARPA's Materials with Controlled Microstructure and Architecture program, the Army Research Office through the Institute for Collaborative Biotechnologies at Caltech, the Office of Naval Research, and the National Science Foundation.

Abstract

Recent developments in micro- and nanoscale 3D fabrication techniques have enabled the creation of materials with a controllable nanoarchitecture that can have structural features spanning 5 orders of magnitude from tens of nanometers to millimeters. These fabrication methods in conjunction with nanomaterial processing techniques permit a nearly unbounded design space through which new combinations of nanomaterials and architecture can be realized. In the course of this work, we designed, fabricated, and mechanically analyzed a wide range of nanoarchitected materials in the form of nanolattices made from polymer, composite, and hollow ceramic beams. Using a combination of two-photon lithography and atomic layer deposition, we fabricated samples with periodic and hierarchical architectures spanning densities over 4 orders of magnitude from $\rho = 0.3 - 300 \text{ kg/m}^3$ and with features as small as 5nm. Uniaxial compression and cyclic loading tests performed on different nanolattice topologies revealed a range of novel mechanical properties: the constituent nanoceramics used here have size-enhanced strengths that approach the theoretical limit of materials strength; hollow aluminum oxide (Al_2O_3) nanolattices exhibited ductile-like deformation and recovered nearly completely after compression to 50% strain when their wall thicknesses were reduced below 20nm due to the activation of shell buckling; hierarchical nanolattices exhibited enhanced recoverability and a near linear scaling of strength and stiffness with relative density, with $E \propto \bar{\rho}^{1.04}$ and $\sigma_y \propto \bar{\rho}^{1.17}$ for hollow Al_2O_3 samples; periodic rigid and non-rigid nanolattice topologies were tested and showed a nearly uniform scaling of strength and stiffness with relative density, marking a significant deviation from traditional theories on “bending” and “stretching” dominated cellular solids; and the mechanical behavior across all topologies was highly tunable and was observed to strongly correlate with the slenderness λ and the wall thickness-to-radius ratio t/a of the beams. These results demonstrate the potential of nanoarchitected materials to create new highly tunable mechanical metamaterials with previously unattainable properties.

Published Content

Chapter 2 has been adapted from:

- 1) D. Jang, L.R. Meza, F. Greer, & J.R. Greer, “Fabrication and Deformation of Three-Dimensional Hollow Ceramic Nanostructures”, *Nature Materials* **12**, 893-898 (2013), DOI: 10.1038/nmat3738

Contributions: Designed and fabricated samples, performed finite element analysis, analyzed data, and partially wrote manuscript.

- 2) L.R. Meza & J.R. Greer, “Mechanical Characterization of Hollow Ceramic Nanolattices” *Journal of Materials Science* **49**, 2496-2508 (2014), DOI: 10.1007/s10853-013-7945-x

Contributions: Designed and fabricated samples, conducted experiments, performed finite element analysis, derived analytical model, analyzed data, and wrote manuscript.

Chapter 3 has been adapted from:

- 3) L.R. Meza, S. Das, & J.R. Greer, “Strong, Lightweight, and Recoverable Three-Dimensional Ceramic Nanolattices” *Science* **345**, 1322-1326 (2014), DOI: 10.1126/science.1255908

Contributions: Designed and fabricated samples, conducted experiments, derived analytical model, analyzed data, and wrote manuscript.

Chapter 4 has been adapted, in part, from:

- 4) L.R. Meza, A.J. Zelhofer, N. Clarke, A.J. Mateos, D.M. Kochmann, & J.R. Greer. (2015) “Hierarchy in Three-Dimensional Architected Meta-materials Brings Resilience” *Proceedings of the National Academy of Sciences* **112**, 11502-11507 (2015), DOI: 10.1073/pnas.1509120112

Contributions: Designed and fabricated samples, conducted experiments, analyzed data, and wrote manuscript.

Table of Contents

Copyright Page.....	ii
Acknowledgements.....	iii
Abstract.....	vi
Published Content.....	vii
List of Figures.....	xi
List of Tables.....	xiii
Chapter 1: Introduction to Nanoarchitected Materials.....	1
1.1. Overview of Architected Materials.....	1
1.1.1. What is an Architected Material?.....	1
1.1.2. Recent Developments in Architected Material Fabrication and Design.....	1
1.1.3. Hierarchical Architectures.....	2
1.2. Nature’s Architected Materials.....	3
1.3. Size Effects in Nanomaterials.....	3
1.4. Architecture and Mechanical Properties.....	4
1.5. Outline and Objectives.....	6
Chapter 2: Mechanical Characterization of Hollow Ceramic Nanolattices.....	7
2.1. Chapter Summary.....	7
2.2. 3D Nanolattice Design and Fabrication.....	8
2.3. Experimental Setup.....	10
2.4. Monotonic Compression of a Single Unit Cell.....	11
2.4.1. Experimental Results.....	11
2.4.2. Finite Element Simulation.....	12
2.4.3. Analytical Modeling.....	15
2.4.4. Comparison between Experimental, Simulation, and Modeling Results.....	20
2.5. Cyclic Compression of a Single Unit Cell.....	21
2.6. Monotonic Compression of a Full Nanolattice.....	23
2.6.1. Experimental Results.....	23
2.6.2. Cellular Solid Model.....	24
2.6.3. Comparison between Experimental and Modeling Results.....	25

2.7. Understanding Material Properties – Titanium Nitride.....	26
2.7.1. Experimental Results and Characterization	26
2.7.2. Theoretical Material Model.....	28
Chapter 3: Strong, Lightweight, and Recoverable 3D Ceramic Nanolattices	31
3.1. Chapter Summary.....	31
3.2. Al ₂ O ₃ Nanolattice Structure and Fabrication	31
3.3. Nanolattice Compression Experiments	34
3.3.1. Experimental Setup and Data Analysis	34
3.4.2. “Thick-walled” Structure Compression	35
3.4.3. “Thin-walled” Structure Compression	36
3.4. Failure and Recoverability Model Formulation	37
3.5. Comparison between Experimental Results and Failure Model	41
3.6. Discussion on Recoverability	42
3.7. Strength and Stiffness Scaling with Density	44
Chapter 4: Hierarchical 3D Nanoarchitected Materials.....	46
4.1. Chapter Summary.....	46
4.2. Hierarchical Nanolattice Design and Fabrication	47
4.3. Experimental Setup	49
4.4. Hierarchical Nanolattice Deformation, Failure, and Recoverability.....	49
4.4.1. Hierarchical Slenderness Ratios	51
4.4.2. 2 nd Order Polymer Samples	52
4.4.3. 2 nd Order Composite Samples	54
4.4.4. 2 nd Order Hollow Al ₂ O ₃ Samples	56
4.4.5. 3 rd Order Samples	59
4.4.6. Discussion on Recoverability	60
4.5. Strength and Stiffness Scaling with Density	61
4.5.1. Experimental Results.....	61
4.5.2. Computational Multiscale Modeling.....	63
4.5.3. Comparison between Experimental Results and Multiscale Modeling.....	64
4.5.4. The Role of Imperfections.....	66
4.5.5. Constituent Material Properties.....	67

Chapter 5: Mechanical Performance of Rigid vs. Non-Rigid Nanolattice Topologies	69
5.1. Chapter Summary	69
5.2. Defining Rigidity of a Structure	69
5.3. Design of Rigid and Non-Rigid Nanolattice Topologies	72
5.4. Deformation Behavior and Transition between Failure Modes	74
5.4.1. Polymer Nanolattices	74
5.4.2. Hollow Al ₂ O ₃ Nanolattices	78
5.4.3 Discussion on Recoverability	80
5.5. Strength and Stiffness Scaling with Relative Density	85
5.5.1. Strength and Stiffness of Rigid and Non-Rigid Topologies	85
5.5.2. The Effect of Angle Changes on Strength and Stiffness	91
5.5.3. The Role of Imperfections – Missing Beams	93
5.5.4. The Role of Imperfections – Offset Nodes	96
Chapter 6: Summary and Outlook	99
Appendices	102
Appendix A. Nanolattice Design Methodologies	102
Periodic Lattice Design	102
Hierarchical Lattice Design	104
Layer-by-Layer Design	105
Appendix B. Analytic Calculation of Relative Density	108
Appendix C. Data Analysis Methods	111
Appendix D. Slenderness Ratio Formulations	113
1 st Order Beam	114
2 nd Order Octahedron Beam	115
2 nd Order Octet Beam	116
3 rd Order Octahedron Beam	117
Appendix E. Data Tables	120
Appendix F. Movies	128
References	132

List of Figures

Figure 1: Structure and Design of TiN nanolattices.	8
Figure 2: Nanolattice fabrication process.	9
Figure 3: Monotonic compression of a single unit cell.....	11
Figure 4: Unit cell design and modeling setup.	13
Figure 5: Finite element analysis of a 4-bar simplified unit cell.	15
Figure 6: Cyclic compression of unit cell.	22
Figure 7: Monotonic compression of a full nanolattice.	24
Figure 8: Schematic representation of theoretical strength.....	30
Figure 9: Design and microstructure of octet-truss alumina nanolattices.....	32
Figure 10: Illustration of the nanolattice etching process.	34
Figure 11: Representative stress-strain curves of nanolattice compression experiments.	35
Figure 12: Compression experiments on thick- and thin-walled nanolattices.....	37
Figure 13: Simplified representation of stress state in nanolattices.....	40
Figure 14: Mechanical tests on hollow octet-truss samples with varying t and ρ	42
Figure 15: Compression of a thin-walled octet-truss nanolattice to high strain.	44
Figure 16: Strength and stiffness versus density of alumina nanolattices.	45
Figure 17: CAD and SEM images of hierarchical nanolattices.....	48
Figure 18: Compression of 2 nd order octahedron-of-octet half-cells.	50
Figure 19: Compression of 3 rd order octahedron-of-octahedra-of-octahedra half-cells.	51
Figure 20: All compression experiments on 2 nd order polymer half-cells.....	54
Figure 21: All compression experiments on 2 nd order composite half-cells.....	56
Figure 22: All compression experiments on 2 nd order hollow Al ₂ O ₃ half-cells.	57
Figure 23: All compression experiments on 2 nd order full-lattices.....	59
Figure 24: All compression experiments on 3 rd order half-cells.....	60
Figure 25: Comprehensive data plot of all tested hierarchical nanolattices.	63
Figure 26: Model flowchart showing truss and refined model generation.	64
Figure 27: Representative stress-strain curves for polymer pillar compression.	68
Figure 28: Examples of rigid and non-rigid structures	71
Figure 29: Rigid and non-rigid nanolattice topologies.	73

Figure 30: Stress-strain curves of different polymer nanolattice topologies.	77
Figure 31: Stress-strain curves of different hollow Al ₂ O ₃ nanolattice topologies.	79
Figure 32: Recoverability of polymer nanolattice topologies.	81
Figure 33: Recoverability of hollow Al ₂ O ₃ nanolattice topologies.	83
Figure 34: Compression of various polymer and thin-walled Al ₂ O ₃ nanolattice topologies.	84
Figure 35: Strength and stiffness vs. density of different nanolattice topologies.	87
Figure 36: Stiffness of experimental data and FEM data for polymer octahedron nanolattices. ...	90
Figure 37: Strength and stiffness vs. density of 3D Kagome lattices with varying angle.	93
Figure 38: Stress-strain data of polymer octet-trusses with missing beams	94
Figure 39: Strength and modulus of polymer octet-trusses with missing beams	95
Figure 40: Stress-strain data of offset-node octet-trusses.	97
Figure 41: Strength and modulus of offset-node polymer octet-trusses.	98
Figure 42: Single Unit Cell Designs.	102
Figure 43: Periodic Lattice Fabrication - Tessellation.	103
Figure 44: Periodic Lattice Fabrication – “Layer-by-Layer”.	103
Figure 45: Hierarchical nanolattice design process.	105
Figure 46: Hierarchical nanolattice unit cells.	105
Figure 47: Layer-by-layer Nanolattice Fabrication.	106
Figure 48: Writing Circular Beams with Elliptical Voxels.	107
Figure 49: Beam Nodal Interference.	108
Figure 50: Octahedron Unit Cell Relative Density.	110
Figure 51: Yield Strength and Young’s Modulus Measurement.	111
Figure 52: Spring Correction for a Highly Compliant Sample.	112
Figure 53: Hierarchical cross-sections.	119

List of Tables

Table 1: Hierarchical nanolattice scaling relationships.	62
Table 2: Scaling and proportionality constants for different nanolattice topologies.	86
Table 3: Hollow Al ₂ O ₃ Octet-truss Data.....	120
Table 4: Hollow Al ₂ O ₃ Cuboctahedron Data.....	121
Table 5: Hollow Al ₂ O ₃ 3D Kagome Data.....	122
Table 6: Hollow Al ₂ O ₃ Tetrakaidecahedron Data	123
Table 7: Polymer Nanolattice Data.....	124
Table 8: Missing Bar Polymer Octet-truss Data.	125
Table 9: Offset Node Polymer Octet-truss Data.	125
Table 10: 2 nd Order Hierarchical Half-cell Data.....	126
Table 11: 3 rd Order Hierarchical Half-cell Data	127
Table 12: 2 nd Order Hierarchical Nanolattice Data.....	127

Chapter 1: Introduction to Nanoarchitected Materials

1.1. Overview of Architected Materials

1.1.1. What is an Architected Material?

Architected materials are “combinations of two or more materials, or of materials and space, configured in such a way as to have attributes not offered by any one material alone” (1). The guiding philosophy behind architected materials is that combinations of material and architecture can give rise to new materials with previously unattainable properties. Architecture has long been used to enhance the performance of engineering materials; foams are used to make lightweight materials with a range of mechanical properties (2), composites can have mechanical properties like strength and toughness well exceeding that of their constituents (3), and honeycomb sandwich panels maintain very high stiffness at low weights (4). All these materials have a controllable architecture that gives them properties superior to their bulk constituents. Traditionally, architected materials use simple design methodologies like layering, sandwiching, corrugating, and adding porosity as a means to control their properties (5, 6).

1.1.2. Recent Developments in Architected Material Fabrication and Design

The rapid expansion of 3D manufacturing technologies over the past few decades has enabled the creation of complex structures with features that can span across multiple length scales. The most interesting architected material fabrication techniques are those that enable fabrication at the micro- and nanoscale; these include self-propagating photopolymer waveguides (7), microstereolithography (8), two-photon lithography (9), and holographic lithography (10). These techniques are often used in combination with other advanced manufacturing techniques

and have led to the creation of many new materials with unprecedented levels of performance like strong and ultralight metal- and ceramic-based microlattices (11–13), nanolattices with features sufficiently in the nanometer regime to capitalize on size-affected material properties (14–16), and light weight meso-lattices with strengths in excess of their bulk constituents (17). They have also provided the unique opportunity to create meta-materials with previously unobtainable properties like negative Poisson’s ratios (18, 19), near infinite bulk-to-shear modulus ratios (20, 21), and negative effective mass-density (22). Some other notable examples of 3D architected materials like carbon nanotube foams (23–25), graphene foams (26), inverse opals (27, 28), and biomimetic composites (29, 30) are also being actively pursued thanks to advances in nanoscale fabrication and metrology techniques.

1.1.3. Hierarchical Architectures

Hierarchical architectures are those with distinct structural features that span multiple length scales (31). This hierarchy can manifest in a self-similar manner, e.g. a lattice structure with beams made of lattices, or with discrete hierarchical elements, e.g. a lattice with composite beams. Hierarchically engineered structures have long been used in architecture, with notable examples found in the Eiffel tower and the Garabit viaduct (32); today hierarchy is seen commonly in construction cranes and building scaffolding. Both natural and engineered structures use the concept of hierarchical design to minimize material use while optimizing structural integrity. Design principles and theories describing hierarchical structural materials exist (31, 33), and macroscopic 2nd and 3rd order 2D cellular solids, like honeycombs (34, 35) and corrugated core sandwich panels (36–38), have been designed and tested experimentally. Theories that describe the design and optimization of 3D hierarchical trusses have been proposed (39–42), but until recently their fabrication presented a challenge.

1.2. Nature's Architected Materials

Natural materials are frequently used as a source of inspiration for the design of architected materials; many have evolved to have novel mechanical properties and enhanced mechanical performance using simple materials like ceramics – such as hydroxyapatite, silica, and aragonite – and biopolymers such as collagen, chitin, keratin, and elastin. Hard biological materials such as bone, antler, shell, nacre, and wood are known to have exceptional hardness and toughness and have been reported to have higher fracture toughness than man-made composites of the same composition (43–52). Porous hard biological materials such as sea sponges, diatoms, and radiolarians are simultaneously stiff, tough, and lightweight (53–58), properties that have been shown to contribute to their effective defense against predators.

The novel combination of mechanical properties in natural materials is thought to be achieved through their hierarchical design (44). Natural materials have characteristic dimensions that can span from nanometers to micrometers to centimeters and larger. Their structure can take on periodic or stochastic arrangements, often with ordered and disordered phases across different levels of hierarchy. Nature's motivation for using these carefully chosen discrete length scales may stem from the advantageous properties offered by the interplay of individual biological constituents. Because hierarchy is so ubiquitous in the natural world, characterizing it, understanding its origins, and discovering its role in enhancing material properties can greatly benefit the design of new advanced materials.

1.3. Size Effects in Nanomaterials

The enhanced mechanical performance of natural materials is often attributed to features at the lowest level of hierarchy, normally on the order of nanometers. It is well known that the

mechanical properties of materials undergo a size-affected transition when their ultimate dimensions are reduced to sufficiently small length scales. These size-affected properties include the power-law strengthening of single-crystalline metals (59, 60), suppression of catastrophic failure in metallic glasses (61, 62), Weibull strengthening in ceramics (63, 64), and enhanced toughness in brittle materials (65, 66). When a structure contains micro- and nanoscale components, as is the case in hard biological materials, size-dependent mechanical properties of constituent materials may play a key role in the enhancement of the overall strength, stiffness and fracture resistance, and need to be incorporated into models to accurately predict the structural response.

The efficient design of architected materials must incorporate knowledge of how materials will behave across different length scales and how different mechanical behaviors will enhance or detract from the overall performance. For example, many bulk monolithic materials with high strength-to-weight (σ_{ys}/ρ) and stiffness-to-weight (E/ρ) ratios – such as technical ceramics, diamond, and metallic glasses – have excellent potential for use as strong and lightweight structural materials but are suboptimal because of their low toughness and brittle, flaw-sensitive nature (67–70). Metals, which generally have high strength and toughness, can become insensitive to flaws at the nanoscale (71) but they can also become weaker when their dimensions are significantly reduced depending on their microstructure (72). A full characterization and understanding of a constituent material's properties are crucial for the design of advanced architected materials.

1.4. Architecture and Mechanical Properties

Bulk mechanical properties of cellular solids, i.e. foams and lattices, have been studied in great detail over a number of decades (2, 6, 56, 73–76). The mechanical properties of cellular

solids are generally characterized by their constituent material properties, geometry, and relative density ($\bar{\rho} = \rho/\rho_s$). Two principal mechanical properties, Young's modulus (E) and yield strength (σ_y), are known to scale with the relative density as

$$E \propto E_s \bar{\rho}^m \quad (1)$$

$$\sigma_y \propto \sigma_{ys} \bar{\rho}^n \quad (2)$$

Here, E_s and σ_{ys} are the Young's modulus and the yield strength of the constituent material, and the exponents m and n are defined by the cell geometry (2). Classical theories of the mechanics of cellular solids generally assume that the constituent material properties are scale-invariant, meaning that any structures with the same geometry and material composition will have the same relative moduli and strengths regardless of their absolute size.

To predict the mechanical behavior of architected materials, it is first necessary to understand the role of architecture in governing mechanical properties. Traditional cellular-solids theories state that there are two main classes of geometries that can be designed to elicit different mechanical responses: those that are bending-dominated and those that are stretching-dominated. Stretching-dominated structures are those that have no intrinsic mechanisms (77) that allow for bending deformation, and as a result their strength and stiffness will scale linearly with relative density as $\sigma_y \propto \bar{\rho}$ and $E \propto \bar{\rho}$ (73, 74, 78). Bending-dominated structures are those with deformation mechanisms that allow for bending of beams, and their strength and modulus will scale as $\sigma_y \propto \bar{\rho}^{1.5}$ and $E \sim \bar{\rho}^2$ for periodic structures or $E \sim \bar{\rho}^3$ for stochastic structures, respectively (74). A more in-depth discussion on mechanisms and rigidity can be found in Section 5.2.

1.5. Outline and Objectives

The focus of this dissertation is on developments that we have made in the field of nanoarchitected materials over the past few years. In the following sections, it is shown that nanomaterials with advantageous properties like high strength and flaw tolerance can be used in nanoarchitected materials in the form of nanolattices. These have highly tunable mechanical properties, and it is shown that shell buckling can be used to make nanolattices that are ductile and recoverable even when made from intrinsically brittle ceramics. The addition of hierarchy to nanolattice design is demonstrated to enhance mechanical properties like strength, stiffness, and recoverability. Finally, the mechanical properties of rigid and non-rigid nanolattice topologies are examined and shown to have performance that significantly deviates from the predictions of classical cellular solids theories.

The goal of this dissertation is to provide a framework for the design and fabrication of new nanoarchitected materials. There is currently a practically unbounded design space through which new architected materials can be created, but there are very few guiding principles for the design of new nanoarchitectures. I believe the developments in nanoarchitected material design, fabrication, and mechanical properties shown in this work can provide guidance for the further development of the field.

Chapter 2: Mechanical Characterization of Hollow Ceramic Nanolattices

2.1. Chapter Summary

This work presents the development of a multi-step nanofabrication process to create three-dimensional hollow titanium nitride (TiN) nanolattices. The relative density of the samples is on the order of $\bar{\rho} = 0.0136$ (similar to aerogels) and their characteristic material length scales span from tens of nanometers (wall thickness) to several microns (tube diameter) to tens of microns (unit cell) to over $100 \mu m$ for the entire structure. In-situ nanomechanical experiments and finite element simulations revealed the constituent TiN to have a remarkably high tensile yield strength of 1.75 GPa , which represents close to half of the theoretical strength of TiN. This high tensile strength, coupled with a lateral-torsional buckling instability observed during the uniaxial compression of a single unit cell, gave rise to a hyperelastic deformation response in the beams. Compression experiments performed on full nanolattices gave a structural modulus of $E = 61.8 \text{ MPa}$ and yield strength of $\sigma_y = 0.873 \text{ MPa}$.

The attainment of exceptionally high strength in TiN is attributed to the low probability of having pre-existing flaws in nanosized solids. Failure in nanoscale ceramics initiates at a weakest link, which is determined by the competing effects of stress concentrators at surface imperfections and local stresses within the microstructural landscape. These findings may offer the potential of applying hierarchical design principles offered by hard biological organisms to creating damage-tolerant lightweight engineering materials.

2.2. 3D Nanolattice Design and Fabrication

The geometry used in these experiments is derived from a series of tessellated regular octahedron unit cells connected at their vertices (Figure 1d, e, h, & i). An octahedron is an inherently rigid geometry, which has no collapse mechanisms (74, 77). The octahedra in the nanolattices were arranged into a structure with a relatively low connectivity ($Z = 8$) and formed a non-rigid structure with periodic collapse mechanisms (74). Each octahedron is composed of approximately $7 \mu\text{m}$ long hollow struts with vertically oriented elliptical cross-sections and wall thicknesses of 75 nm (see inset in Figure 1i). The resulting structure is an approximately $100 \mu\text{m}$ cube composed of a $10 \times 10 \times 10$ array of octahedron unit cells.

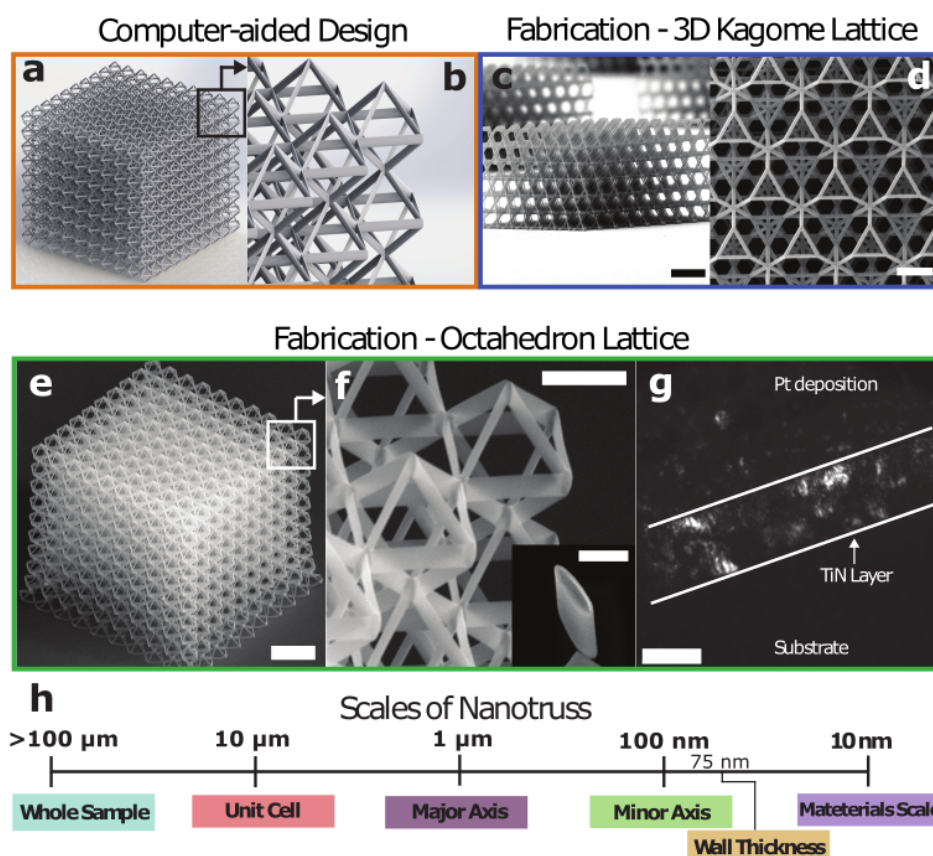


Figure 1: Structure and Design of TiN nanolattices.

a,b) Computer-aided design of octahedron nanolattices. c,d) SEM image of a fabricated nanolattice with a 3D Kagome unit cell. e-g) SEM (e, f) and transmission electron microscope dark-field (g) images of an engineered hollow nanolattice synthesized with TiN. The inset in f shows the cross-section of a strut. h) Schematic representation of the relevant dimensions of such fabricated nanolattices. Scale bars: $20 \mu\text{m}$ (e), $5 \mu\text{m}$ (c,d), $1 \mu\text{m}$ (inset of f), 20 nm (g).

Nanolattices were created using a multi-step negative pattern fabrication process involving direct laser writing (DLW), two-photon lithography (TPL), atomic layer deposition (ALD), and O_2 plasma etching (Figure 2). A polymer scaffold was fabricated through a TPL DLW process in IP-Dip 780 photoresist with a speed of $50 \mu m s^{-1}$ and laser power of 10 mW using the Photonic Professional DLW system (Nanoscribe). This scaffold was conformally coated with TiN using a plasma enhanced ALD process in the Oxford OpAL ALD system (Oxfordshire, UK). The deposition was performed by sequentially cycling through the following steps: flowing the reactant dose of titanium tetrachloride ($TiCl_4$) precursor for 30 ms, purging the system for 5 s, plasma treatment with an N_2/H_2 gas mixture (25 sccm/25 sccm) for 10 s, and purging the system for an additional 5 s. This process was repeated until a 75 nm thick layer was deposited. The internal polymer was then exposed using focused ion beam (FIB) milling in the FEI Nova 200 NanoLab and etched out in a barrel oxygen plasma etcher for 3 h under 100 W and 300 sccm oxygen flow, leaving behind a hollow truss structure. (Figure 1f, g: 3D Kagome unit cell, Figure 1h, i: octahedron unit cell).

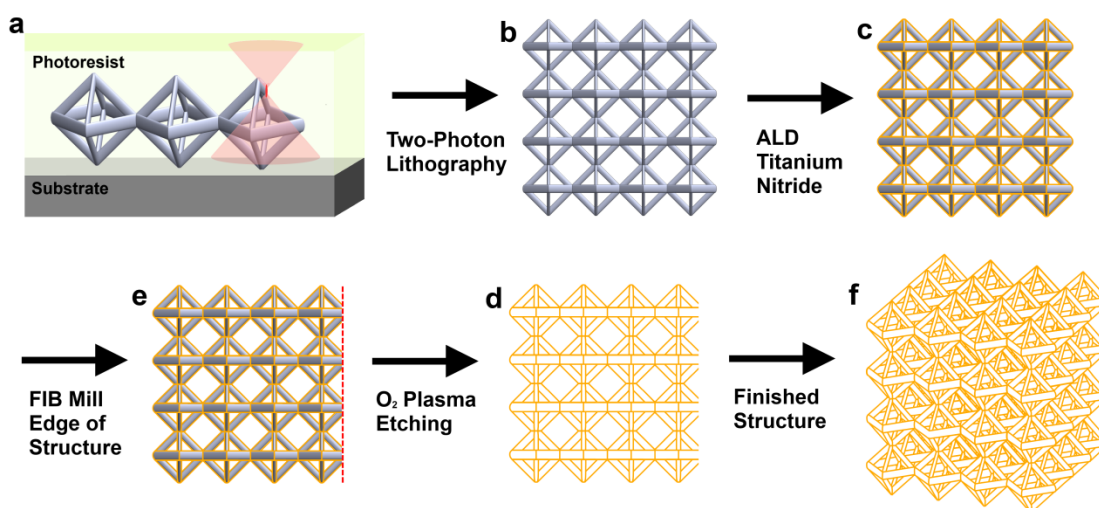


Figure 2: Nanolattice fabrication process.

a, b) Schematic representation of the writing process of the lattice unit cells using two-photon lithography direct laser writing. c) Structure is coated using an atomic layer deposition (ALD) process. d) One edge of the sample is milled using a focused ion beam (FIB) to expose the polymer. e) The internal polymer is etched away using an O_2 plasma. f) Final product: a hollow tube nanolattice.

Careful imaging of the fabricated structures revealed that the truss beams had elliptical cross-sections with a major axis of $a = 600 \text{ nm}$, a minor axis of $b = 134 \text{ nm}$, and a thickness $t = 75 \text{ nm}$. The characteristic nanostructural length scale of TiN, represented by its grain size, was between 10 and 20 nm , as can be seen in the dark-field transmission electron microscope image in Figure 1j. Figure 1 also contains scale bars showing all relevant sizes within these structures. The effective length of the beams was taken to be $L = 6.5 \mu\text{m}$ based on the geometry of the unit cell. The modulus of elasticity used was $E = 98 \text{ GPa}$, which was approximated by matching the stiffness calculated through the FEM simulations with that of the experiments. When this modulus was taken with a Poisson's ratio of $\nu = 0.295$ for titanium nitride, the shear modulus of the beam was calculated to be $G = 37.8 \text{ GPa}$.

2.3. Experimental Setup

Individual unit cells and the full nanolattice structures were quasi-statically compressed to failure in an in-situ nanomechanical testing instrument InSEM (Nanomechanics, Inc., Tennessee) previously referred to as SEMentor (see (59) for a specification of the instrument). Individual unit cells were compressed using a flat punch tip by applying a load at their apex along their vertical axis (see Figure 3) at a constant prescribed displacement rate of 10 nm s^{-1} ; cyclic experiments consisted of 11 loadings to total displacements (beam deformation + medial node deflection) of 350 nm followed by unloading to 10% of the maximum load in the previous cycle. Full structures were compressed using a flat punch tip at 250 nm s^{-1} also along their vertical axis. Before the tests, the instrument was stabilized for at least 12 h to minimize thermal drift. The typical thermal drift rate of this instrument is below 0.05 nm s^{-1} , which would contribute less than 0.5% to the total displacement.

2.4. Monotonic Compression of a Single Unit Cell

2.4.1. Experimental Results

Figure 3 shows the results of in-situ monotonic loading experiments on a single octahedron unit cell of the fabricated hollow nanolattice (Movie 1). The load-displacement curve for monotonic loading (Figure 3f) shows that the sample deformed elastically until the onset of nonlinearity (indicated by the arrow) and subsequently failed at a maximum load of $\sim 150 \mu\text{N}$ (marked by II). Figure 3e shows that the final axial displacement of the structure was roughly 420 nm , which includes both the compression of the upper four beams and the deflection of the surrounding structure. This load-displacement data was subsequently corrected to only account for the vertical compression of the upper four beams, measured to be approximately 200 nm based on in-situ SEM video frames. In the correction, it was assumed that the displacement of the surrounding structure remained in the linear elastic regime. This net displacement of the upper beams was used as the boundary condition in the simplified four-beam model in the finite-element analysis.

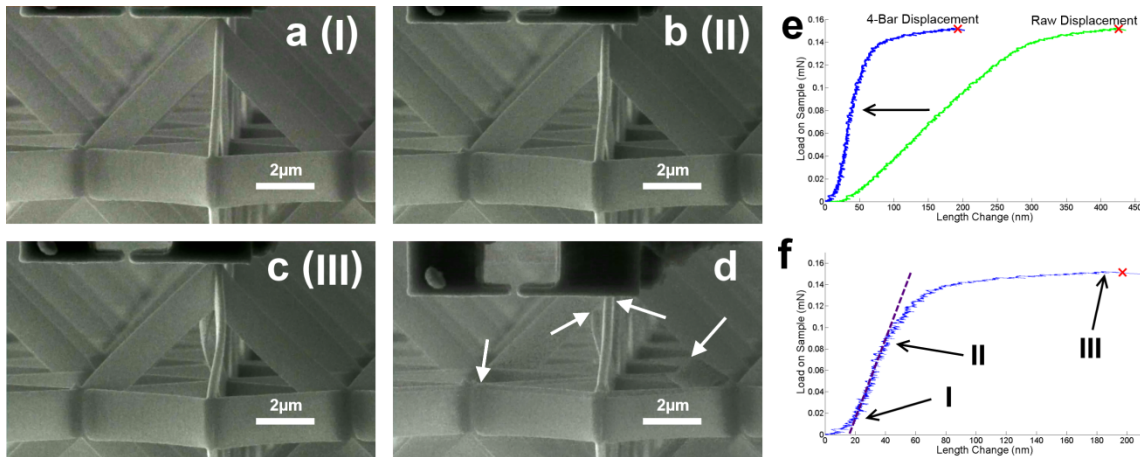


Figure 3: Monotonic compression of a single unit cell.

a–c) SEM images captured during the monotonic compression experiment, showing the progressive buckling of the unit cell. These snapshots are correlated to positions I, II, and III in the load–displacement curve in f. d) The arrows shown here point to local fracture points. It should be noted that the fracture positions closely match the stress concentrations seen in the FEM simulations (Figure 5). e) Load–displacement data is corrected to only account for the deflection of the upper 4 bars of the unit cell. The red x indicates the point of failure. f) Zoom in of the load–displacement plot showing the initial linear behavior and subsequent deviation from linearity.

The SEM images in Figure 3a-d depict the deformation morphology evolution during the experiment: Figure 3a corresponds to point I in the load–displacement data shown in Figure 3f and depicts the initial structure before any load was applied; Figure 3b corresponds to II, the point of maximum applied load; and Figure 3c corresponds to III, the point after failure. These images show that the deformation was accommodated mostly by bending and twisting of the diagonal truss members until the unit cell failed catastrophically at the nodes and along the mid-sections of the struts, noted by the arrows in Figure 3d. There was a notable deviation from linear behavior in the load-displacement data, as is indicated in Figure 3f. In-situ video analysis confirmed that this deviation likely coincides with the initiation of lateral-torsional buckling in the struts.

2.4.2. Finite Element Simulation

FEM simulations of the uniaxial compression of the top four beams of a single unit cell were performed in the finite element software ABAQUS. A non-linear elastic geometry solver was implemented in the simulations to account for the significant deflection of the beams. A linear elastic solver would have been sufficient to model the stress and deformation of the beams up to the point of buckling but would have been unable to capture the elastic instability and the large post-buckling deformation. The structure was modeled using the CAD program SolidWorks to obtain a geometry that precisely reflected that of the real structure. A simplified model of the unit cell consisting of only the upper four beams was used in order to better isolate the beam buckling response (Figure 4a, b) and to create a better analog to the analytical buckling model. All four beams were modeled to ensure that the resulting behavior was due to structural interactions and not to any imposed symmetry boundary conditions.

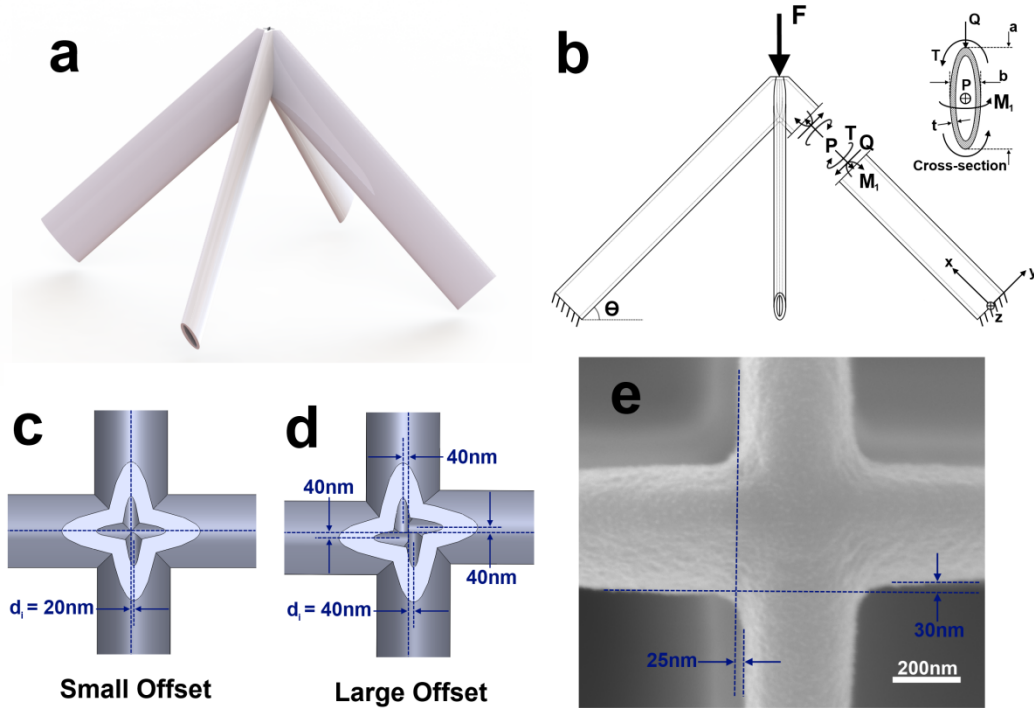


Figure 4: Unit cell design and modeling setup.

a) Computer-aided design of the simplified 4-bar structure used in FEM simulations. b) Diagram showing the force and moment balance on the simplified 4-bar unit cell. c, d) Computer-aided design of 20- and 40-nm offset structures tested in FEM simulations. e) SEM top view of actual unit cell showing the offset.

A rigid boundary condition was applied to the lower end of each of the four beams of the unit cell to simplify the FEM model (Figure 4b). A stiff elastic boundary condition would most accurately represent the unit cell, but it is difficult to determine the exact stiffness of the lower boundary due to the complex geometry and nodal connectivity. Instead, an FEM model of a full unit cell was made and tested for the sake of validating the simplified model, and the buckling response and stress concentrations were found to be nearly identical, giving validation to both the simplified unit cell and the fixed lower boundary. Only the results of the simplified unit cell are shown here for the sake of isolating the behavior of the beams in buckling.

A displacement boundary condition was applied to the top face of the structure to match the experimental conditions. No lateral constraint was placed on the top face, so the structure was free to translate and rotate about the central node. A tetrahedral mesh was used to

accommodate the complex geometry of the unit cell. The mesh was manually refined until the maximum stresses observed in the structure had fully converged at a final average mesh density of 400,000 *elements* μm^{-3} , with a higher concentration of elements toward the central node of the structure.

To explore the role that imperfections in the geometry of the unit cell have on the resulting deformation and to better mimic the geometry of the actual unit cell (Figure 4e), a number of different beam models with varying degrees of offset in the central node of the structure were created and compressed using a non-linear elastic FEM solver in ABAQUS. First, an ideal beam model with no offset in the central node of the structure was tested. The resulting deformation was linear and did not reproduce the lateral deflection seen in the experiments. Several beam models with systematically varying degrees of central offset were then created in an attempt to better match the actual geometry of the structure (Figure 4c-e). In the deformation response of these offset FEM models, the beams first displayed a linear elastic behavior that continued up to a displacement of 30 – 40 *nm* and then rapidly began to twist and bend (Figure 5), which very closely matched the behavior observed experimentally. Exploring a variety of beams with systematically varying degrees of offset in the central node of the structure revealed that any degree of offset qualitatively reproduced an identical bending and twisting response. The final deformed state of the structure and the final stresses in the beams were similar for the entire array of central offsets used, which ranged from one tube with a 20 *nm* offset to four tubes each with a 40 *nm* offset.

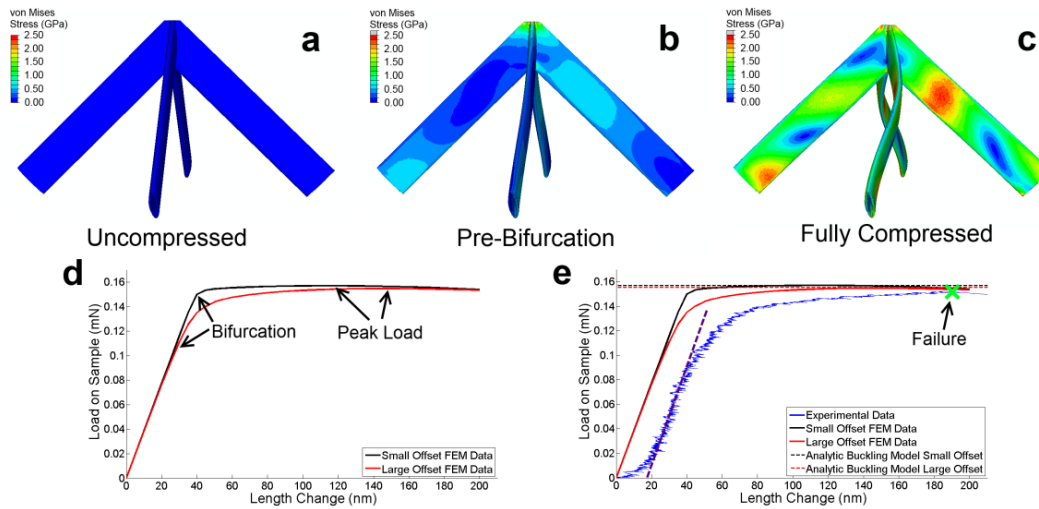


Figure 5: Finite element analysis of a 4-bar simplified unit cell.

a) Uncompressed FEM model of a 4-bar structure. b) 4-bar structure under compression before the initiation of buckling. This corresponds to the bifurcation point in d. c) Fully compressed 4-bar structure showing the full extent of deflection. This corresponds to the end of the FEM load displacement curve. d) The load displacement response of the FEM simulations on the small and large-offset beams. e) Fully overlaid unit cell compression results showing experimental, FEM, and analytic data. The green X indicates the point of failure.

The vertical reaction force, defined here as the sum of the forces on the nodes at the top face of the structure, was measured for different beam models. As the degree of offset in the central nodes became greater, it was observed that the onset of non-linear behavior occurred at a lower load (Figure 5d). The resulting load-displacement data for two structures, one with a 20 nm offset of a single beam (small-offset) and one with a 40 nm offset of all of the beams (large-offset), is presented alongside the experimental data (Figure 5e). The critical load at which the bifurcation occurred was found to be $F = 0.152 \text{ mN}$ in the small-offset beam and $F = 0.135 \text{ mN}$ for the large-offset beam. The peak load in the small-offset beam was $F_{max} = 0.157 \text{ mN}$ and $F_{max} = 0.154 \text{ m}$ for the large-offset beam.

2.4.3. Analytical Modeling

To capture the physical foundation for the observed deformation response, it is helpful to define and to quantify the resultant forces and moments acting on individual beams. The analysis here is done using the same four beam structure that is used in the FEM simulations and with identical boundary conditions. The only external load acting on the structure is the vertical force

applied to the top face (F). In a pin jointed structure, this force is evenly distributed among the four beams and can be expressed by:

$$P = \frac{F}{4 \sin(\theta)} \quad (3)$$

Here, F is the vertical load on the unit cell, P is the resolved axial load in the beams, and $\theta = 45^\circ$ is the angle between the beams and the plane normal to the loading direction (Figure 4b). In the idealized pin jointed structure with no offset at the central node, the only resulting load on a beam is this axial load. In the actual structure, the fixed boundary condition on the lower face of the beam causes it to undergo a vertical bending following a displacement condition on the top face that is proportional to its axial deflection. A displacement equation that accurately predicts the actual beam deflection can be found using classical beam bending models (79), as can the moment (M_2) and shear force (Q). This shear force and moment play a minimal role in the final deformation, so their derivation is omitted here.

In an ideal structure, the axial load and the bending moment are the only resultant forces that act on the beams. Any imperfection in the beams or misalignment between the beams will lead to an additional torsional moment that acts at the central node of the structure. It is reasonable to assume that this moment M is generated solely by a misalignment in the central node of the structure and can therefore be approximated by multiplying the horizontal component of the axial load in the beams by the sum of the offset of each of the beams:

$$M = \frac{P}{\tan(\theta)} \sum_{i=1}^4 d_i \quad (4)$$

This moment can then be taken and resolved into each of the beams as a bending moment and a torsional moment as

$$M_1 = M \cos(\theta) = \frac{P \cos^2(\theta)}{\sin(\theta)} \sum_{i=1}^4 d_i \quad (5)$$

$$T = M \sin(\theta) = P \cos(\theta) \sum_{i=1}^4 d_i \quad (6)$$

It is important to impose proper boundary conditions for the deformation in this direction of the beam. The lower end of the beam was assumed to be rigid. If the unit cell were perfect, the symmetry of the unit cell would force the upper node to remain in the center of the structure. The deformed structure shown in Figure 3c and Figure 5c demonstrates that the beams were able to pivot about the central node. While all of the beams in the structure provide some torsional resistance to buckling, due to the symmetry of the beam buckling, the effect is minimal. Therefore, the top node is assumed to have a pinned boundary condition, making the beam deflection governed by a fixed-pinned boundary condition. This is a critical consideration in calculating the overall strength of the structure.

Experimental and computational observations suggest that a buckling instability is the cause of the observed deflection of the beams. The complex loading and boundary conditions render a simple uniaxial buckling model incapable of characterizing the deformation of nanolattices observed here. A fundamental set of coupled differential equations, defined by (80), is used to characterize the deflection.

$$EI_y \frac{d^4 u}{dx^4} + P \frac{d^2 u}{dx^2} - M_1 \frac{d^2 \phi}{dz^2} = 0 \quad (7)$$

$$EI_z \frac{d^4 v}{dx^4} + P \frac{d^2 v}{dx^2} + M_2 \frac{d^2 \phi}{dz^2} = 0 \quad (8)$$

$$C_1 \frac{d^4 \phi}{dx^4} - \left(C - P \frac{I_o}{A} \right) \frac{d^2 \phi}{dx^2} - M_1 \frac{d^2 u}{dz^2} + M_2 \frac{d^2 v}{dz^2} = 0 \quad (9)$$

Here, u is the deflection of the beam in the z-direction, v is the deflection of the beam in the y-direction, and ϕ is the twist of the beam. P is the axial load in the beam, M_1 is the lateral bending moment and linearly dependent on P , M_2 is the vertical bending moment, and A is the area of the ellipse (Figure 4b). I_y , I_z , and I_o are the second moments of area about the major and minor axis and the polar moment of inertia of the ellipse, respectively. C_1 is the warping constant of the beam, which can be taken to be zero for an elliptical beam, and C is the torsional constant. The equations for these variables in the context of a thick walled hollow elliptical cylinder are

$$A = \pi(ab - (a - t)(b - t)) \quad (10)$$

$$I_y = \frac{\pi}{4}(ab^3 - (a - t)(b - t)^3) \quad (11)$$

$$I_z = \frac{\pi}{4}(a^3b - (a - t)^3(b - t)) \quad (12)$$

$$I_o = \frac{\pi}{4}[ab(a^2 + b^2) - (a - t)(b - t)((a - t)^2 + (b - t)^2)] \quad (13)$$

$$C = \pi G \left[\frac{a^3b^3}{a^2 + b^2} - \frac{(a - t)^3(b - t)^3}{(a - t)^2 + (b - t)^2} \right] \quad (14)$$

In these equations, a and b are the principal axes of the ellipse, as defined in previous sections. Based on these equations, the area of the beam is $A = 1.78 \times 10^{-13}m^2$, the moment of inertia about the vertical axis is $I_y = 1.19 \times 10^{-27}m^4$, the moment of inertia about the horizontal axis is $I_z = 2.47 \times 10^{-26}m^4$, and the polar moment of inertia is $I_o = 3.57 \times 10^{-26}m^4$. The torsion constant was calculated to be $C = 1.73 \times 10^{-16}Nm^2$. The horizontal moment of inertia of the beam (I_z) is roughly one order of magnitude greater than the vertical moment of inertia (I_y), which suggests that buckling will likely only occur in the horizontal direction. This simplifies the deflection equations from three sets of coupled ODEs to two equations of the form

$$EI_y \frac{d^4 u}{dx^4} + P \frac{d^2 u}{dx^2} - M_1 \frac{d^2 \phi}{dz^2} = 0 \quad (15)$$

$$\left(C - P \frac{I_o}{A} \right) \frac{d^2 \phi}{dx^2} - M_1 \frac{d^2 u}{dz^2} = 0 \quad (16)$$

The fixed-pinned boundary condition of the beam for deflection in the z-direction leads to the following forms for the deflection and twisting equations of the beam:

$$u(x) = A_1(\sin(\kappa x) - \kappa x \cos(\kappa)) \quad (17)$$

$$\phi(x) = A_2(\sin(\kappa x) - \kappa x \cos(\kappa)) \quad (18)$$

Here, $\kappa L = 4.493$, which is the first solution to the inequality $\kappa L = \tan(\kappa L)$ (79). Inserting these equations into Equations 15 and 16 results in a matrix with the coefficients A_1 and A_2 :

$$\begin{bmatrix} EI_y \kappa^2 - P & M_1 \\ M_1 & C - \frac{I_o}{A} P \end{bmatrix} \begin{bmatrix} A_1 \\ A_2 \end{bmatrix} = \mathbf{BA} = 0 \quad (19)$$

To obtain a nontrivial solution, the determinant of the \mathbf{B} matrix must be zero.

$$\text{Det}(\mathbf{B}) = (EI_y \kappa^2 - P) \left(C - \frac{I_o}{A} P \right) - M_1^2 = 0 \quad (20)$$

The only unknown variable in this equation is the load P , which means that it is a quadratic that is solvable both analytically and numerically. In the case of $M_1 = 0$, the classical Euler buckling and torsional buckling solutions for a beam are obtained (80). In the presence of an additional bending moment, buckling will occur at a lower load.

A larger lateral offset of the beams from the central node of the structure generates a higher bending moment, which effectively lowers the force necessary to initiate buckling. In the ideal case where $M_1 = 0$, it was calculated that the minimum load required to buckle an individual strut is $P_{cr} = 55.5 \mu N$. When this calculation is performed using a moment $M_1 =$

$1.13 \times 10^{-7} N m$, which corresponds to the approximate moment induced during the compression of the large-offset structure, the critical load drops down to $P_{cr} = 55.0 \mu N$. Using Equation 57, these loads are multiplied by $2\sqrt{2}$ to calculate the effective resolved load in the 4-bar setup of the compression of a unit cell. The resulting applied force F that is needed to buckle the struts in the full unit cell structure is $0.157 mN$ for a structure with no central moment, meaning no offset, and $0.155 mN$ for the beam with a central moment of M_1 .

2.4.4. Comparison between Experimental, Simulation, and Modeling Results

There is a strong agreement between the experimental results and the FEM simulations, both qualitatively in the observed deflection (Figure 3a-c and Figure 5a-c) and quantitatively in the load-displacement data (Figure 5e). The close agreement between the experimental results and the FEM result indicates that the elastic model was able to sufficiently replicate the behavior seen experimentally. This correlates well with the fact that the TiN in the experiment was nanocrystalline, meaning that there are few mechanisms for plasticity (81).

The maximum load obtained in the FEM simulations of the small-offset and the large-offset structures closely matched the load obtained in the analytical buckling analysis. The initiation of buckling in the FEM model occurred at a lower load than the theoretical buckling load for both structures (Figure 5e), with the large-offset structure displaying a greater deviation from the theoretical buckling load than the small-offset one. This implies that the effect of the offset can be explained in the context of a structural imperfection. In a perfect beam, when the structure reaches the critical buckling load, there is a sudden jump to the buckled state that corresponds to a bifurcation in the load. Any imperfection in the beam, such as a bend, surface roughness, or waviness, facilitates a more gradual transition to the buckled state because the beam has been locally pre-bent, with larger imperfections leading to greater deviations from

perfect buckling. This behavior is described in detail in (82), where the degree of deviation from the perfect beam buckling response is directly related to a parameter $k = a/r$. Here, a is the lateral offset of the bent beam from the perfect structure and r is the radius of gyration, defined as $r = \sqrt{I/A}$, where I is the second moment of area in the buckling direction and A is the cross-sectional area of the beam. The analytic buckling model does not account for any imperfections, which means it is predicting the critical load necessary to initiate buckling in a perfect beam and is not able to account for any imperfections.

The close agreement between the deflection behavior observed experimentally, the FEM modeling, and the analytic beam buckling approach strongly suggests that the observed deflection of the structure was due to a buckling instability. Equations 15 and 16 show that lateral and torsional buckling are coupled due to the additional central moment in the structure. Therefore, any lateral buckling of the beam will couple with torsional buckling resulting in lateral-torsional buckling (83, 84), as was observed in both the experimental results and the FEM model. The values for these three results are plotted in Figure 5e.

2.5. Cyclic Compression of a Single Unit Cell

Figure 6a-c shows SEM images of the deformed octahedron unit cell subjected to cyclic compression, and Figure 6d-f shows the corresponding load–displacement data (Movie 2-Movie 4). Three consecutive sets of 11 load-unload cycles were performed on a single unit cell. The data shown was corrected to account for the vertical deflection of the lower nodes of the structure in the same manner as for the monotonic compressions.

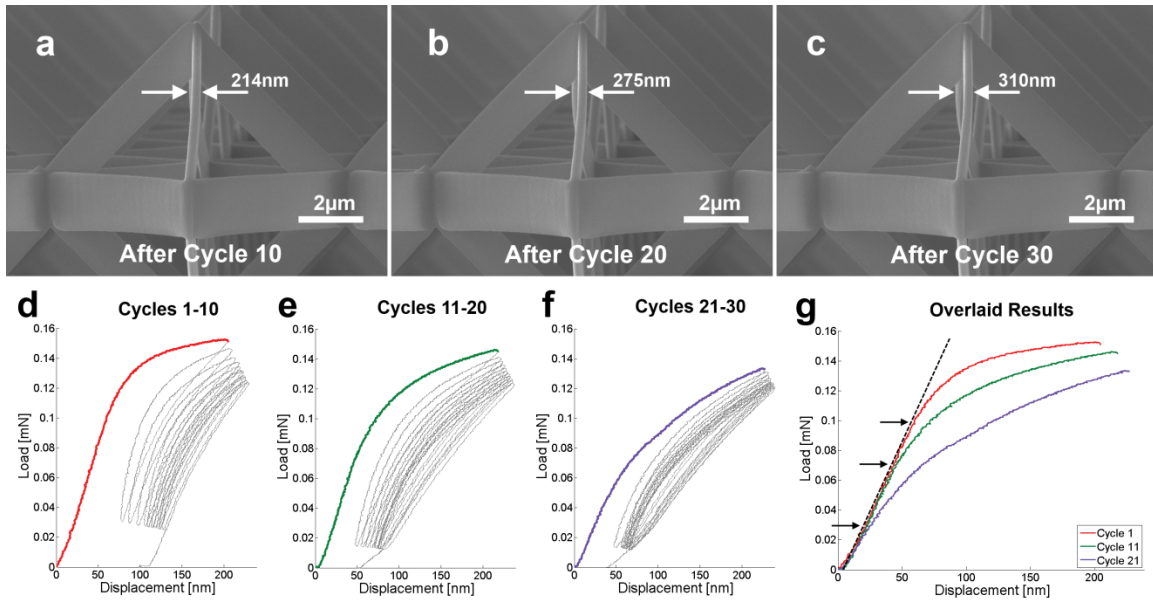


Figure 6: Cyclic compression of unit cell.

a–c) Images showing progressive bowing of beams during cyclic compressive loading. The bowing gives rise to a weakened load displacement response, as shown in the graph in g. Each image corresponds to an additional ten cycles of unloading–reloading. d–f) Three rounds of cyclic loading experiments that were performed on a single unit cell of the structure. g) The weakened load displacement response of the first compression in each of the cyclic loading experiments. This graph is shown to demonstrate the progressively earlier onset of nonlinearity, a response which closely matches that of a pre-bent beam buckling.

The unit cell survived cyclic compression loading of up to 95% of the maximum load prescribed in the uniaxial test without failure. The loading data in each cycle are characterized by elastic loading followed by a nonlinear response, whose onset occurred at progressively lower applied forces: from 114 to 84 μN after 11 cycles, and to 41 μN after 22 cycles (Figure 6g). The extent of the nonlinear response increased from 125 nm after the first set of cycles to 160 nm after the last. The large strain recovery seen during cyclic loading (Figure 6d–e) implies that the deformation was primarily elastic. Although there is some permanent deformation observed, it is minimal and only observed after many compression cycles at loads close to the failure limit.

The observed hyperelasticity in the loading and unloading cycles is likely the result of a bifurcation caused by torsional buckling within the tubes (83, 84), and the load-displacement response corresponds well with the fully elastic FEM that were performed on a single unit cell. The progressively lower loads for the initiation of non-linear behavior during cycling can then be

explained in the context of buckling, because buckling will initiate at a lower load for a beam that is pre-bent. The hysteresis observed in the cyclic load displacement data may be explained by accounting for the friction between the top surface of the structure and the indenter tip. The steep inclination of the beams means that friction will play a lesser effect on the onset of buckling because it does not act as directly in the direction of the buckling. The unbuckling response will still have a hysteresis, as demonstrated experimentally in (85, 86).

2.6. Monotonic Compression of a Full Nanolattice

2.6.1. Experimental Results

Figure 7 shows video stills from the compression of a full nanolattice structure along with the corresponding experimental stress-strain data. The stress-strain data shows that the sample initially deformed in a linear-elastic manner followed by a brittle catastrophic collapse at the peak stress. The large strain burst indicates that the nanoindenter controller was unable to maintain the prescribed loading displacement rate; this is likely due to the inertia of the system. There is a sparse set of data that was collected after the yield point (Figure 7c), but the exact values of the data may be an artifact of the system. The post-deformed image of the structure (Figure 7b) shows the six topmost unit cells were fully compressed to failure. A full collapse of the structure was prevented due to a limitation in the travel distance of the indenter. The stress and strain at failure were estimated to be $\sigma_y = 0.873 \text{ MPa}$ and $\varepsilon_y = 0.0218$ using a measured top surface area $A = 8588 \mu\text{m}^2$ and a height $h = 88.0 \mu\text{m}$. The elastic modulus, calculated to be $E = 61.8 \text{ MPa}$, was found using the loading slope of the stress-strain data.

The failure mode of the 4-bar unit cell structure was elastic buckling followed by fracture near the midpoints of the beams, but this failure mode cannot be generalized to the entire

structure, which experiences a more complex stress state. Additional failure modes might be activated as a result of bending and twisting actions of the beams. The experiments performed on the individual unit cells allow us to gain some insight into the possible failure mechanisms, and additional studies on the entire structure are necessary to fully understand the range of possible failure modes.

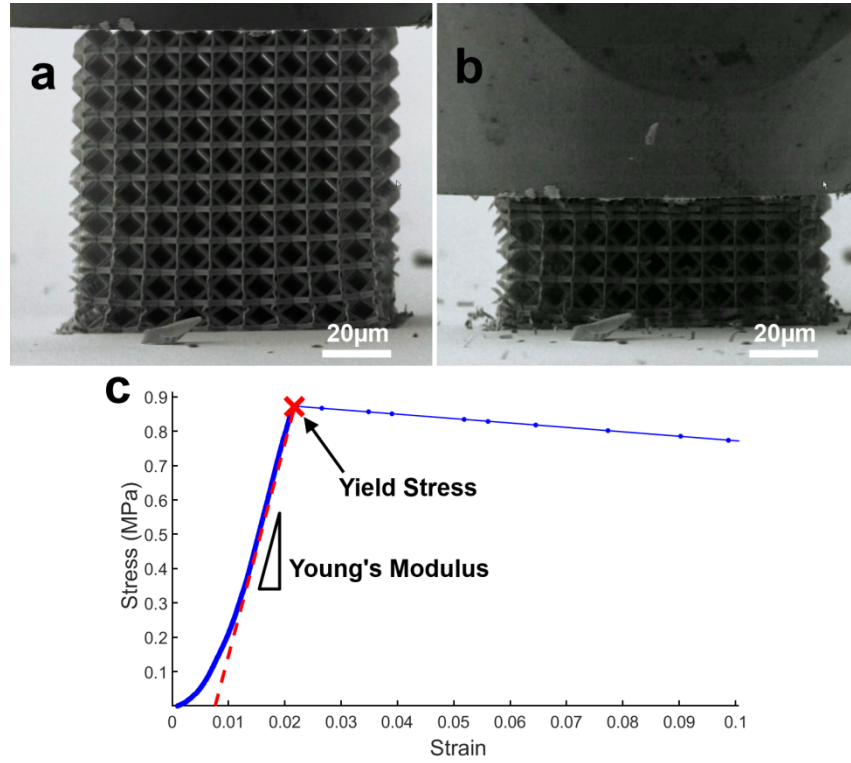


Figure 7: Monotonic compression of a full nanolattice.

a) Full structure at the beginning of a compression test. b) Structure after the yield point indicated in the graph. c) Stress-strain data from the compression of the above structure.

2.6.2. Cellular Solid Model

The octahedron geometry of the nanolattice fabricated in this study is a bending-dominated structure, and it can be compared to the classical model for open-cell foams. It is therefore possible to approximate the strength and modulus of the nanolattice using classical Gibson-Ashby cellular mechanics relations derived for open-cell foams (2). For a brittle, open-cell foam, the modulus and strength scale with the relative density of the structure, defined as

$$\bar{\rho} = \rho/\rho_s, \text{ as}$$

$$E \approx E_s \bar{\rho}^2 \quad (21)$$

$$\sigma_{cr} \approx 0.2 \sigma_{fs} \bar{\rho}^{3/2} \quad (22)$$

Here, E_s is the Young's modulus of the constituent material. σ_{fs} is the modulus of rupture of the constituent material, which is defined as the maximum tensile stress achievable before failure. The relative density scaling relations for the strength and modulus arise because of the bending dominated nature of the structure, and the coefficient of 0.2 for the strength relation is due to the fact that the nanolattice is composed of a brittle material. The relative density of the structure in this work was computed to be $\bar{\rho} = 0.0136$, which was found using a computer aided design (CAD) of the structure, and is similar to the relative density of other ultra-light materials like aerogels (87).

Using this model with a constituent material modulus of $E_s = 98 \text{ GPa}$ and a modulus of rupture of $\sigma_{fs} = 1.75 \text{ GPa}$ as obtained from finite element experiments, the structural stiffness and strength were calculated to be $E = 18.39 \text{ MPa}$ and $\sigma_{cr} = 0.559 \text{ MPa}$.

2.6.3. Comparison between Experimental and Modeling Results

The strength and modulus of the nanolattice are underestimated by the classical Gibson and Ashby scaling laws by a factor of 1.56 and 3.35 times, respectively. The classical cellular solids models given by Gibson and Ashby (2) have been analytically derived for an isotropic, open cell material with solid walls, where a bending of the beams gives rise to high stress concentrations near the nodes of the structure. The nanolattice material, which is a bending dominated structure with hollow thick walled beams, has similar conditions to those used in the analytic derivation, and it is therefore reasonable that they would follow a similar, although not identical, scaling law. The biggest difference comes from the large anisotropy of the elliptical

tubes, which have an aspect ratio of 4.5:1. This high aspect ratio gives the tubes a moment of inertia in the vertical direction that is roughly one order of magnitude higher than that in the horizontal direction. Because the analytic model for a bending dominated structure assumes isotropic beam bending, it is insufficient to perfectly analyze the structure, although it still can be used to obtain a reasonable approximation.

The difference between the experimental and analytic results for the strength and modulus can be explained using anisotropy results that have been derived previously for anisotropic structures with elongated unit cells. It is shown in (2) that the degree of anisotropy in the modulus and strength can be quantified using an anisotropy ratio R , defined as the ratio between vertical and transverse dimensions of a unit cell. In these equations, the anisotropy in the modulus scales approximately with R^2 , and the strength anisotropy scales approximately with R , meaning that the modulus is much more sensitive to the anisotropy than the strength. While the scaling equations used in (2) do not directly apply to anisotropic beam members, they do suggest that the discrepancy observed between the experimental and analytic results follows the correct trend. A more in-depth derivation is needed to properly account for the anisotropy of the beams in an analytical model.

2.7. Understanding Material Properties – Titanium Nitride

2.7.1. Experimental Results and Characterization

Bulk titanium nitride is typically a brittle ceramic, whose failure is governed by microstructural flaws (88). The tensile yield strength of 1.75 *GPa* obtained from FEM modeling in this work appears to be 1-2 orders of magnitude higher than values reported for typical bulk ceramics, which generally range from tens to hundreds of MPa (89). The high tensile yield

strength in the ALD-deposited TiN is attributed to the competition between internal (microstructural) heterogeneities like grain boundaries and constituent material defects. Recent work by Gu, et al reported that failure in nanocrystalline platinum nanostructures was not governed by the presence of external notches but was driven by microstructural heterogeneities (71). This transition coincides with a yield strength that is governed by grain boundary failure and represents a significant fraction of the theoretical material fracture strength, approximated to be between $E/2\pi$ and $E/30$ (65, 90).

The Young's modulus of 98 GPa found in the experiments is on the lower end of the range of the reported values for bulk TiN (67, 89). The most likely causes of the reduced Young's modulus are the porosity of ALD-deposited material and the grain size of $10 - 20 \text{ nm}$ in the TiN films, the most critical of which being the porosity of the sample. The modulus of a material is highly dependent on density, and lower relative density materials can have considerably reduced Young's moduli (91). The modulus has been shown to decrease linearly with relative density for a number of materials. For example, in work by Andrievski (67), it was shown that the modulus of TiN had a strong linear scaling with relative density, with a porosity of 20% corresponding to an 80% reduction in the modulus. It has been shown that atomic layer deposition (ALD) onto polymers may result in lower film densities because the gas-phase reactants can diffuse into the polymer (92). While the porosity of the constituent TiN was not thoroughly investigated, it is likely a major contributor to the observed reduction in modulus. The other important factor in the modulus reduction is the nanocrystalline microstructure of the TiN in this work, with the grains on the order of $10 - 20 \text{ nm}$ (Figure 1j). For materials with nanocrystalline grains, a larger volume fraction of the material is comprised of grain boundaries, which have been shown to be less dense than a regular crystal lattice, and therefore have a lower

Young's modulus (91). When the grain size of iron, copper, and palladium samples was reduced to 10 – 20 nm in (91), a decrease of up to 26% in the Young's modulus was reported and explained through the increased volume fraction of grain boundaries. This combination of high porosity and nanometer-sized grains may explain the reduction in the modulus from a maximum of ~490 GPa reported in literature for fully dense bulk TiN (67) to the 98 GPa found in this study.

2.7.2. Theoretical Material Model

Failure in ceramics generally initiates at an imperfection with the highest stress concentration, such as a crack or a void. Fracture strength of typical ceramics is a few orders of magnitude lower than those predicted theoretically for a perfect material (90). The observed high tensile strength of 1.75 GPa and the bending strain of 1.8% that were attained by the TiN struts in this work are unusually high for a nanocrystalline ceramic. This high strength might be understood by considering the competing effects of microstructural and external local stress fields on strength and failure initiation (71). In macroscopic brittle materials, the fracture strength, σ_f , is defined by the crack geometry and size,

$$\sigma_f = \frac{K_c}{\sqrt{\pi a}} \quad (23)$$

where K_c is the fracture toughness and a is the initial flaw size (90). Equation 23 shows that the strength of materials is inversely proportional to the square root of the size of pre-existing flaws, which serve as weak spots for failure initiation and reduce material strength. In large samples, the wide statistical distribution of flaw sizes leads to a relatively high probability of finding a weak spot, and the material will break at a relatively low applied stress. In smaller samples, the distribution of flaw sizes is narrower, which lowers the probability of finding a

large flaw and shifts the strength of the weakest link up. In sufficiently small nanocrystalline samples, the low probability of finding a weak external flaw and the blunting of the notch tip by nucleated dislocations render the stress concentration at the external flaws comparable to those within the microstructure, that is, grain boundary triple junctions (71). In these small samples, usually with nanometer dimensions, failure has been shown to initiate at the location with the highest stress concentration, internally or externally (71). Fracture strength of materials whose failure is described by the weakest link theory is commonly explained by Weibull statistics (90). The probability of finding the weakest spot inversely scales with the sample volume, V . Weibull analysis predicts the fracture strength to be proportional to $1/V^{1/m}$. Here, m is the Weibull modulus, a measure of statistical variability where higher m corresponds to a wider statistical distribution of strength (90). The volume of hollow TiN nanolattices can be approximated to be $V \sim At$, where A is the total surface area and t is the wall thickness. When the wall thickness of hollow TiN tubes is the only varying geometric dimension, the fracture strength of TiN walls becomes

$$\sigma_f \propto \left(\frac{1}{t}\right)^{\frac{1}{m}} \quad (24)$$

Equation 24 implies that nanolattices with thinner walls are expected to be stronger up to a critical length scale, t , because the attainable stress in any material is bounded by a theoretical upper limit, often called the ideal fracture strength. A reasonable approximation of this strength may be between $E/2\pi$ and $E/30$ (65, 90, 93), which represents the atomic bond strength of a material along the tensile loading direction, and is independent of sample size (90). Figure 8 depicts an illustrative plot of strength as a function of sample thickness, which shows the intersection of the theoretical strength and that described by Equation 24 at the critical thickness

of t . This plot illustrates the saturation of the fracture strength at the theoretical upper limit in samples with dimensions lower than t .

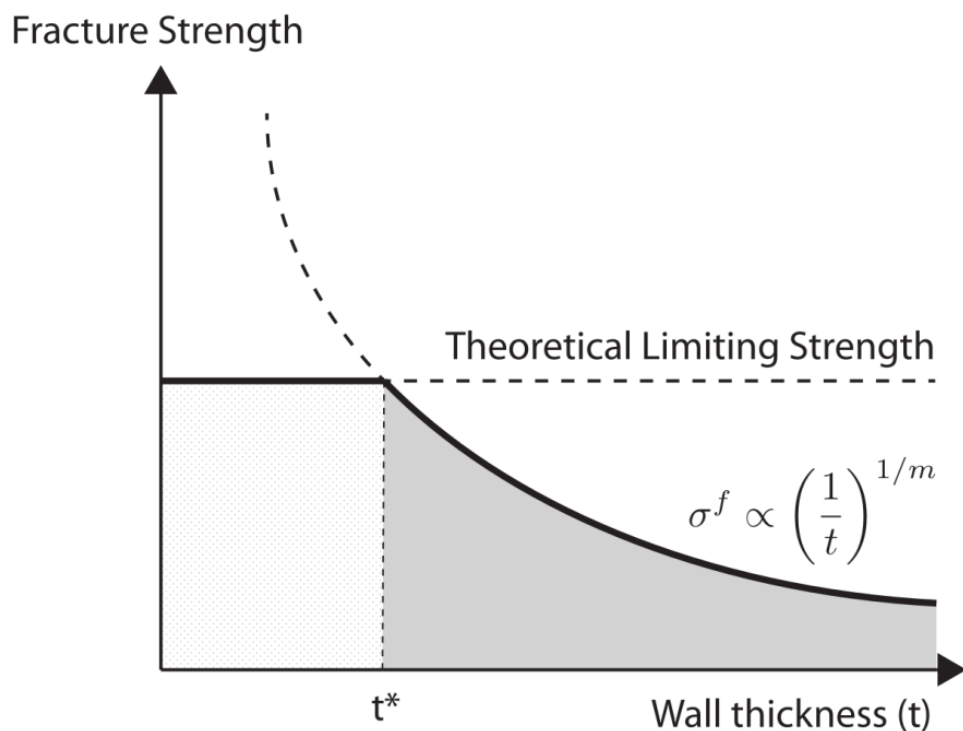


Figure 8: Schematic representation of theoretical strength.

Theoretical strength is independent of sample size, and fracture strength described by Weibull statistics.

FEM simulations on samples with the same material properties and of the same geometry as in the experiments predict the maximum tensile stresses in the TiN struts to be 1.75 GPa , close to the theoretical elastic limit of 3.27 GPa (estimated by $E/30$ with $E = 98 \text{ GPa}$), which suggests that the wall thickness of 75 nm in the hollow TiN nanolattices might be close to the critical length scale. This line of reasoning serves as a phenomenological first-order type of model, which may help explain the attainment of unusually high tensile strengths in the thin TiN walls without failure. Rigorous theoretical studies on uncovering the deformation mechanisms in nanosized solids, which may or may not contain internal stress landscapes, are necessary to capture the complex physical phenomena associated with their deformation and failure.

Chapter 3: Strong, Lightweight, and Recoverable 3D Ceramic Nanolattices

3.1. Chapter Summary

This work investigates the creation of an ultralight hollow-tube nanolattice with an octet-truss geometry that consists solely of a brittle ceramic, aluminum oxide (alumina/ Al_2O_3), and exhibits nearly full recoverability after compressions in excess of 50% strain. The samples shown in this work are able to absorb energy, recover after significant compression, and reach an untapped strength and stiffness material property space. This is achieved using high-strength ALD alumina engineered into a thin-walled nanolattice that is capable of deforming elastically via shell buckling. Nanomechanical experiments reveal that the Young's modulus of the nanolattices scales with relative density as $E \sim \bar{\rho}^{1.61}$, and failure strength scales as $\sigma_{ys} \sim \bar{\rho}^{1.73}$, which differ from the analytical scaling for both stretching- and bending-dominated structures because of the hollow tubes and nodes. The ultralight ceramic nanolattices represent the concept of materials by design, where it is possible to transform a strong and dense brittle ceramic into a strong, ultralight, energy-absorbing, and recoverable metamaterial. These results serve to emphasize the critical connection between material microstructure, hierarchical architecture, and mechanical properties at relevant length scales.

3.2. Al_2O_3 Nanolattice Structure and Fabrication

Nanolattices in this work were designed in an octet-truss geometry (Figure 9), which is a fully rigid topology with an average beam connectivity of $Z = 12$. The tubes were designed to be hollow with wall thicknesses t of between 5 – 60 nm, tube major axis a of between 0.45 – 1.38 μm , and unit cell widths L of between 5 – 15 μm (Figure 9B and C), spanning

length scales that can be controlled across four orders of magnitude. The relative densities of samples in this work spanned $\rho = 0.21\% - 8.6\%$. Using a reported value for the density of ALD alumina, $\rho_s = 2900 \text{ kg m}^{-3}$ (94), the absolute densities of nanolattices were calculated to be $\rho = 6.1 - 249 \text{ kg m}^{-3}$, which places the lightest ones into the ultralight regime, defined as materials with densities $\leq 10 \text{ kg m}^{-3}$ (11). This density range is comparable to that of aerogels (87) and other ultralight materials (11, 12). Transmission electron microscopy (TEM) analysis revealed ALD alumina to contain 2 – 10 nm nanocrystalline precipitates intermixed in an amorphous matrix (Figure 9F). A list of the parameters and relative densities of samples tested in this work is provided in Table 3.

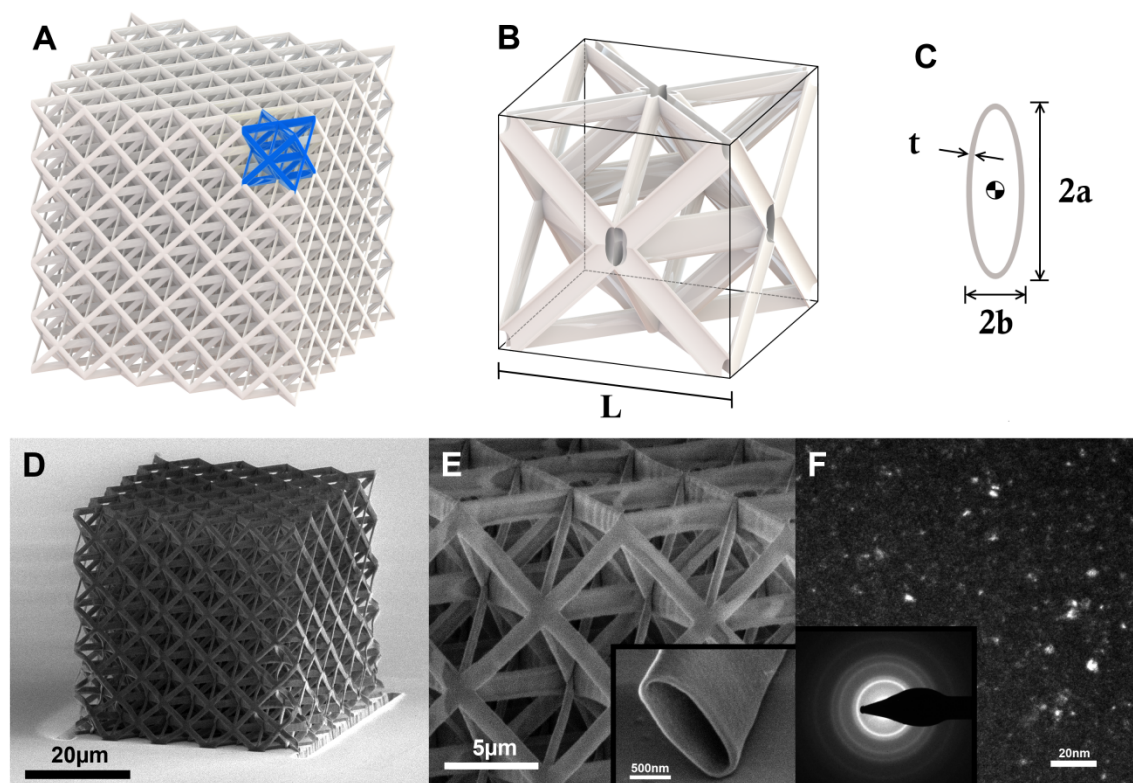


Figure 9: Design and microstructure of octet-truss alumina nanolattices.

A) CAD image of the octet-truss design used in the study. The blue section represents a single unit cell. B) Cutaway of hollow octet-truss unit cell. C) Hollow elliptical cross section of a nanolattice tube. D) SEM image of alumina octet-truss nanolattice. E) Zoomed-in section of the alumina octet-truss nanolattice. The inset shows an isolated hollow tube. F) TEM dark-field image with diffraction grating of the alumina nanolattice tube wall.

Octet-truss polymer nanolattice scaffolds are written using a two photon lithography direct laser writing process in IP-Dip photoresist using the Photonic Professional lithography system (Nanoscribe GmbH). Structures are written using laser powers in a range from 6 – 14 *mW* and a writing speed of $\sim 50 \mu\text{m s}^{-1}$. The laser power is used to control the diameter of the tubes, and the speed varies slightly during the writing process to control the quality of the structure. After a polymer scaffold is created, the structures are conformally coated in alumina using atomic layer deposition (ALD). ALD allows for the deposition of conformal coatings on complex 3D geometries with angstrom-level thickness control, resulting in high quality finished structures (63, 95). Deposition is done at 150°C in a Cambridge Nanotech S200 ALD system using the following steps: H₂O is pulsed for 15 *ms*, the system is purged for 20 *s*, trimethyl aluminum (TMA) is pulsed for 15 *ms*, the system is purged for 20 *s*, and the process is repeated. The carrier gas is nitrogen, which is used at a flow rate of 20 *sccm* (standard cubic centimeters per minute). The process was cycled for between 50 and 600 cycles to obtain the desired thickness coatings on the nanolattices. The thickness of the coatings was verified using spectroscopic ellipsometry with an alpha-SE Ellipsometer (J.A. Wollam Co., Inc.). After deposition, two outer edges of the coated nanolattice are removed using focused ion beam (FIB) milling in an FEI Nova 200 Nanolab system in order to expose the polymer to air. Once the polymer is exposed, the samples are placed into an O₂ plasma barrel asher for between 50 – 75 *hours*, depending on the overall size of the sample, with a 300 *sccm* flow rate of O₂ under 100 *W* of power in order to fully remove the polymer. Structures that had been etched were cut open using FIB milling to ascertain whether the polymer had been fully removed (Figure 10B and C). It is also possible to discern the amount of polymer that has been etched away by looking at the change in contrast of the nanolattices (Figure 10A).

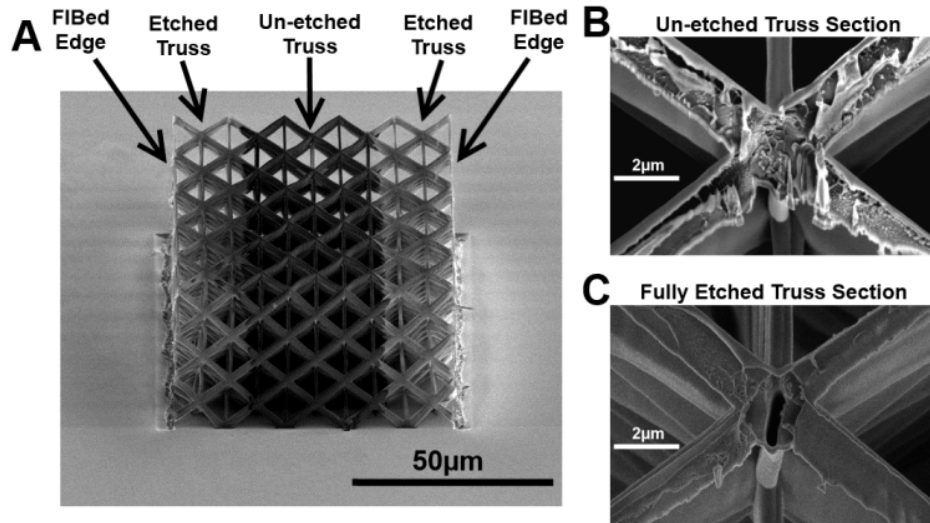


Figure 10: Illustration of the nanolattice etching process.
A) Half-etched nanolattice showing the contrast change of the etched vs unetched portions. (B) Cross section from the partially etched section of the structure. C) Cross section of the fully etched section of the structure.

3.3. Nanolattice Compression Experiments

3.3.1. Experimental Setup and Data Analysis

Monotonic and cyclical uniaxial compression experiments were performed on nanolattices in a G200 XP Nanoindenter (Agilent Technologies). In the first set of experiments, structures were compressed uniaxially to $\sim 50\%$ strain at a rate of 10^{-3} s^{-1} to determine their yield stress and overall deformation characteristics (Figure 11A, Figure 12 and Figure 14A-D). In the second set of experiments, structures were cyclically loaded and unloaded three times to $\sim 70\%$ of their failure load, and unloading slopes from each cycle were averaged to estimate Young's modulus (Figure 11B). Unloading rather than loading moduli were used to mitigate the possible effects of loading imperfections such as misalignment and partial initial contact. Effective stress and strain data was calculated by normalizing the load and displacement data by the footprint area and sample height respectively. The Young's modulus and yield strength data reported are the effective structural properties of the nanolattices.

Additional samples were compressed in an in-situ nanomechanical instrument, InSEM (Nanomechanics Inc.), to observe local and global deformation characteristics and to investigate the failure modes that occurred during deformation (Movie 5 to Movie 7). Stress-strain data and still frames of the in-situ compression experiments are shown in Figure 12.

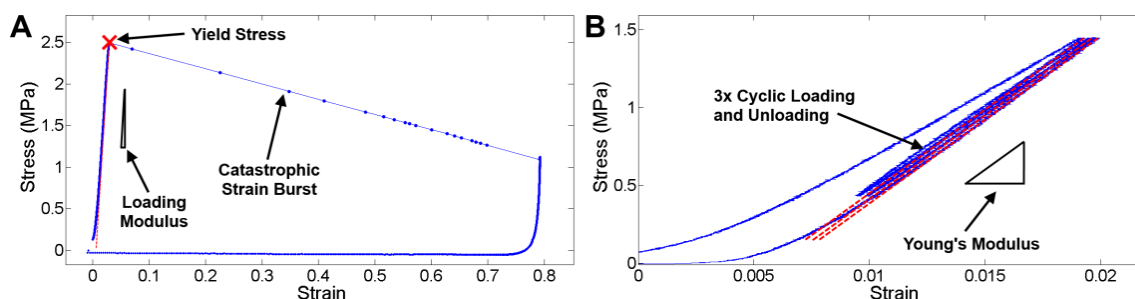


Figure 11: Representative stress-strain curves of nanolattice compression experiments.

A) Example of one of the compression experiments on a thick-walled nanolattice showing the loading slope, the yield strength, and the deformation characteristic. B) Example of a cyclic loading test on a nanolattice showing the unloading modulus fit used to measure the Young's modulus.

3.4.2. “Thick-walled” Structure Compression

Two distinct deformation signatures were observed during nanolattice compressions. These are best characterized using the thickness-to-radius ratio of the tubes, t/a , as a figure of merit. Structures with $t/a \geq 0.03$, referred to here as thick-walled, demonstrate linear elastic loading followed by catastrophic brittle failure (Figure 14A, B, E, and F). An example of a typical deformation and corresponding stress-strain data are shown in Figure 12F-J and in Movie 7. Compressive stress-strain data for thick-walled structures show large strain bursts, with burst magnitude increasing at greater t/a ; structures with $t/a = 0.032$ have bursts of $\sim 10\%$ strain (Figure 14B), whereas structures with $t/a = 0.067$ show bursts of $\sim 80\%$ strain (Figure 14A). This observed increase in burst magnitude is probably driven by greater elastic strain energy stored in thicker-walled structures during deformation. Each strain burst corresponds to a discrete brittle failure event, which leads to permanent damage of the structure (Figure 12J and Figure 14E and F). This type of catastrophic failure has been observed in previous experiments

on hollow ceramic nanolattices (96) and ceramic composites (14) and is typical of ceramic foams (2).

3.4.3. “Thin-walled” Structure Compression

Thin-walled nanolattices, defined as those with $t/a \leq 0.02$, did not exhibit catastrophic failure or discrete strain bursts. Samples in this regime first deformed elastically, where stress increased linearly with strain, followed by a ductile-like, controlled deformation, with stress plateauing after yielding (Figure 14C and D). An example of a typical deformation and corresponding stress-strain data are shown in Figure 12A-E and in Movie 5. As the t/a of the samples decreased, the serrated burst behavior seen in the thick-walled structures was suppressed, and stress-strain data became smooth (Figure 14C and D). After yielding, all ensuing deformation was accommodated through wrinkling and local buckling of the tube walls (Figure 12D and E and Movie 5). All thin-walled ceramic nanolattices exhibited notable recovery after deformation, with some recovering up to ~98% of their original height after compression to 50% strain (Figure 12E and Figure 14H) and others recovering by ~80% after compression to 85% strain (Figure 15). Structures with smaller unit cells demonstrated greater recoverability, each recovering to at least 95% of its original height. Nanolattices with larger unit cells recovered less on average, but all recovered to at least 75% of their original height. SEM images of post-deformed structures revealed localized cracking on and around the nodes (Figure 14J), implying that the failure of ALD alumina remained brittle and that the observed deformability and recoverability probably emerged from structural effects.

Nanolattices with $0.02 \leq t/a \leq 0.03$ exhibited a combination of the two described deformation signatures. In these samples, both brittle and ductile-like deformation took place; several minor strain bursts were present, and marginal recovery occurred after compression to

50% strain (Figure 14C, G, and I and Movie 6). The in-situ deformation Movie 6 shows that each strain burst correlates with discrete local brittle fracture events in the tubes, and post-yield ductile-like behavior corresponds to buckling and wrinkling of the tube walls. The transition between these two deformation modes is probably driven by an energetic competition between elastic and brittle failure.

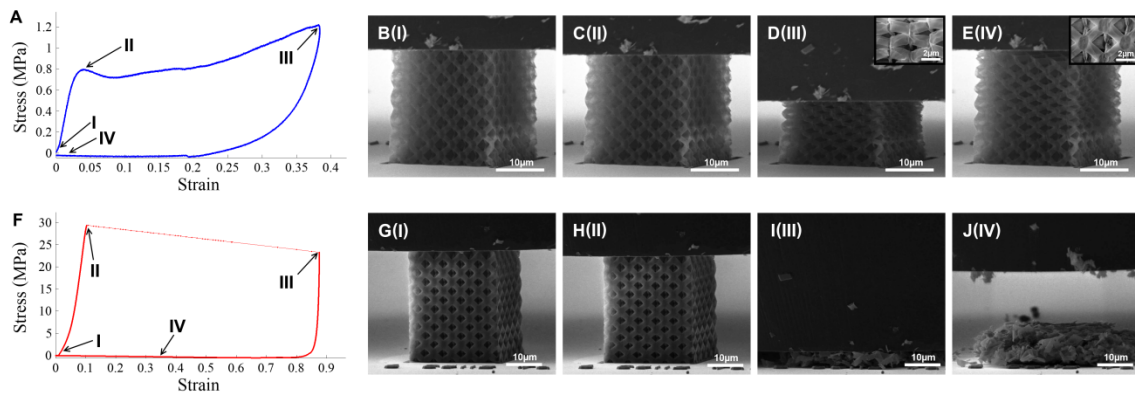


Figure 12: Compression experiments on thick- and thin-walled nanolattices.

A-E) Mechanical data and still frames from the compression test on a thin-walled ($L = 5$ mm, $a = 650$ nm, $t = 10$ nm) nanolattice demonstrating the slow, ductile-like deformation, local shell buckling, and recovery of the structure after compression. F-J) Mechanical data and still frames from the compression test on a thick-walled ($L = 5$ mm, $a = 790$ nm, $t = 50$ nm) nanolattice showing catastrophic brittle failure and no post-compression recovery.

3.4. Failure and Recoverability Model Formulation

Three competing failure mechanisms exist for hollow-tube lattice structures: fracture of the tube wall, Euler (beam) buckling of a truss member, and local (shell) buckling of the tube wall (97). A failure mechanism (or failure mode) is defined here to be any event that causes a loss of structural integrity of the nanolattice. Different combinations of these mechanisms can occur during deformation depending on the stress state that arises in the beams during loading. Elastic deformation will occur in a structure when the stress necessary to initiate buckling, which is an elastic process, is less than the critical stress required for fracture.

By equating the stresses necessary to initiate each failure mechanism, it is possible to obtain an expression for the critical transition point between fracture and elastic failure in a truss

structure. The following section details the derivation of these expressions. The three potential failure modes in a lattice structure – fracture, Euler (beam) buckling, or local (shell) buckling – can be defined respectively from (98) as

$$\sigma_{fracture} = \sigma_{fs} \quad (25)$$

$$\sigma_{buckle} = \frac{\pi^2 EI}{(kL)^2 A_{tube}} \quad (26)$$

$$\sigma_{shell} = \frac{E}{\sqrt{3(1-\nu^2)}} \left(\frac{t}{r} \right) \quad (27)$$

Here, E is the Young's modulus, σ_{fs} is the fracture strength, and ν is the Poisson's ratio of the constituent material. t is the wall thickness, r_c is the radius of curvature and L is the length of a beam. k is a constant based on the boundary condition, which, for the stretching dominated geometry used here, can be taken to be 1/2 for a pinned-pinned boundary. I and A_{tube} are the area moment of inertia and cross sectional area, respectively. Taking the beams to be elliptical with a major and minor axis of a and b , respectively, a first order approximation of these parameters is found to be

$$I = \frac{\pi}{4} (3a + b) b^2 t \quad (28)$$

$$A_{tube} = \pi(a + b)t \quad (29)$$

The radius of curvature r_c of an elliptical beam varies from $r_c = a^2/b$ to $r_c = b^2/a$, depending on the position along the ellipse. The initiation point for shell buckling will occur where $\sigma_{shell}/\sigma_{local}$ is at a maximum, meaning it will happen at the highest local stress concentration with the smallest local radius of curvature. The largest radius of curvature is at the minor axis of the ellipse, and the maximum stress, which arises from a combination of uniaxial compression and vertical bending, concentrates toward the major axes of the ellipse. To simplify

the analysis, the radius of curvature at the point of shell buckling will be approximated here to be $r_c = a$ given the distribution of stresses in the beams. The diagonal tubes of the nanolattice are elliptical with an aspect ratio of $\sim 3:1$ ($a = 3b$). From this, the buckling failure criteria of the beams can be derived in terms of the major axis a of the ellipses to be

$$\sigma_{buckle} = \pi^2 E \left(\frac{3a + b}{a + b} \right) \left(\frac{b}{L} \right)^2 = \frac{5}{18} \pi^2 E \left(\frac{a}{L} \right)^2 \quad (30)$$

$$\sigma_{shell} = \frac{E}{\sqrt{3(1 - \nu^2)}} \left(\frac{t}{a} \right) \quad (31)$$

For the nanolattice structures, there are two competing sets of failure modes: yielding vs shell buckling and yielding vs Euler buckling. These competing modes can act independently or in combination. Yielding of the tubes will occur in tension, and Euler and shell buckling will occur in compression. In an idealized pin-jointed stretching-dominated structure, the beams are assumed to only experience uniaxial tensile or compressive stresses, and it is the stretching of the horizontal members in tension that will govern the strength and stiffness of the lattice (99) (Figure 13A). When the tubes are made to be hollow, load transfer at the nodes is governed by shell wall bending, and the resulting bending and ovalisation of the beam near the node will govern the strength and stiffness. A simplified representation of the stress concentrations that arise due to the hollow nodes is shown in Figure 13B.

If the compressive stresses and tensile stressed generated in the sample are assumed to be roughly equal, which is reasonable for a beam in bending, a critical transition between the modes can be found by setting the failure equations equal to each other. From this, the critical transition values are determined to be

$$\left(\frac{t}{a} \right)_{crit} = \frac{\sigma_{fs}}{E} \sqrt{3(1 - \nu^2)} \quad (32)$$

$$\left(\frac{a}{L}\right)_{crit} = \frac{3}{\pi} \sqrt{\frac{2\sigma_{fs}}{5E}} \quad (33)$$

Both of these relations are functions only of the constituent properties of the materials. Using mechanical property data reported for 75 nm thick ALD alumina, $E = 164 \text{ GPa}$, $\sigma_{fs} = 1.57 - 2.56 \text{ GPa}$, $\nu = 0.24$ (68), and Equations 32 and 33, the critical thickness-to-radius ratio that induces a transition from yielding to shell buckling in the nanolattices was calculated to be between $(t/a)_{crit} \approx 0.0161 - 0.0262$, and the critical radius-to-length ratio that denotes transition from yielding to Euler buckling was between $(a/L)_{crit} \approx 0.0591 - 0.0755$. The property space of all nanolattices studied here, along with their t/a , a/L , and predicted failure modes are shown in Table 3. The experimentally observed deformation behavior of each sample is also noted in the table.

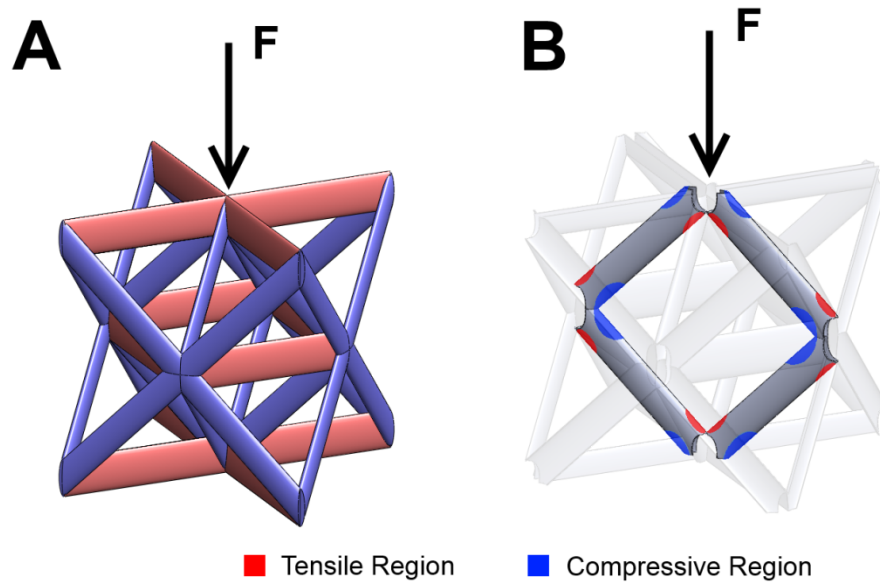


Figure 13: Simplified representation of stress state in nanolattices.

A) Idealized stress state in a solid tube, pin-jointed lattice structure. B) Schematic representation of a realistic stress state in a hollow tube lattice structure arising due to bending of the hollow beams near the nodes.

3.5. Comparison between Experimental Results and Failure Model

The thickness-to-diameter ratios of the nanolattices ranged from $t/a = 0.0059 - 0.0862$, which overlaps the range of $(t/a)_{crit}$ predicted by Equation 32. For thick-walled structures, whose $t/a \geq 0.030 > (t/a)_{crit}$, the model predicts that failure of the beams is dominated by brittle fracture within the alumina tubes. Fractured segments of tubes are unable to carry any load, so every failure event will cause a strain burst whose magnitude depends on the amount of strain energy stored in the system before failure. These predictions are corroborated by experimental stress-strain data for the thick-walled structures (Figure 12I and J, Figure 14E and F and Movie 7).

Failure in the thin-walled structures, whose $t/a \leq (t/a)_{crit} \leq 0.020$, is predicted to occur primarily via shell buckling, which is an elastic failure mode. This type of failure corresponds to a plateau in the stress-strain data caused by a gradual drop in load-carrying capacity of the beams (98), in contrast to the immediate drop in load-carrying capacity associated with fracture. Bending of an isolated thin-walled hollow beam often leads to shell buckling bifurcation, which can cause a jump in displacement (100). In a truss structure, the interactions and nodal support among all the beams delay the onset of bifurcation and allow the beams to gradually settle into a new mode. Shell buckling in thin-walled nanolattices is manifested as wrinkling and warping of the tubes near the nodes (Figure 12D and E, Figure 14H and J and Movie 5). The ductile-like deformation and recoverability observed in the experiments on the thin-walled nanolattices probably arise as a result of such shell buckling.

The proposed shell buckling model does not take into account the microstructural or material details, nor is it capable of predicting the deformation of structures in the transition regime of $0.020 \leq t/a \leq 0.030$. It is helpful in qualitatively explaining deformation in this

regime, where nanolattices experience a complex stress state with compressive, tensile, and shear components. Fracture occurs primarily under tension, and shear and buckling occur only in compression, which means that the stress state within the beams can simultaneously satisfy fracture and buckling conditions. This is observed experimentally as a mixing of fracture and buckling failure modes, along with suppressed strain burst behavior and some recoverability (Figure 14G and I and Movie 6).

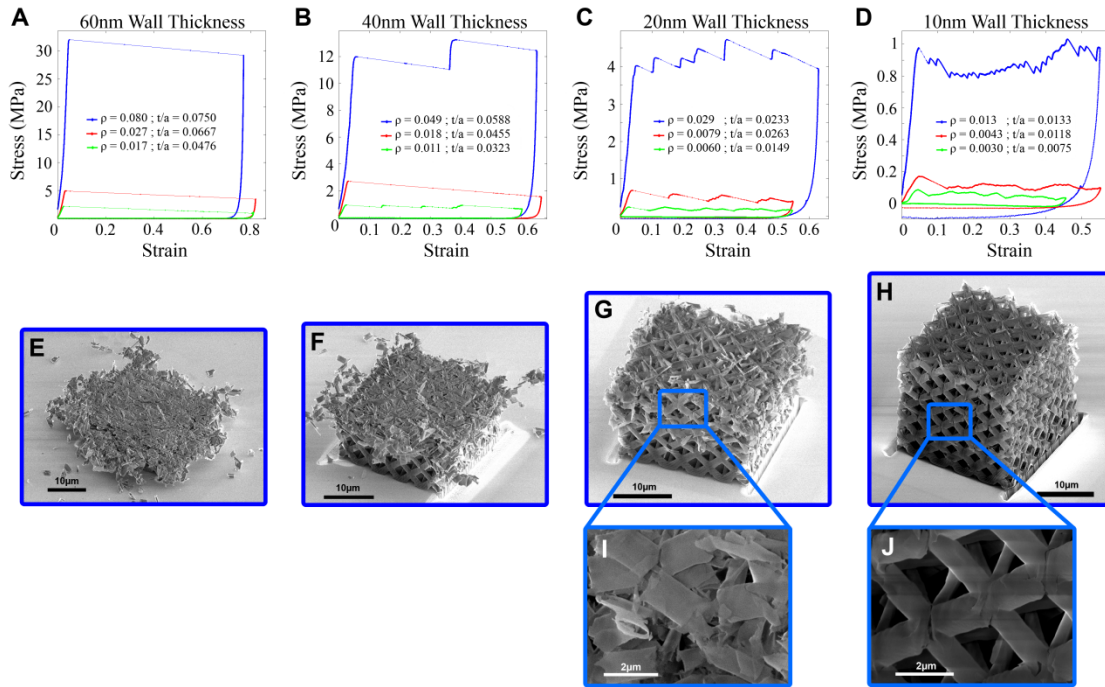


Figure 14: Mechanical tests on hollow octet-truss samples with varying t and $\bar{\rho}$.

A-D) Stress-strain plots of structures with varying wall thicknesses showing the transition from brittle to ductile-like deformation in thinner-walled structures. E-H) Post-compression images of the nanolattices showing the recoverability as wall thickness is reduced. I-J) Zoomed sections of post-compression nanolattices.

3.6. Discussion on Recoverability

Elastic recovery has been studied previously in metallic and polymer lattices, and models have been proposed for their recoverability (11, 101–103). None of these works account for the observed ductile-like behavior of the ceramic nanolattices, and elastically deformable structures composed of intrinsically brittle materials such as ceramics are virtually unexplored. It is postulated that reducing the t/a ratio to below $(t/a)_{crit}$ derived in Equation 32 enables failure

via shell buckling, an elastic failure mode that causes minimal damage to the beams and nodes and allows the structure to recover. The transition to elastic failure is a necessary condition to prevent initial yielding or fracture of the constituent material but not a sufficient condition to ensure recovery of the structure. Figure 12D shows that during shell buckling, the global deformation is accompanied by localized wrinkling and warping of the tube walls. This results in confined regions of high stress that can subsequently lead to localized fracture (Figure 12E and Figure 14J). The propagation of these localized microcracks depends on the overall stress landscape and flaw distribution. If a crack extends into a region of high tensile stresses, or if numerous flaws reside near a crack tip, it is likely to propagate through the node and can potentially result in fracture of the tube. If an existing crack extends into a region of compressive stress, or if the stress field is insufficient to continue the crack extension, its propagation will be suppressed so that the tubes may never fully fracture. In this mechanism, a sufficient number of nodal connections remain intact to enable the structure to recover nearly fully to its original shape. The applied compressive load reduces the local tensile stresses within the tube walls that are generated by bending of the beams, which generates a compressive stress state at the nodes that can impede the propagation of a crack. As the t/a is reduced, shell buckling will commence at a lower applied load, which lowers the probability of initiating and/or propagating an existing crack. The wall thicknesses of alumina are on the order of tens of nanometers, a length scale that has been shown to exhibit enhanced strengths and damage tolerance caused by a statistically lower probability of finding a weak defect (63). These are some of the phenomena that collectively give rise to recoverability of the alumina nanolattices (Figure 12E, Figure 14H and Figure 15).

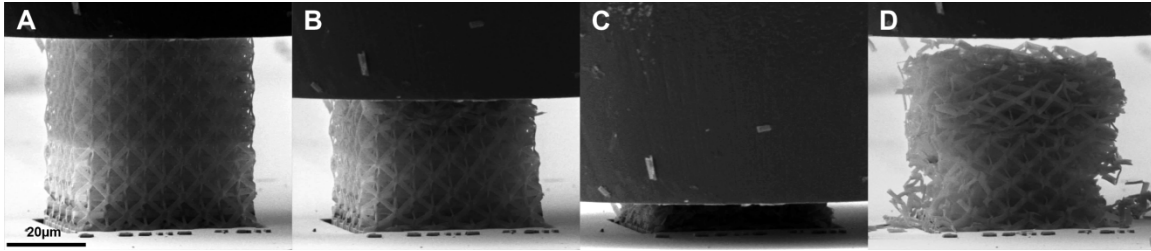


Figure 15: Compression of a thin-walled octet-truss nanolattice to high strain.

A) Pre-compression, B) 35% strain, C) 85% strain, and D) post-compression recovered nanolattice. Structural parameters are $L=10\mu\text{m}$, $a=750\text{nm}$, and $t=10\text{nm}$.

3.7. Strength and Stiffness Scaling with Density

The strength and Young's modulus of all the octet-truss nanolattices follow a power law scaling with relative density as $\sigma_y \sim \bar{\rho}^{1.73}$ and $E \sim \bar{\rho}^{1.61}$ (Figure 16A and B). This scaling outperforms traditional lightweight and ultralight bending-dominated structural materials, whose properties scale as $E \sim \rho^2$ or $E \sim \rho^3$ (11), but does not follow the analytic prediction for an ideal stretching-dominated structure, $\sigma_y \sim \rho$ and $E \sim \rho$ (78). Such a deviation from the analytic prediction can be explained, in part, by factors such as the ellipticity of the tubes, structural imperfections, and non-idealities of the experimental setup. This deviation is attributed primarily to the hollowness of the tubes, which affects the structural integrity of the nodes, where the highest stress concentrations will occur (101, 102). The strength and deformation of an ideal, monolithic, stretching-dominated cellular solid is governed by stretching of the beams, with the nodes acting as rigid pin-jointed elements that perfectly transfer load between truss members (78). In a hollow lattice, the nodes are constrained only by the shell walls, which has a detrimental effect on strength and stiffness because load transfer at the nodes occurs via shell wall bending. This, together with the sharp angles between the tubes, leads to an uneven distribution of stress and induces large stress concentrations in the vicinity of the nodes (Figure 9B and E). Bending of the tubes also causes large deflections and additional ovalization at the nodes, which further increases the compliance and stress concentrations. In-situ experiments and

post-compression analysis revealed that most of the deformation is localized to the nodes (Figure 12D and E and Figure 14J), which implies that improving nodal strength is a critical factor in enhancing the scaling of strength and stiffness with density.

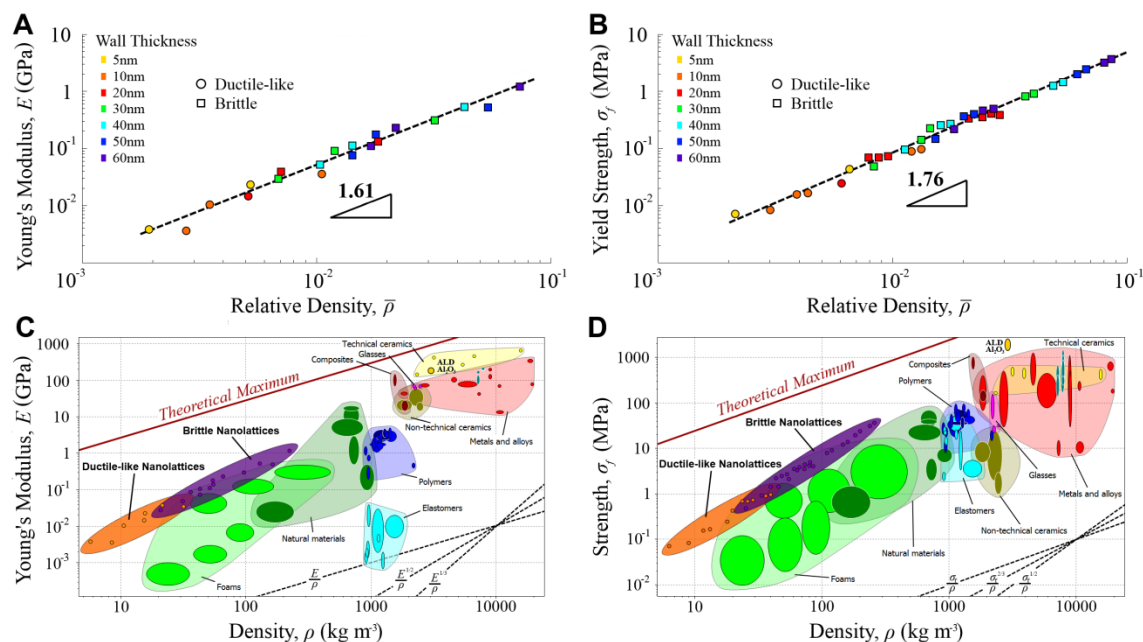


Figure 16: Strength and stiffness versus density of alumina nanolattices.

A-B) Stiffness and strength plotted against relative density for all tested samples. Data clearly obey a power law, with little deviation across wall thicknesses and failure modes. C-D) Material property plots (Materials Property CES Selector software by Granta Design) of the experimental stiffness and strength data against density for existing materials, showing that the materials created in this work reach a new niche in the high-strength and -stiffness lightweight material parameter space.

Chapter 4: Hierarchical 3D Nanoarchitected Materials

4.1. Chapter Summary

This work investigates the fabrication, mechanical characterization, and computational analysis of hierarchical nanolattices made out of three different materials: (1) solid polymer IP-Dip (Nanoscribe GmbH), (2) a core-shell composite with a polymer core and a 20 *nm* thick Al₂O₃ coating, and (3) hollow 20 *nm* thick Al₂O₃. The hierarchical architectures in this study demonstrated exceptional strength, stiffness, and damage tolerance over simple periodic ones. In-situ nanomechanical deformation experiments were performed on a number of different geometries and revealed a range of tunable deformation and recoverability mechanisms, along with a nearly linear scaling of yield strength and stiffness with relative density. It is further shown that the incorporation of multiple levels of self-similar hierarchy does little to improve the mechanical properties and in some cases degrades them. Simulations were performed to further elucidate the local stress distributions within the nanolattices, which confirm the effective experimental nanolattice response and help shed light on the distribution of load bearing components that are responsible for the overall observed nanolattice performance. This ability to engineer material structure on the most fundamental length scales opens up a new design space where material properties—mechanical, thermal, electrical, photonic, etc.—can be controlled and tuned independently by properly choosing atomic-level microstructure, critical material dimensions, and architecture.

4.2. Hierarchical Nanolattice Design and Fabrication

Various sample geometries were tested to quantify the effect of architecture and relative density on mechanical behavior. The hierarchical nanolattices fabricated in this work are designed using a recursive method that combines different unit cells into hierarchical geometries. The design process takes place as follows: (1) two (unique or identical) unit cell geometries are prescribed, (2) one unit cell is designated 1st order and the other 2nd order, and (3) the 1st order unit cell is patterned along the length of the 2nd order unit cell with N repeating units, resulting in a fractal-like geometry. These steps can be repeated iteratively to create a fractal of any order, and the method is sufficiently general that it can be repeated for a wide range of unit cell geometries (Figure 17). For the samples tested in this work, 1st order axial support beams are added along the length of the 2nd order beam to ensure that the hierarchical beams form a stretching-dominated geometry. A more thorough explanation of the design process can be found in Appendix A. This design concept can be extended to create hierarchical metamaterials of any order with previously unobserved combinations of properties across multiple length scales—for example, high strength to weight ratios, tunable mass density, near-infinite bulk to shear modulus ratios (20, 21), and negative Poisson's ratios (18, 19).

Hierarchical nanolattices were fabricated from solid polymer, ceramic–polymer core-shell composites, and hollow ceramic tubes. Solid polymer lattices were written in negative photoresist (IP-Dip 780) using the Photonic Professional TPL-DLW System (Nanoscribe GmbH). Core-shell composites were created by depositing a conformal coating of 20 nm Al₂O₃ onto the polymer nanolattices using atomic layer deposition in a Cambridge Nanotech S200 ALD System with H₂O and trimethylaluminum (TMA) precursors. Hollow structures were made by removing the edges of the coated nanolattices using focused ion beam milling with the FEI

Nova 200 Nanolab and then etching out the internal polymer structure with oxygen plasma using the Zepto Plasma Etcher (Diener GmbH), resulting in the hollow ceramic nanolattice.

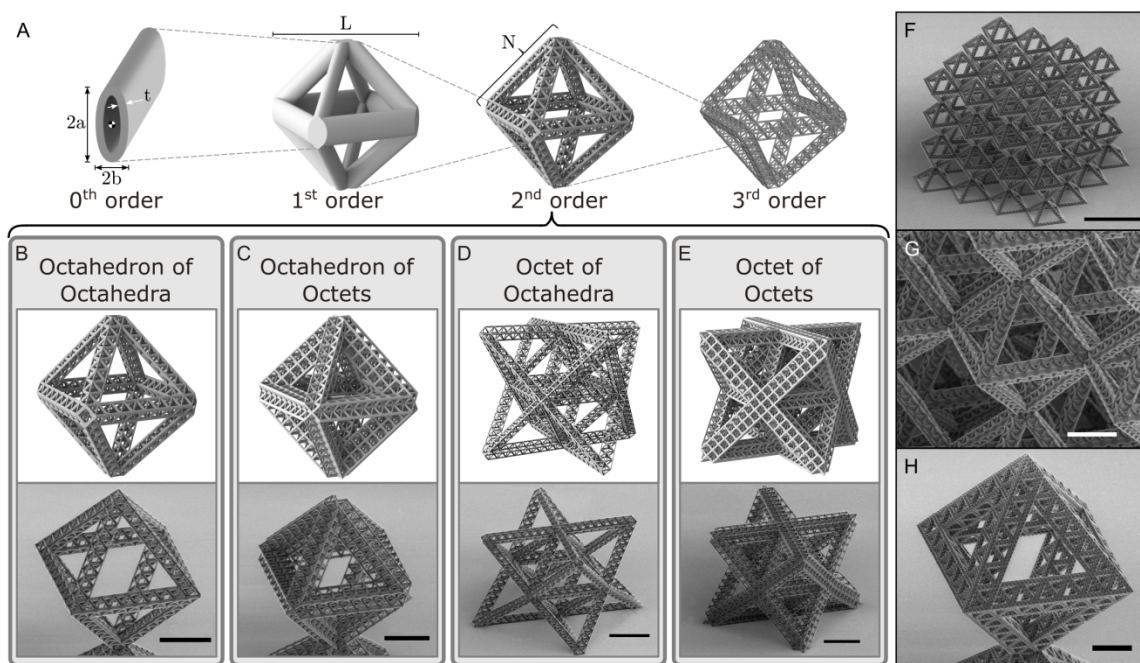


Figure 17: CAD and SEM images of hierarchical nanolattices.

A) CAD images illustrating the process of making a third-order hierarchical nanolattice. A 0^{th} order repeating unit, an elliptical beam, is arranged into a 1^{st} order octahedron; it becomes the repeating unit for a 2^{nd} order octahedron-of-octahedra, which is then arranged to create a 3^{rd} order octahedron-of-octahedra-of-octahedra. B-E) CAD and SEM images of the various 2^{nd} order samples. (Scale bars: $20\mu\text{m}$.) F) SEM image of a 2^{nd} order octahedron-of-octahedra lattice. (Scale bar: $50\mu\text{m}$.) G) A zoomed-in image of the 2^{nd} order octahedron of octahedra lattice showing the 1^{st} order repeating units that make up the structure. (Scale bar: $10\mu\text{m}$.) H) SEM image of a 3^{rd} order octahedron-of-octahedra-of-octahedra. (Scale bar: $25\mu\text{m}$.)

Two sets of samples were created: half-unit cells (half-cells) and full nanolattices. Three different types of half-cells were fabricated and tested: a 2^{nd} order octahedron-of-octahedra (Figure 17B), a 2^{nd} order octahedron-of-octets (Figure 17C), and a 3^{rd} order octahedron-of-octahedra-of-octahedra (Figure 17H). For the 2^{nd} order structures, two different base unit cell sizes (L) were used (8 and $12\mu\text{m}$), with three numbers of unit cells per fractal beam (N): 10 , 15 , and 20 . For the 3^{rd} order samples, two different octahedra-of-octahedra-of-octahedra were fabricated and tested with different geometric configurations: a unit cell with $L = 3\mu\text{m}$ and $N = 10$ and one with $L = 8\mu\text{m}$ and $N = 5$. Three different 2^{nd} order octahedron of octahedra full nanolattices were fabricated and tested: a unit cell with $L = 8$ and $N = 10$, one with $L = 6$

and $N = 15$, and one with $L = 4$ and $N = 20$. The inherent limitations of the two-photon lithography fabrication methodology used to create the nanolattices render it impractical to create materials with more than three orders of structural hierarchy. A full list of samples and structural parameters can be found in Table 10 to Table 12.

4.3. Experimental Setup

In-situ nanomechanical experiments were performed in a Quanta SEM (FEI Co.) using an InSEM Nanomechanical Module (Nanomechanics Inc.). All samples were compressed to $\sim 50\%$ strain at a strain rate of 10^{-3} s^{-1} . The load displacement data for each of the samples showed an initial linear region from which the effective loading stiffness was determined followed by an inelastic region with behavior that varied depending on the constituent material (Figure 18 and Figure 19). The structural stiffness was estimated based on the loading slope of the load displacement curve in the linear regime, and failure strength was taken to be the peak applied load before failure. The effective Young's modulus was calculated by normalizing the measured loading stiffness by the sample height divided by the footprint area. The effective yield strength was determined by dividing the measured peak load by the sample footprint area. Scaling relations were obtained using an exponential best fit of the stiffness data; the scaling is computed as the average of the fits of the two 2nd order half-cell geometries: the octahedron-of-octets and the octahedron-of-octahedra.

4.4. Hierarchical Nanolattice Deformation, Failure, and Recoverability

The characteristic failure and post-yield deformation of each sample were observed to correlate with material system and architecture. It was found that the material system (i.e., polymer vs. composite vs. hollow alumina) most strongly influenced the global deformation

behavior and that the architecture directly affected the localization of failure within the hierarchical beams and the global recoverability of the samples. Of all material systems, the hollow ceramic samples had the highest average recovery, with samples recovering up to 85–98% of their original height after compressions exceeding 50% strain (Figure 18A-C and Figure 19A-C). Polymer sample deformed in a ductile and continuous manner and samples recovered to ~ 75–90% of their original height after unloading (Figure 18G-I and Figure 19G-I). All of the composite samples demonstrated brittle catastrophic failure, with a majority exhibiting little to no recovery (Figure 18D-F and Figure 19D-F). More in-depth results from all the materials systems tested in this work are discussed in the following sections.

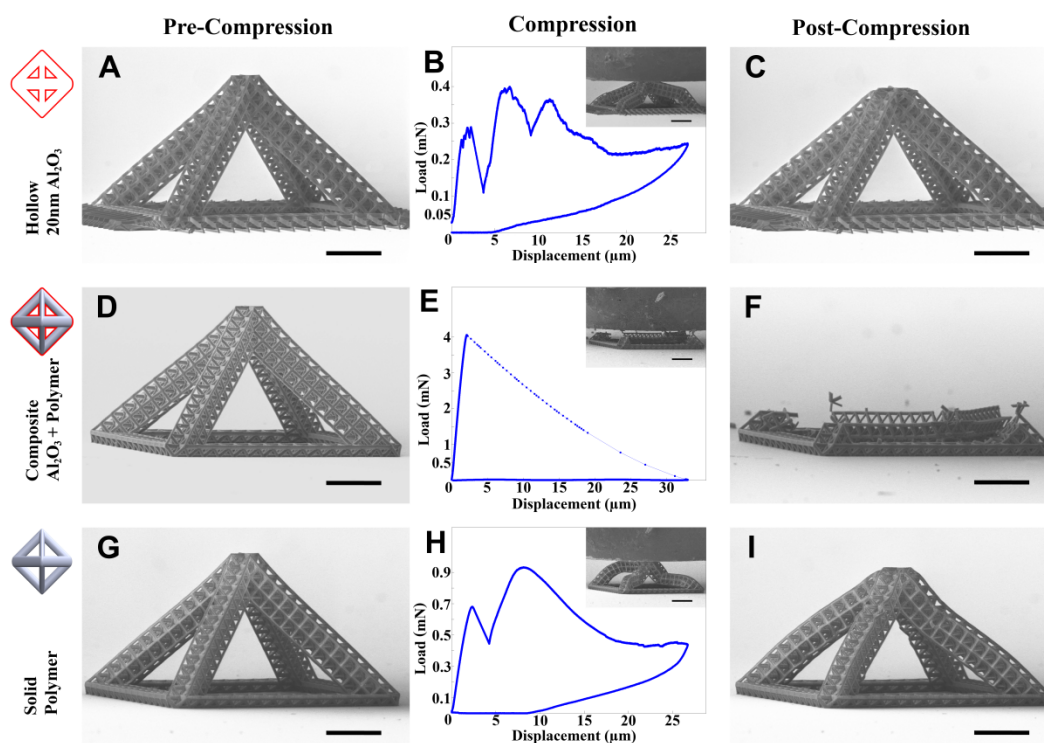


Figure 18: Compression of 2nd order octahedron-of-octet half-cells.

All samples shown here have $N = 15$ and $L = 8$. A-C) Compression and recovery of hollow 20-nm walled Al_2O_3 . Inset corresponds to 50% strain. D-E) Compression of composite sample. Inset corresponds to the sample after the occurrence of a strain burst. G-I) Compression and recovery of polymer sample. Inset corresponds to 50% strain. (Scale bars: $20\mu\text{m}$.)

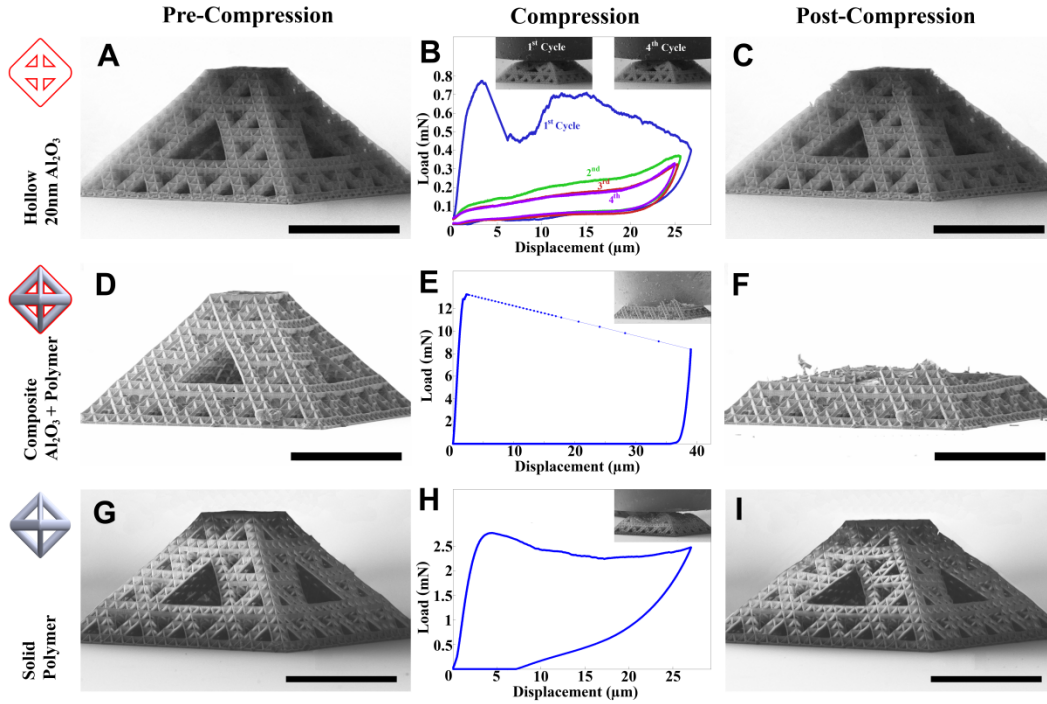


Figure 19: Compression of 3rd order octahedron-of-octahedra-of-octahedra half-cells.

All samples shown have $N = 5$ and $L = 8$. A-C) Compression and recovery of hollow 20-nm walled Al_2O_3 . Inset corresponds to 50% strain. D-E) Compression of composite sample. Inset corresponds to the sample after the occurrence of a strain burst. G-I) Compression and recovery of polymer sample. Inset corresponds to 50% strain. (Scale bars: $20\mu\text{m}$.)

4.4.1. Hierarchical Slenderness Ratios

The critical dimensionless geometric parameter for a beam, hierarchical or otherwise, is its slenderness ratio, defined as

$$\lambda = \sqrt{\frac{AL^2}{I}} \quad (34)$$

Here, A is the cross sectional area of a beam, L is its length, and I is the area moment of inertia. For a hierarchical beam, slenderness ratios can be defined at each level of hierarchy: $\lambda_1, \lambda_2, \dots, \lambda_n$. This slenderness ratio can be directly related to the critical stress required for buckling as

$$\sigma_{cr} = \frac{\pi^2 EI}{kL^2} = E_s \left(\frac{\pi}{k\lambda} \right)^2 \quad (35)$$

Here, k is a coefficient determined by the boundary conditions and E_s is the Young's modulus of the constituent material. This equation shows that a beam with higher slenderness is more likely to buckle than one with lower slenderness, as long as the slenderness is sufficiently high to initiate buckling.

There are two important characteristic parameters related to the slenderness ratio: the ratio between the slenderness of the beams and the average slenderness, defined as

$$H_{ij} = \frac{\lambda_i}{\lambda_j} \quad (36)$$

$$\lambda_{avg} = \frac{\lambda_1 + \lambda_2 + \dots + \lambda_n}{n} \quad (37)$$

These parameters don't relate directly to analytic equations that dictate failure behavior like the slenderness does in Equation (35), but they are used here to quantify different combinations of structural parameters in the hierarchical architectures. Many of the results shown in the following sections will be discussed in terms of the relative slenderness ratios for each respective geometry and material system. The full derivation of the hierarchical slenderness for each individual sample tested in this work can be found in Appendix D below.

4.4.2. 2nd Order Polymer Samples

2nd order polymer half-cells deformed in a continuous ductile manner throughout their compression and recovered to ~75 – 90% of their original height when unloaded from 50% strain (Figure 18G-I and Movie 8). Most samples exhibited an additional 5 – 10% recovery after being left in an unstressed state for an extended period of time. 2nd order polymer full nanolattice samples recovered immediately to 65 – 85% of their original height (Figure 20), with additional viscoelastic recoveries of 5 – 20% after unloading. This reduced recovery is largely due to the

emergence of a layer-by-layer collapse mechanism that led to highly localized strains and in turn large local deformations.

Failure in 2nd order polymer samples occurred primarily via a mix of localized Euler buckling in the 1st order beams and global buckling of the 2nd order beams. The beam with the highest slenderness λ will buckle at the lowest applied load, meaning that the failure can be well explained using the ratio between hierarchical slendernesses H_{12} . Samples with $H_{12} < 1$ failed via global buckling of the 2nd order beams because their relative slenderness was higher (Figure 20C, E-F). Samples with $1 < H_{12} < 1.5$ had a mix of local Euler and global buckling of the higher order beams indicating a transition between buckling in the 1st and 2nd order beams (Figure 20A, D, K). All samples with $H_{12} > 1.5$ failed via Euler buckling in the 1st order beams and displayed a short initial strain burst upon loading caused by the collapse of the top-most 2nd order node (Figure 18H-I and Figure 20B, G-I, L). Increasing H_{12} to > 2.25 led to a second burst via collapse of top-most 2nd order node (Figure 20G-H, K). This localized top node collapse can be explained by considering the higher stress concentration in the 1st order beams near the top. All of the parameters for the samples tested can be found in Table 10.

The polymer used to fabricate the hierarchical nanolattices is viscoelastic (IP-Dip, Nanoscribe GmbH), which gives rise to their ductile post-yield load-displacement behavior. The hierarchy leads to an enhanced recovery because failure is generally localized to buckling in highly strained 1st order beams while the majority of the beams deform elastically. In samples with buckling in 1st order beams, the area moment of inertia in the buckled section is reduced, which creates a compliant hinge that accommodates most of the deformation and results in greater local strains (Figure 18H, Figure 19H, Figure 20A-B, D, F-I). In samples with buckling in 2nd order beams, a characteristic buckling stiffness drop occurs without any localization of

strain in the 1st order beams (Figure 20C, E). After the onset of buckling, highly strained buckled regions deform plastically, which causes local residual strains that prevents global recovery. Some of this residual strain can be alleviated via viscoelastic recovery, which may explain the observed additional 5 – 10% recovery after the removal of the load. In the 2nd order full nanolattices, failure occurs through layer-by-layer collapse via buckling and the activation of different structural mechanisms. This deformation mode leads to high local stresses in the beams and in the nodes and reduces the global recoverability.

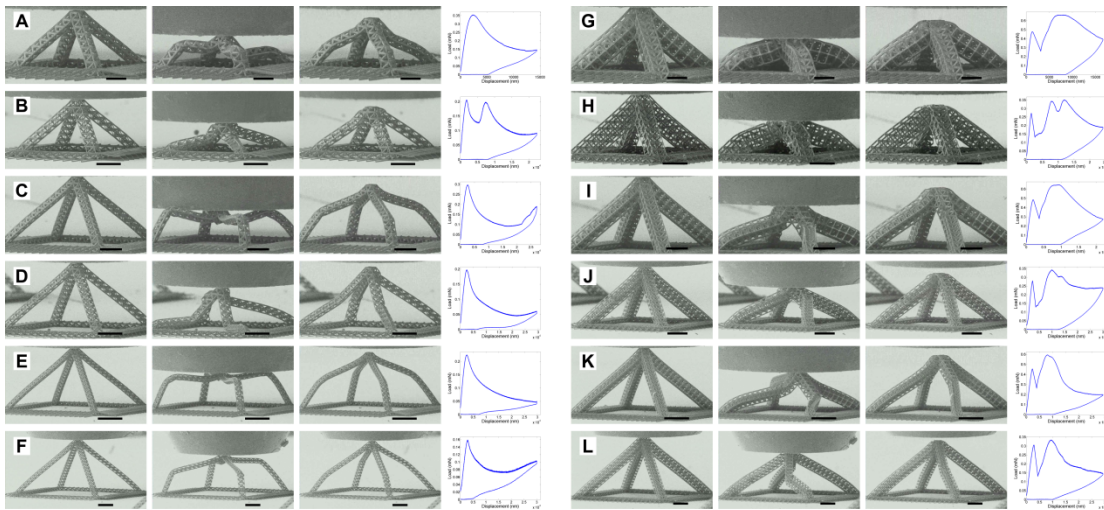


Figure 20: All compression experiments on 2nd order polymer half-cells.

All figures show the samples in an undeformed configuration, at 50% strain, and unloaded, along with the corresponding load (mN) vs. displacement (μm) data. Samples (A-F) are octahedrons-of-octahedra half-cells, and samples (G-L) are octahedrons-of-octets. The samples shown have the following structural parameters: A) $L=8\mu\text{m}$ and $N=10$, B) $L=12\mu\text{m}$ and $N=10$, C) $L=8\mu\text{m}$ and $N=15$, D) $L=12\mu\text{m}$ and $N=15$, E) $L=8\mu\text{m}$ and $N=20$, F) $L=12\mu\text{m}$ and $N=20$, G) $L=8\mu\text{m}$ and $N=10$, H) $L=12\mu\text{m}$ and $N=10$, I) $L=8\mu\text{m}$ and $N=15$, J) $L=12\mu\text{m}$ and $N=15$, K) $L=8\mu\text{m}$ and $N=20$, and L) $L=12\mu\text{m}$ and $N=20$.

4.4.3. 2nd Order Composite Samples

2nd order composite half-cells underwent a linear elastic deformation and then failed via a catastrophic brittle collapse with little to no post-yield recovery (Figure 18 and Movie 9). This behavior was replicated in the full 2nd order nanolattices. Three characteristic failure modes were observed: (1) complete catastrophic collapse, (2) gradual brittle crushing, and (3) partial collapse. These characteristic failure modes are well quantified using the slenderness of the 1st and 2nd order beams λ_1 and λ_2 and the average slenderness ratio λ_{avg} .

In the sample, beams are subjected to a mix of compressive and bending stresses. The bending moment M scales with length as $M \propto L^{-2}$, meaning less slender beams will have a greater stress concentration. In a hierarchical beam this means a smaller fraction of the bars carry the load, so failure of a single bar will lead to a more catastrophic failure. This is exemplified in samples with average slenderness $\lambda_{avg} < 36$, which experienced a complete catastrophic failure of all four 2nd order beams with no recovery (Figure 18E-F and Figure 21A, C, G-I, K). In these samples, failure was localized to the lowest section of the 2nd order beams, which is the region of highest stress concentration (Figure 26). Samples with average slenderness $36 < \lambda_{avg} < 40$ experienced a small catastrophic collapse followed by a gradual brittle crushing of the 2nd order beams with marginal recovery of $\sim 5\%$ (Figure 21B, J, L). In these samples λ_2 is at least a factor of 2 lower than λ_1 , which drives the failure towards 2nd order beams and gives rise to a gradual brittle crushing that is localized to the upper- and lowermost regions of the 2nd order beams. Samples with average slenderness $\lambda_{avg} > 40$ exhibited catastrophic failure with a complete fracture of two of the 2nd order beams and a partial fracture of the other two; the two surviving beams remained intact throughout their compression and recovered to 80 – 95% of their original height (Figure 21D-F). In these samples both λ_1 and λ_2 are large, so stress is more evenly distributed throughout the beams and failure of a single beam re-distributes the applied load among the remaining beams, preventing global failure in the sample. In all the composite samples there was no observable correlation between the failure mode and H_{12} .

All of composite samples exhibited brittle failure mechanisms and had no observed buckling in any beams despite both the constituent materials exhibiting buckling behavior when isolated. This lack of observed buckling suggests that the presence of the polymer-ceramic interfaces suppresses Euler buckling failure in the polymer and the shell bending and local

buckling in the hollow samples. Failure in the composite samples appears to be governed by fracture of the ceramic tube walls, which experience greater stress than the polymer in the given isostrain loading configuration. At their yield point the ceramic walls will fracture, after which the isolated polymer is unable to support the high local loads and also fails. The strength and stiffness of the composite samples exceed the rule-of-mixtures sum of pure polymer and hollow alumina samples with the same geometry on average by a factor of 2 and 3 respectively (Figure 18E and Figure 19E), which implies that the hierarchical nanolattices are non-linear with respect to their mechanical properties.

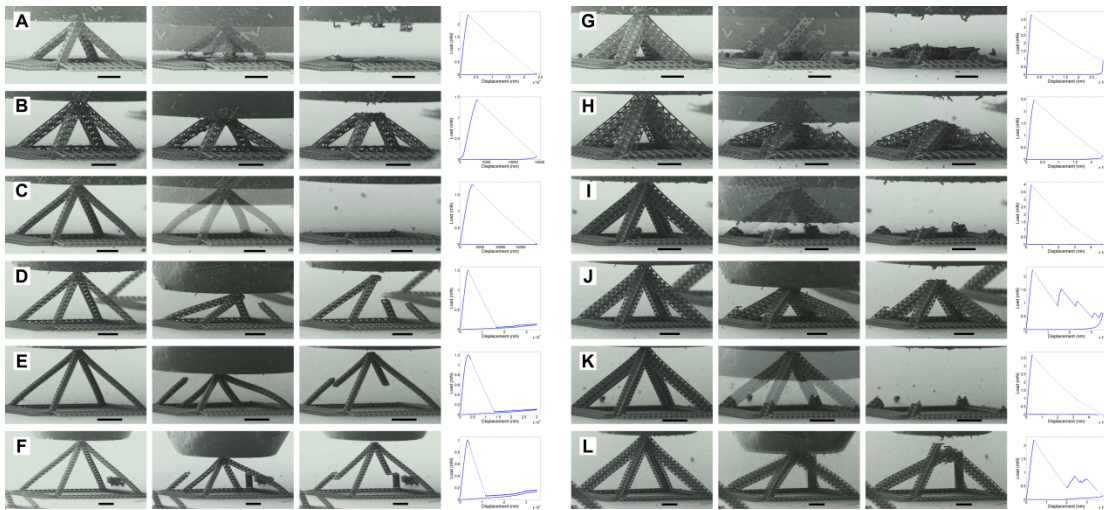


Figure 21: All compression experiments on 2nd order composite half-cells.

All figures show the samples in an undeformed configuration, at 50% strain, and unloaded, along with the corresponding load (mN) vs. displacement (μm) data. Samples (A-F) are octahedrons-of-octahedra half-cells, and samples (G-L) are octahedrons-of-octets. The samples shown have the following structural parameters: A) $L=8\mu\text{m}$ and $N=10$, B) $L=12\mu\text{m}$ and $N=10$, C) $L=8\mu\text{m}$ and $N=15$, D) $L=12\mu\text{m}$ and $N=15$, E) $L=8\mu\text{m}$ and $N=20$, F) $L=12\mu\text{m}$ and $N=20$, G) $L=8\mu\text{m}$ and $N=10$, H) $L=12\mu\text{m}$ and $N=10$, I) $L=8\mu\text{m}$ and $N=15$, J) $L=12\mu\text{m}$ and $N=15$, K) $L=8\mu\text{m}$ and $N=20$, and L) $L=12\mu\text{m}$ and $N=20$.

4.4.4. 2nd Order Hollow Al_2O_3 Samples

2nd order hollow half-cells deformed in a ductile-like manner with serrated continuous post-yield load-displacement data, and recovered to 85 – 98% of their original height after compression to 50% strain (Figure 18A-C and Movie 10). Failure occurred either by localized crushing of the 2nd order topmost node or localized Euler buckling of the 1st order beams, the initiation and progression of which was found to depend on the average slenderness λ_{avg} and the

ratio between beam slendernesses H_{12} . Similar to the failure in the polymer samples, H_{12} will dictate the competition in failure between 1st and 2nd order beams and change the localization of failure; similar to the failure in the composite samples, λ_{avg} will dictate stress concentrations in the beams and will alter how the surrounding structure responds when a single beam fails. This is exemplified in samples with $H_{12} > 1$, which generally experienced little to no failure along the length of the 2nd order beams and instead accommodated deformation through 1st order beam buckling and crushing of the topmost node (Figure 22B, G-H, J, and L). In samples with $H_{12} < 1$, 2nd order beams bend to accommodate the applied load, and failure localizes via buckling in a 1st order beam along the length of a higher order beam (Figure 18B and Figure 22A, C-F, I, K). Failure in samples with $\lambda_{avg} < 35$ initiated via Euler buckling in the top-most node and manifested as 1-2 small strain bursts during loading (Figure 18B-C and Figure 22A-C, G-L).

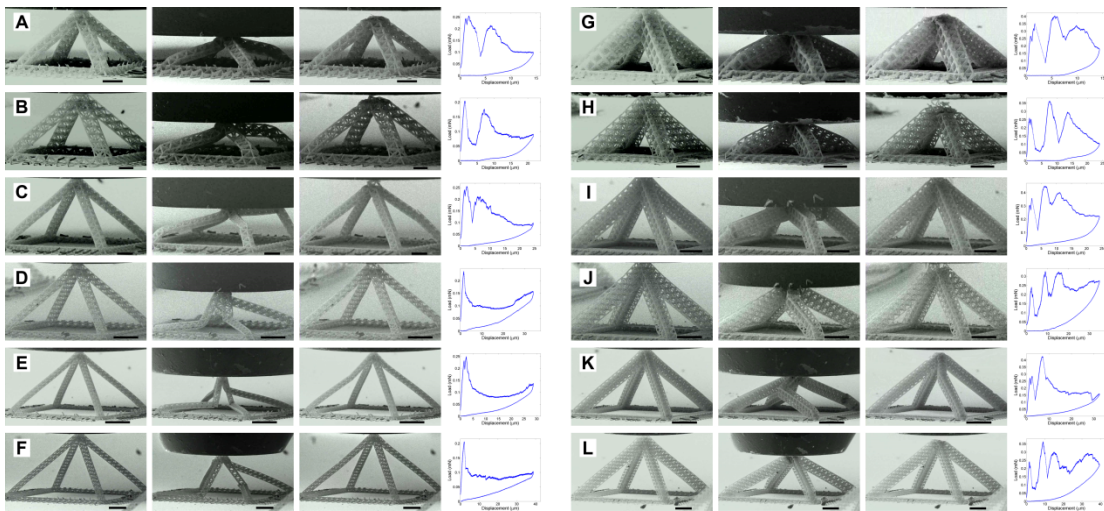


Figure 22: All compression experiments on 2nd order hollow Al_2O_3 half-cells.

Figures show the samples in an undeformed configuration, at 50% strain, and unloaded, along with the corresponding load (mN) vs. displacement (μm) data. Samples (A-F) are octahedrons-of-octahedra half-cells, and samples (G-L) are octahedrons-of-octets. The samples shown have the following structural parameters: A) $L=8\mu\text{m}$ and $N=10$, B) $L=12\mu\text{m}$ and $N=10$, C) $L=8\mu\text{m}$ and $N=15$, D) $L=12\mu\text{m}$ and $N=15$, E) $L=8\mu\text{m}$ and $N=20$, F) $L=12\mu\text{m}$ and $N=20$, G) $L=8\mu\text{m}$ and $N=10$, H) $L=12\mu\text{m}$ and $N=10$, I) $L=8\mu\text{m}$ and $N=15$, J) $L=12\mu\text{m}$ and $N=15$, K) $L=8\mu\text{m}$ and $N=20$, and L) $L=12\mu\text{m}$ and $N=20$.

The brittleness of the Al_2O_3 causes large local strains to be relieved either by elastic buckling or fracture, meaning there is no residual strain in the beams after unloading, enabling samples to globally recover virtually to their original shape after unloading. Further, in samples

that undergo local buckling in the 1st order beams, the locally buckled regions act as a compliant pivot point that accommodates large local strains and allows more of the structure to remain intact, which suppresses failure and enhances the recoverability of the samples.

As discussed in Section 3.4, shell buckling in a hollow ceramic tube ceramic can become a dominant deformation mechanism over brittle fracture when the wall-thickness-to-tube-radius ratio is below a critical transition value of $(t/a)_{cr} = \sigma_{fs}/E\sqrt{3(1-\nu^2)} \approx 0.03$. The t/a values for samples in this work range from 0.0163 to 0.0536, with most being below the critical transition ratio in the shell buckling regime (Table 10 to Table 12), meaning that shell buckling will dominate over brittle fracture as the constituent material failure mechanism. This is what gives rise to the ductile-like deformation observed in nearly all of the hollow samples.

Equating the shell buckling stress $\sigma_{sb} = E/\sqrt{3(1-\nu^2)}(t/a)$ to the Euler buckling stress $\sigma_{Eb} = \pi^2 E(b/L)^2$ for a hollow elliptical beam, a critical buckling-transition ratio is obtained of

$$\left(\frac{tL^2}{ab^2}\right)_{cr} = \pi^2 \sqrt{3(1-\nu^2)} \approx 16.3 \quad (38)$$

Samples with critical buckling ratios > 16.3 will preferentially Euler buckle; those with lower ratios will shell buckle. Buckling ratios for samples in this work range from 15.3 to 137.1, with most falling above the 16.3 transition value. This means a majority of failure will initiate via Euler buckling. This does not preclude shell buckling as a failure mode, and samples whose t/a is lower than the critical buckling ratio will shell buckle after a beam has undergone Euler buckling.

2nd order full Al₂O₃ nanolattice samples underwent layer-by-layer collapse and recovered to only 60 – 75% of their original height. All 2nd order full nanolattices had values of $H_{12} < 1$,

and failed nearly identically to the half-cells. During deformation, full nanolattices experienced layer-by-layer collapse which led to highly locally strained regions where the buckled beams partially fractured without complete failure (Figure 23C, F). The bifurcated beams likely experienced marginal recovery due to the residual strain energy being insufficient to return the sample to its original configuration. Preventing layer-by-layer collapse would improve recovery but requires a more efficient hierarchical geometry to optimize load distribution.

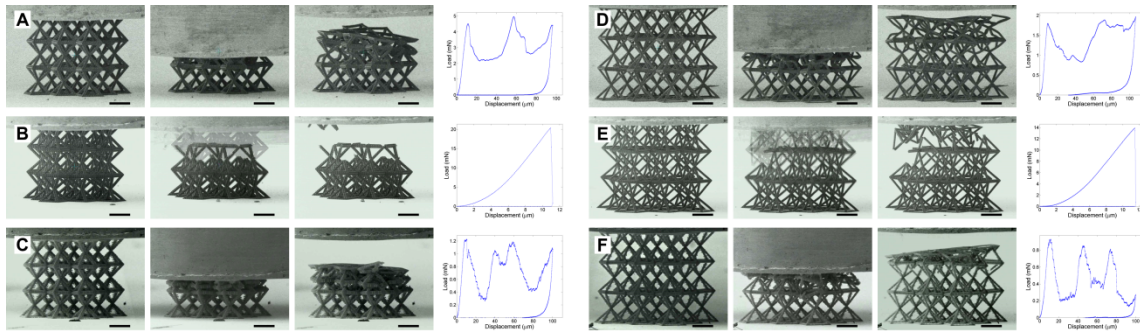


Figure 23: All compression experiments on 2nd order full-lattices.

Figures show the samples in an undeformed configuration, at 50% strain, and unloaded, along with the corresponding load (mN) vs. displacement (μm) data. All samples are octahedra-of-octahedra. Samples (A-C) have $L=8\mu\text{m}$ and $N=10$, and samples (D-F) have $L=6\mu\text{m}$ and $N=15$. Samples A and D are pure polymer, B and E are polymer-ceramic core-shell composites, and C and F are hollow Al_2O_3 .

4.4.5. 3rd Order Samples

The deformation behavior of 3rd order half-cells closely matches that of the 2nd order samples within each material system. Polymer 3rd order samples with $H_{12} > 1$ failed via local buckling in the 1st order beams (Figure 19h, Figure 24A and Movie 11); samples with $H_{12} < 1$ failed via local buckling in the 2nd order beams (Figure 24D). The relative 3rd order slenderness was never high enough to induce failure via buckling in 3rd order hierarchical beams. All 3rd order polymer samples were ductile during compression and showed some permanent residual strain after unloading (Figure 19I and Figure 24A, D). All 3rd order composite samples failed catastrophically. Samples with $\lambda_{avg} < 20$ completely collapsed (Figure 19F, Figure 24B, Movie 11); samples with $\lambda_{avg} > 20$ had two of the four 3rd order beams remain intact after the

catastrophic event (Figure 24E). Hollow 3rd order samples with $H_{12} > 1$ experienced local buckling and crushing of the topmost 3rd order node (Figure 19B and Figure 24C); samples with $H_{12} < 1$ locally buckled in the 2nd order beams along the length of the 3rd order beam (Figure 24F). All hollow samples had ductile-like load-displacement behavior during compression and recovered to $\sim 100\%$ over multiple loading cycles (Figure 19B, C, Figure 24C and Movie 13).

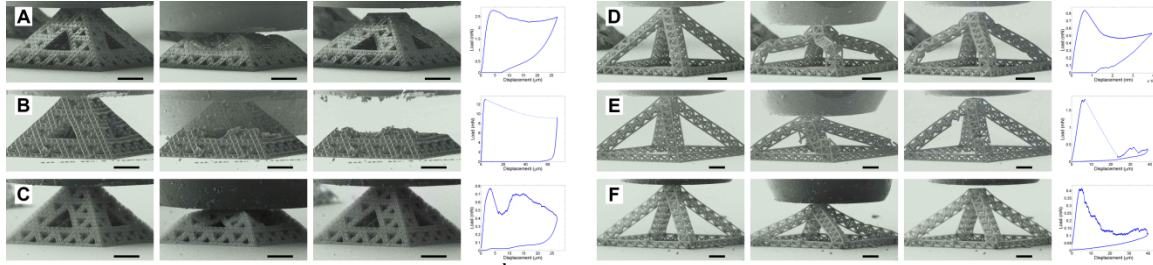


Figure 24: All compression experiments on 3rd order half-cells.

Figures show the samples in an undeformed configuration, at 50% strain, and unloaded, along with the corresponding load (mN) *v* displacement (μm) data. All samples are octahedra-of-octahedra-of-octahedra. Samples (A-C) have $L=8\mu\text{m}$ and $N=5$, and samples (D-F) have $L=3\mu\text{m}$ and $N=10$. Samples A and D are pure polymer, B and E are polymer-ceramic core-shell composites, and C and F are hollow Al_2O_3 .

Figure 19A–C shows cyclic experiments on a third-order hollow ceramic half-cell, which revealed, after the initial loading cycle, that the stiffness dropped from 420 to 39 N m^{-1} and that the applied load at yield decreased from 0.77 to 0.089 mN . In the first loading cycle, the sample recovered to 96% of the original height on unloading; all subsequent cycles showed nearly complete 100% recovery to this initial deformed height. The load displacement data quickly reached a stable hysteretic cycling behavior, with minimal degradation after the second loading cycle (Figure 19A–C and Movie 13).

4.4.6. Discussion on Recoverability

The underutilization of non-axially oriented beams plays a significant role in the ability of hierarchical nanolattices to recover. Axially oriented beams undergo failure at the point of highest stress in a sample; in the absence of a catastrophic failure event, non-axially oriented beams are able to remain intact. Under global compression, the undamaged non-axially oriented

first-order beams either efficiently distribute strain through bending or undergo local elastic buckling to accommodate large global deformation without failure. Having a large number of elastically deformed first-order beams enables the hierarchical samples to globally recover.

In the absence of residual strain in the buckled beams, such as is the case in hollow nanolattices, samples show excellent recovery behavior. The residual plastic strain in the buckled beams of polymer nanolattices impedes their ability to fully recover. In samples that undergo multiple loading cycles, most of the first-order beam buckling modes are activated in the first loading cycle; multiple loading cycles serve to reactivate the same buckling modes, which leads to near perfect recoverability of the initially deformed samples (Figure 19A-C). It may be possible to remove underused beams through better optimization of the hierarchical geometries, but such a reduction in the nonloadbearing beams may reduce the post-yield recoverability by impeding the recovery mechanism.

4.5. Strength and Stiffness Scaling with Density

4.5.1. Experimental Results

Second-order half-cell samples of varying material compositions were tested with densities spanning over two orders of magnitude from $\rho = 0.30 - 33.2 \text{ kg m}^{-3}$. Individual material systems had relative densities that spanned more than one order of magnitude. Strength and modulus in architected materials scale with relative density as

$$E = BE_s\bar{\rho}^m \quad (39)$$

$$\sigma_y = C\sigma_{ys}\bar{\rho}^n \quad (40)$$

Here, E_s and σ_{ys} are the constituent material's Young's modulus and yield strength, respectively; B and C are geometry-dependent proportionality constants, and n and m are scaling

constants (74). The experimentally measured stiffness in the hollow second-order half-cells was found to scale nearly linearly, with relative density as $E = 0.015E_h\bar{\rho}^{1.04}$ and strength as $\sigma_y = 0.026\sigma_{yh}\bar{\rho}^{1.17}$. Similar scaling relations were found for polymer and composite second order half-cell samples. Table 1 provides a full list of the constituent material properties used and the observed scaling parameters; polymer and composite properties can be found in Section 4.5.5 and Al_2O_3 properties were taken from (64, 68, 104–106).

Material Type	E_s (GPa)	σ_{ys} (MPa)	B (B^*)	m (m^*)	C	n
Polymer	2.10	62.7	0.110 (0.071)	1.12 (1.05)	0.316	1.36
Polymer + 20nm Al_2O_3	15.8	509	0.050 (0.062)	1.07 (1.04)	0.236	1.32
20nm Al_2O_3	165	5200	0.015 (0.036)	1.04 (1.00)	0.026	1.17

Table 1: Hierarchical nanolattice scaling relationships.

Material properties and proportionality and scaling constants for 2nd order half-cells as obtained from experiments and simulations. Stiffness constants in parenthesis represent simulation results.

The strength and stiffness of the second-order hierarchical half-cells follow analytical and computational predictions for stretching-dominated cellular solids (74). These results show a factor of 1.5 improvement in the scaling relationship for strength and a factor of 1.6 improvement in modulus over nonhierarchical hollow Al_2O_3 nanolattices (Figure 25). The strength and stiffness of the equivalently dense hollow third-order half-cell samples were found to be approximately a factor of two lower than those of second-order half-cells; under the same metric, polymer and composite samples had equivalent strength and stiffness for second- and third-order samples. Experimental and computational results for all second- and third order half-cells are summarized in Figure 25. Experiments on full second-order nanolattices revealed that the strength and stiffness align with second-order half-cell experiments.

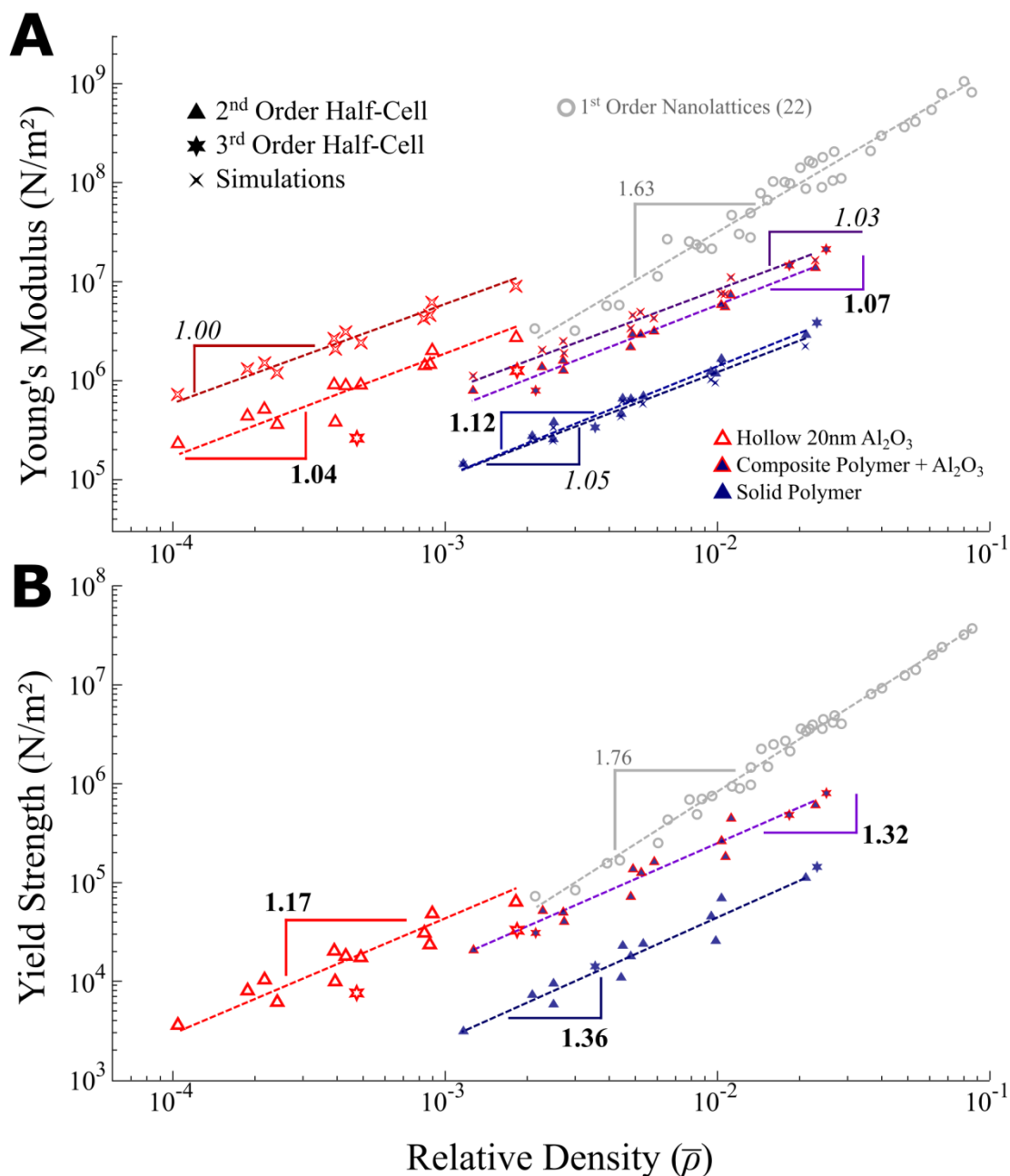


Figure 25: Comprehensive data plot of all tested hierarchical nanolattices.

A) Effective Young's modulus of the hierarchical structures plotted against their relative density. Data are plotted for experimental (slope values are in bold) and refined node simulations (slope values are italicized) results. B) Experimentally derived effective yield strength of the hierarchical nanolattices plotted against their relative density.

4.5.2. Computational Multiscale Modeling

In collaboration with Alex Zelhofer and Dennis Kochmann, numerical simulations were performed to measure the elastic response of second-order hierarchical nanolattices from all three material systems. Simulations revolved around a two-step computational strategy involving

Abaqus and an in-house variational-based solid mechanics code. In this method, first a characteristic stiffness of individual beams and lattice junctions was determined using finite element calculations with linear elastic shell and solid elements. It is assumed that the cross-sections of both ends of a beam deform rigidly through kinematic constraints, meaning the deformation of each beam and joint depend only on the displacements and rotations of its end points. Second, the thus-obtained load-displacement relations and stiffness matrices are input into an efficient simulation of the complete hierarchical structure based on the reduced degrees of freedom of all beam members and junctions in the lattice.

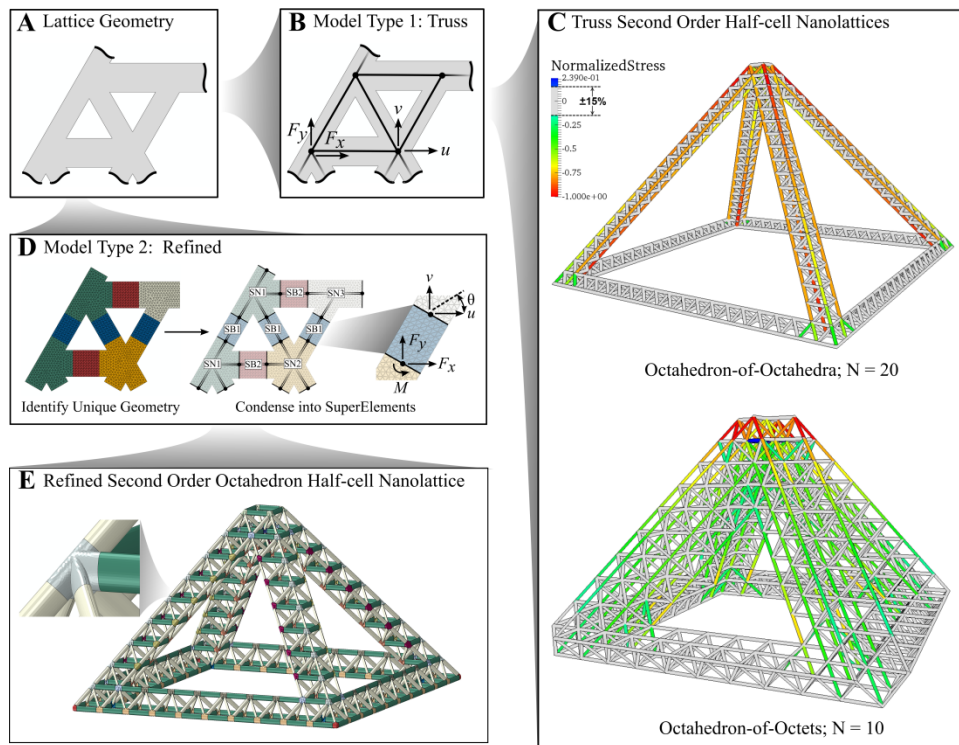


Figure 26: Model flowchart showing truss and refined model generation.

A) Representative lattice geometry section. B) Creation of a truss model lattice. C) Example compression of truss model half-cell nanolattices. Stress is normalized by the maximum compressive stress in the sample, and stresses $|\sigma| \leq 15\%$ of the maximum stresses have been grayed out to help illustrate the beams with high stresses. D) Refined model creation process containing geometrically unique supernodes (SN) and superbeams (SB). E) Example refined model half-cell nanolattice colored by unique geometry beam or node.

The response of 12 second-order lattices of varying architecture was modeled by the aforementioned procedure. Computed scaling exponents are included in Table 1 and show good

agreement with experiments, differing by only 6.1%, 3.3%, and 3.9% for polymer, composite and hollow trusses, respectively. The absolute computed stiffnesses were, on average, 10.7% lower for polymer, 30.2% higher for composite, and 68.5% higher for hollow samples compared with experimental data, which hints that geometric and/or material imperfections contribute significantly to a reduction in the effective stiffness. A summary of the results is shown in Figure 25.

4.5.3. Comparison between Experimental Results and Multiscale Modeling

Simulations reveal the local stress distribution and expose the load-carrying members of the hierarchical nanolattices. One prominent feature revealed by computations is that the first order axially oriented beams, which comprise $\sim 8.1\%$ of all of the beams in an individual sample, carry an average of 91% of the load. This has multiple implications for the global mechanical behavior of the hierarchical nanolattices. First, it is postulated that the near-linear strength and stiffness scaling observed arises from the combination of axially loaded first-order beams and the reduced effects of bending on global compliance. Because most of the load is carried in compression – which scales linearly with relative density – the global stiffness trends will also be linear with respect to their relative density. Second, this low percentage of load carrying beams suggests that the remaining beams within the structure are underused. The underutilization of non-axially oriented beams is likely a major factor in the observed reduction of the proportionality constants B and C (Equations 39 and 57) from what is predicted analytically for an ideal stretching-dominated solid, which have $B = C \approx 0.3$ (74). The negative impact of underused beams could be improved through better optimization of the hierarchical geometries.

Figure 26C illuminates the regions of high local stress revealed by computations in second-order samples with varying degrees of slenderness. Samples with low slenderness have stress concentrations highly localized to the topmost first-order beams and are more likely to experience failure there. Samples with high slenderness have a more even stress distribution throughout their length and are more likely to have failure initiate away from the topmost region. This stress localization trend agrees well with experimentally observed locations of failure. Failure in the structure will manifest itself as buckling, which is normally non-linear with respect to relative density, but because the relative density of the sample can be tuned relatively independently of the slenderness of the 1st order beams, the global strength scaling can be greatly improved over that of a traditional buckling dominated solid.

4.5.4. The Role of Imperfections

The marked overestimation of the absolute stiffness obtained by the refined model simulations compared with experiments can be explained by the presence of geometric imperfections in the fabricated samples. Defects, like misaligned nodes, prebending of the beams and variations in the wall thickness negatively impact the mechanical performance of nanolattices (96, 107). One dominant imperfection that was observed in all tested samples is sinusoidal waviness of the first order beams caused by the external vibrations during the two photon writing process. Simulations of the compression of beams with varying degrees of waviness and material compositions showed that, for a wave amplitude of 50 nm and a wavelength of 1 μ m, the calculated effective stiffness of polymer beams decreased by 5%, that of the ceramic-polymer composites decreased by 32%, and that of the hollow ceramic beams decreased by 70%, which serve to illustrate the increased sensitivity to defects in the composite and hollow beams. The simulations over-predicted the stiffnesses of composite and hollow

ceramic hierarchical lattices by 30.2% and 68.5%, respectively, which suggests that waviness-induced defects significantly contribute to this reduction. Model inaccuracy in under-predicting solid polymer stiffness by 10.7% can likely be attributed to the uncertainty in the polymer modulus.

4.5.5. Constituent Material Properties

Mechanical characterization of the IP-Dip polymer was performed through micropillar compression experiments in a nanomechanical testing device (TI 950 Triboindenter, Hysitron Inc.). Micropillars were compressed using a 20 μm diamond flat punch tip to 10 – 15% strain at a rate of 10^{-3} s^{-1} then held at their peak displacement for 50 s before unloading. Samples were fabricated out of IP-Dip photoresist using an identical DLW method to that described above for hierarchical nanolattices. Samples were fabricated and tested with diameters between 2 – 10 μm , and length-to-diameter (L/D) ratios between 2 and 4.

For each micropillar, stress-strain data was obtained and used to determine the Young's modulus (E) and compressive yield strength (σ_y). The Young's modulus is calculated using the slope of the linear regime of the stress-strain curve. The compressive yield strength is calculated by finding the intersection of the stress-strain data with a 0.2% strain offset curve from the linear regime. Three representative data sets along with their corresponding yield strength and stiffnesses are shown in Figure 27. The stress-strain data has an initial toe region followed by a linear regime and then a plastic flow region. The toe region is likely due to improper alignment or contact of the indenter tip with the sample, and was consequently ignored in the calculation of the Young's modulus. From the stress-strain data, it was found that the IP-Dip polymer had an

average modulus of $E = 2.1 \pm 0.3 \text{ GPa}$ and an average yield strength of $\sigma_y = 67.2 \pm 4.7 \text{ MPa}$.

These values are shown in Figure 27.

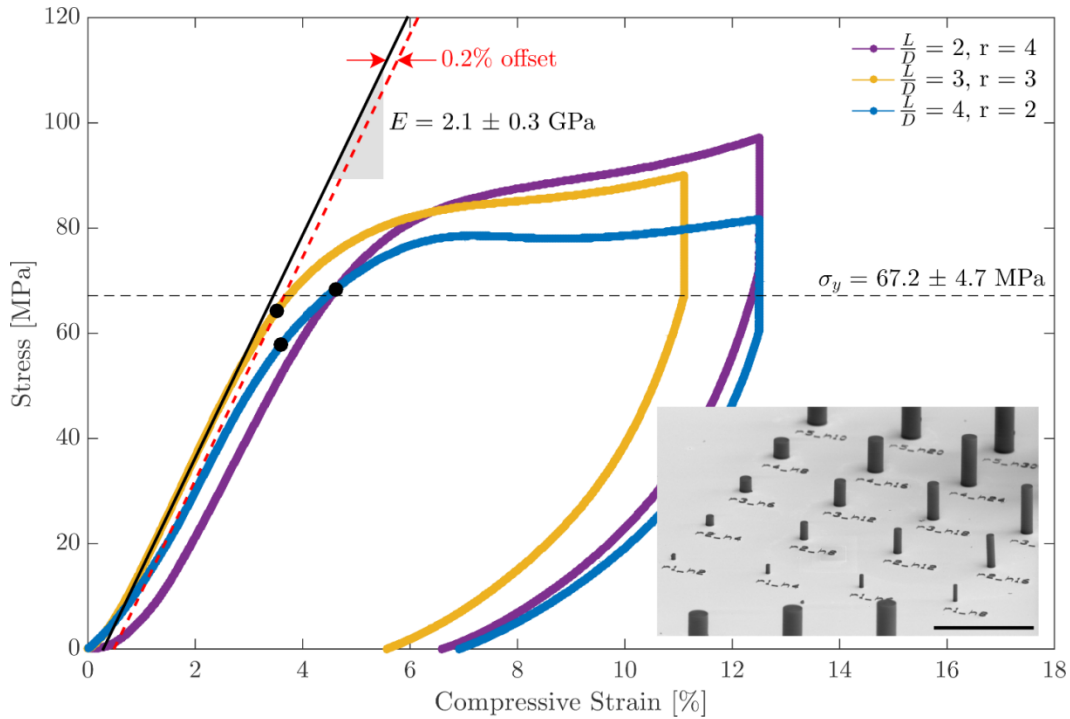


Figure 27: Representative stress-strain curves for polymer pillar compression.

Curves show each slenderness ratio tested ($L/D = 2, 3, 4$) with various radii. The arithmetic mean of the Young's modulus (E) and compressive yield strength (σ_y) are plotted. The inset image shows a set of pre-compression micropillar samples (scale bar: $50 \mu\text{m}$).

The properties of the composite were calculated using a Voigt model rule of mixtures, with the properties of the ALD Al_2O_3 taken from (64, 68, 104–106). In the 2nd order half cells, the polymer beams have dimensions of $a = 753\text{nm}$ and $b = 317\text{nm}$, where a and b are the major and minor radii of the ellipse respectively. The ceramic shell has a thickness of $t = 20\text{nm}$, meaning the volume fraction of polymer in the beams can be calculated to be $f = A_{\text{polymer}} / (A_{\text{polymer}} + A_{\text{ceramic}}) = 91.6\%$. Given the polymer properties of $E_p = 2.1 \pm 0.3 \text{ GPa}$ and $\sigma_{yp} = 67.2 \pm 4.7 \text{ MPa}$, and the ceramic properties of $E_h = 165 \text{ GPa}$ and $\sigma_{yh} = 5.2 \text{ GPa}$, the core shell composite properties are found to be $fE_p + (1 - f)E_h = E_c = 15.8 \text{ GPa}$ and $f\sigma_{yp} + (1 - f)\sigma_{yh} = \sigma_{yc} = 509 \text{ MPa}$.

Chapter 5: Mechanical Performance of Rigid vs. Non-Rigid Nanolattice Topologies

5.1. Chapter Summary

Traditional theories on the strength and stiffness of cellular solids indicate that there is a strong connection between the rigidity of a sample and the mechanical properties. In this work, a systematic series of mechanical tests were performed on rigid, periodically-rigid, and non-rigid truss topologies made from solid polymer and hollow aluminum oxide (Al_2O_3) beams to study their strength, stiffness, and deformation response. Across all topologies and the two material systems, a near identical scaling of strength and stiffness with relative density was found, diverging from previous theories on the strength and stiffness of “bending” and “stretching” dominated topologies. The mechanical behavior of polymer samples across all topologies was found to correlate strongly with the slenderness of the beams, and there was an observed transition between yielding-dominated and buckling-dominated samples. The mechanical behavior of Al_2O_3 samples across all topologies was found to correlate with the wall thickness-to-radius ratio (t/a) of the beams, and there was an observed transition between yielding-dominated and shell buckling-dominated behavior. Nanolattice samples were also made to study the effect of angle changes, missing beams, and offset nodes on the mechanical properties.

5.2. Defining Rigidity of a Structure

A structure comprised of bars connected by pin-jointed links is defined to be ‘rigid’ if any shape change of the structure requires a corresponding increase in the strain energy. Structures that are non-rigid are kinematically indeterminate because they can change shape without any applied load in their members. Any motion that is able to change the shape of a

structure without increasing strain energy is known as a *structural mechanism*. Structures that are rigid can be statically determinate or statically indeterminate. A structure is statically determinate if the force in every bar can be coupled by a set of equilibrium equations to the force in every other bar; in this case, the number of equilibrium equations is equal to the number of unknowns. A structure is statically indeterminate if there is redundancy in the structure and there is a non-unique solution to the force in the bars; in this case, there are more equilibrium equations than unknowns. A force that can be applied in a structure without a corresponding shape change is referred to as a state of *self-stress*.

The first attempt at describing the rigidity of a structure came in 1864 from James Maxwell (108). In this, he considered a structure with j joints and b bars subject to k kinematic constraints in d dimensions. With these, a structure has the potential to be rigid if it satisfies the equation

$$dj - b - k \leq 0 \begin{cases} d = 2 \text{ in 2D} \\ d = 3 \text{ in 3D} \end{cases} \quad (41)$$

This equation is necessary but not sufficient to determine the rigidity of a structure. In order to make the equation more accurate, structural mechanisms and states of self-stress must first be accounted for. For a structure with m mechanisms and s states of self-stress, Equation 41 can be generalized to

$$dj - b - k = m - s \quad (42)$$

A structure that is rigid will have $m = 0$, and a structure that is non-rigid will have $m > 0$. It isn't possible to determine the number of mechanisms or states of self-stress from this equation, but if either is known it is possible to determine the other. Examples of structures with different numbers of mechanisms and states of self-stress are shown in Figure 28 below.

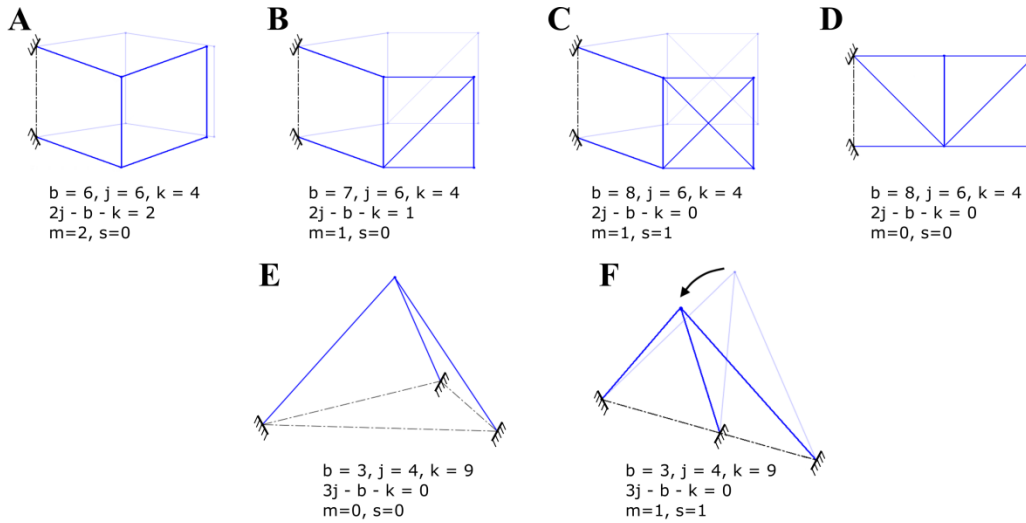


Figure 28: Examples of rigid and non-rigid structures

A-D) are examples of how bars can be arranged in a 2D structure with the same number of joints and kinematic constraints to give rise to different numbers of mechanisms and states of self-stress. E-F) are an example of how the position of joints in a 3D structure can change the number of mechanisms and states of self-stress even for structures with the same number of bars, joints, and kinematic constraints.

To obtain a more mathematically rigorous definition of the rigidity of a structure, one must formulate an equilibrium matrix that relates the forces at the nodes to the displacement of the bars, as was shown by Pellegrino and Calladine in 1986 (77). In this analysis, a vector $\mathbf{f} \in \mathbb{R}^{d \cdot j - k}$ can be defined that represents the force in each dimension d at the nodes j of a structure. The force on a node with a kinematic constraint k in that direction is ignored. It is also possible to define a vector $\mathbf{t} \in \mathbb{R}^b$ that represents the tension (or compression) in each of the bars of a structure. Correspondingly, a vector $\mathbf{d} \in \mathbb{R}^{d \cdot j - k}$ can be defined that represents the displacements at the nodes of a structure and a vector $\mathbf{e} \in \mathbb{R}^b$ that represents the elongations of the bars. These vectors can be related to each other using an equilibrium matrix $\mathbf{A} \in \mathbb{R}^{(d \cdot j - k) \times b}$ representing a force balance between bars and joints and an equilibrium matrix $\mathbf{B} \in \mathbb{R}^{b \times (d \cdot j - k)}$ representing a displacement balance between joints and bars as

$$\mathbf{f} = \mathbf{A} \mathbf{t} \quad (43)$$

$$\mathbf{e} = \mathbf{B} \mathbf{d} \quad (44)$$

These equilibrium matrices \mathbf{A} and \mathbf{B} can be used to determine the number of mechanisms and states of self-stress. If there is a nullity in matrix \mathbf{A} , there is set of bar tensions \mathbf{t} that can be applied that don't change the forces or corresponding displacements of the nodes, meaning it is a state of self-stress. If there is a nullity in matrix \mathbf{B} , that means a displacement \mathbf{d} can be applied to the nodes without a corresponding stretch in the bars, meaning there is a structural mechanism. It is possible to show that $\mathbf{A} = \mathbf{B}^T$, so the rank of \mathbf{A} is equal to the rank of \mathbf{B} . From linear algebra, the dimension of the nullspace of a matrix $\mathbf{C} \in \mathbb{R}^{p \times q}$ with rank r is $q - r$ and the dimension of the nullspace of \mathbf{C}^T is $p - r$. Therefore, the number of mechanisms and states of self-stress can be defined to be

$$m = (3j - k) - r_A \quad (45)$$

$$s = b - r_A \quad (46)$$

Here, r_A is the rank of the equilibrium matrices. It is therefore possible to determine the rigidity of a structure through setting up an equilibrium matrix and finding its rank, thereby determining the number of mechanisms in a structure.

5.3. Design of Rigid and Non-Rigid Nanolattice Topologies

Four different nanolattice topologies were designed and fabricated in this work using two different constituent materials, hollow Al_2O_3 and solid polymer, as model systems. The four topologies and corresponding average nodal connectivities Z are: octet-truss ($Z = 12$), cuboctahedron ($Z = 8$), 3D Kagome ($Z = 6$), and tetrakaidecahedron ($Z = 4$). An octet-truss is a fully rigid topology composed of a close packing of octahedrons and tetrahedrons. A cuboctahedron is a periodically rigid topology composed of octahedrons connected at their nodes. A 3D Kagome lattice is a periodically rigid topology composed of tetrahedrons connected at their nodes. A tetrakaidecahedron, also commonly known as a Kelvin foam, is a fully non-

rigid topology. The cuboctahedron and 3D Kagome lattice are periodically rigid because their constituent sub-units, an octahedron and a tetrahedron respectively, are rigid and periodically organized in the structure, meaning that most deformation modes will involve a periodic deformation of the rigid sub-units.

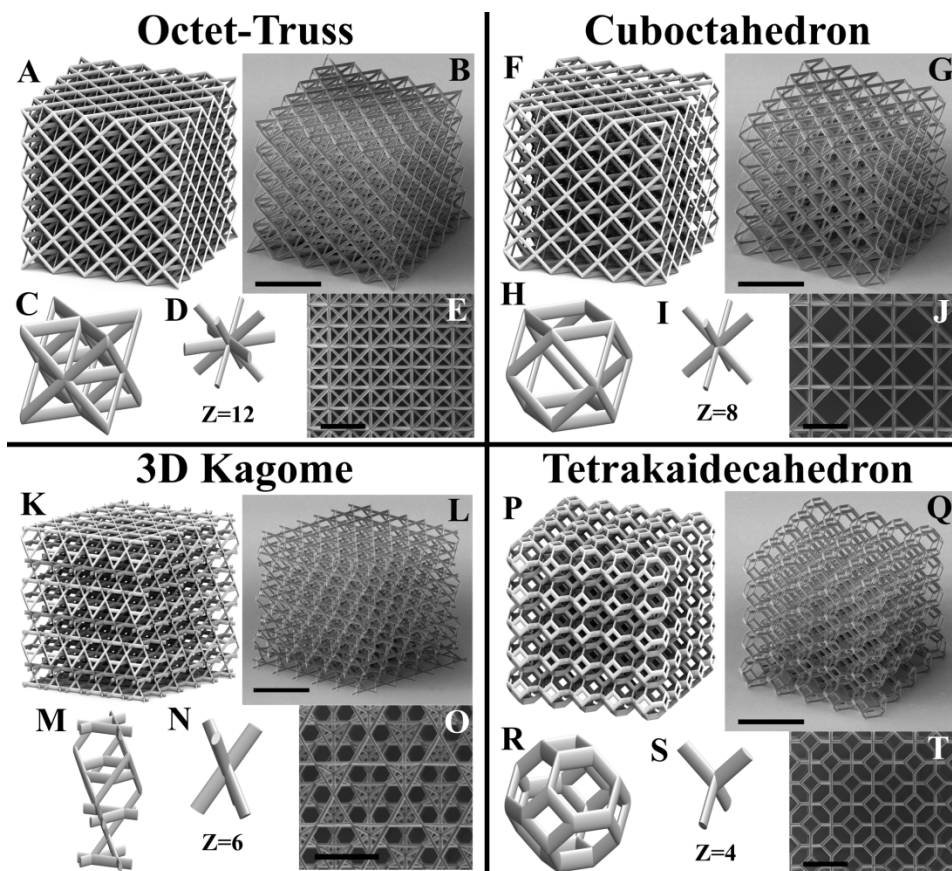


Figure 29: Rigid and non-rigid nanolattice topologies.

These figures show each of the four nanolattice topologies tested in this work: an octet-truss, cuboctahedron, 3D Kagome, and tetrakaidecahedron. Figures A, F, K, and P are CAD models of the full structures, B, G, L, and Q are SEM images of the full structures, C, H, M, and R are CAD models of the unit cells, D, I, N, and S are representative nodes showing the average nodal connectivity, and E, J, O, and T are SEM images from the top of the structures. The scales bars in B, G, L, and Q are $10\mu\text{m}$, and the scale bars in E, J, O, and T are $5\mu\text{m}$.

Each of the four nanolattice topologies were created with solid polymer beams and hollow Al_2O_3 beams. All of the samples had relative densities that spanned at least one order of magnitude. In polymer samples, the relative density was tuned by changing the size of the unit cell and the diameter of the beams. A full list of polymer samples tested can be found in Table 7. In hollow Al_2O_3 samples, the relative density was tuned by changing the size of the unit cell, the

beam diameter and the wall thickness. A full list of hollow octet-truss samples tested can be found in Table 3, hollow cuboctahedrons are in Table 4, all three variants of hollow 3D Kagome lattices are in Table 5, and hollow tetrakaidecahedrons are in Table 6. All of the topologies were made with regular polyhedra, meaning they had beams of equal length. Two additional 3D Kagome lattices were made with shortened and elongated unit cells having a tetrahedron edge-face angle of 45° and 65° respectively (a regular tetrahedron has an edge-face angle of $\sim 54.7^\circ$).

In addition to the normal topologies, polymer octet-truss lattices were created with two types of intentionally introduced imperfections: missing beams and offset nodes. In the missing beam samples, beams were removed randomly from only horizontal members, only diagonal members, and from the entire structure. In the offset-node samples, the connectivity of the structure was left the same but the nodes were displaced in a random direction by a distance defined by a uniform random distribution. A full list of these fabricated samples can be found in Table 8 and Table 9 for the missing beam and offset-node structures respectively.

The fabrication of the samples was done with a combination of two-photon lithography and atomic layer deposition in a manner identical to that described in Section 3.2. Mechanical testing of all samples was performed in a manner identical to that described in Section 3.3.1.

5.4. Deformation Behavior and Transition between Failure Modes

5.4.1. Polymer Nanolattices

When investigating the deformation and failure of polymer nanolattices, it is first useful to define the slenderness ratio λ and the critical beam buckling stress σ_b of an elliptical beam. The slenderness ratio is defined as $\lambda = \sqrt{AL^2/I}$, where A is the cross sectional area, L is the

length, and I is the area moment of inertia of a beam. For an elliptical beam with semi-major and semi-minor axes a and b respectively, the maximum slenderness ratio can be found to be

$$\lambda = \frac{2L}{b} \quad (47)$$

The critical beam buckling stress $\sigma_b = \pi^2 EI / Ak^2 L^2$ can be defined in relation to the slenderness ratio as

$$\sigma_b = \frac{\pi^2 E}{(\lambda k)^2} \quad (48)$$

Here, E is the Young's modulus of the constituent material, and k is a constant that varies depending on the boundary condition. For a beam with a fixed-fixed boundary, $k = 1/2$, and for a beam with a pinned-pinned boundary, $k = 1$. In a lattice structure, beams are supported by a rigid elastic boundary at the nodes and the actual value of k likely lies somewhere between $1/2$ and 1 .

In a polymer lattice structure, the failure and subsequent deformation behavior is governed by a competition between beam buckling and yielding. Taking the yield strength of the constituent polymer to be σ_y , a transition between the two failure modes will occur at a slenderness value of

$$\lambda_{cr} = \frac{\pi}{k} \sqrt{\frac{E}{\sigma_y}} \quad (49)$$

Using constituent values of the polymer as found in Section 4.5.5, taking $k = 1/2$ gives a critical slenderness of $\lambda_{cr} \approx 35$, and taking $k = 1$ gives a critical slenderness of $\lambda_{cr} \approx 17$. Different topologies are observed to have different critical slenderness ratio transitions between failure and deformation behaviors. In octet-truss samples, the transition between buckling- and yielding-dominated behavior occurs at a slenderness of $\lambda \approx 35$, which corresponds to a structure

with beams that have a fixed-fixed boundary condition ($k \approx 1/2$). In cuboctahedron samples, the transition occurs at $\lambda \approx 30$ ($k \approx 0.6$), in the 3D Kagome it occurs at $\lambda \approx 25$ ($k \approx 0.7$), and in the tetrakaidecahedrons it occurs at $\lambda \approx 22$ ($k \approx 0.8$). This indicates there is a gradual shift between an effective fixed-fixed and an effective pinned-pinned boundary correlating with the rigidity of the structure. A fully rigid topology has no mechanisms that allow for local deformation of the structure, causing the node to behave more like a fixed boundary, while non-rigid topologies have more mechanisms that allow for local deformations of the structure, allowing the nodes to behave more like a pinned boundary. Example stress-strain curves showing the deformation of various nanolattice topologies and their transition between failure modes are shown in Figure 30 below, and a full list of all the geometries tested with their corresponding observed failure modes are in Table 7.

The competition between buckling and yielding manifests itself in the nanolattice behavior in two ways: in the initial yielding behavior and in the post-yield deformation behavior. With regard to the initial yielding behavior, samples that undergo buckling-dominated failure have a sharp transition between their elastic and post-yield states and also have a negative post-yield stiffness (Figure 30 A, B, E, F, I, J, M, and N). Buckling is a bifurcation event that corresponds to a beam snapping between two deformed states (80, 82), and this snapping gives rise to the sudden change in the observed loading stiffnesses. While buckling generally doesn't give rise to a negative stiffness, beams in the nanolattices are subject to combined axial loading and bending and failure in the samples occurs as a whole layer. The cumulative effect of these two factors leads to a catastrophic layer failure that results in a negative stiffness. Samples that undergo yielding-dominated failure have a gradual transition between their elastic and post-yield states and maintain a positive post-yield stiffness throughout compression (Figure 30 C, D, G, H,

K, L, O, and P). This behavior more closely matches the yielding behavior of a fully dense material, as would be expected for the less slender and denser samples.

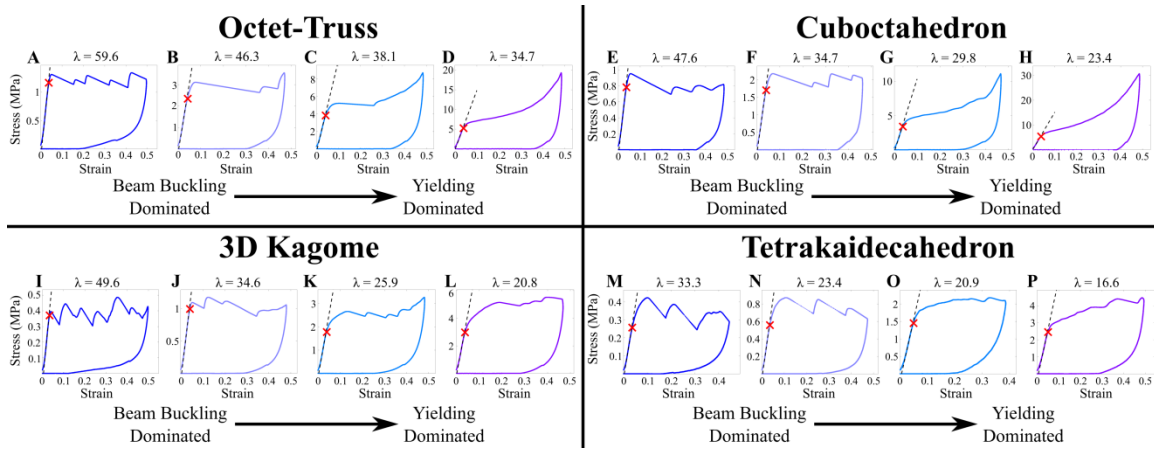


Figure 30: Stress-strain curves of different polymer nanolattice topologies.

These stress-strain plots show the transition between buckling-dominated and yielding-dominated failure for octet-truss (A-D), cuboctahedron (E-H), 3D Kagome (I-L), and tetrakaidecahedron (M-P) nanolattice topologies. The dashed lines and red X indicate the measured Young's modulus and yield strength respectively for each sample.

With regard to the post-yield deformation behavior, samples that undergo buckling-dominated failure have a serrated stress-strain response with a series of linear loading sections followed by drops in the stress. This serrated behavior corresponds with a periodic layer buckling, and larger strain bursts correspond to more layers failing simultaneously. Samples that undergo yielding-dominated failure will either plateau or gradually increase their stress until densifying. This densification occurs when the sample is effectively fully compressed and the stress-strain response is dominated by uniaxial beam-on-beam crushing instead of uniaxial beam compression, bending, and tension. A full list of the samples tested and their corresponding observed failure modes can be found in Table 7, and examples of the compression of different topologies can be found in Movie 14–Movie 17.

5.4.2. Hollow Al_2O_3 Nanolattices

There are two parameters that can be used to characterize the constituent structure of the hollow nanolattices: the wall thickness-to-radius ratio (t/a) and the slenderness ratio. The slenderness of a hollow thin walled beam can be calculated to be

$$\lambda_h = \frac{2L}{b} \sqrt{\frac{a+b}{3a+b}} \quad (50)$$

The deformation and failure behavior of the hollow nanolattices is observed to correlate strongly with the t/a ratio of the samples and has little to no correlation with the slenderness ratio. As discussed in Section 3.4, the failure of the hollow samples is primarily governed by a competition between shell buckling and brittle fracture. This competition can be expressed using the equation $(t/a)_{crit} = \sigma_{fs}/E\sqrt{3(1-\nu^2)}$ to relate the critical wall thickness-to-radius ratio at which shell buckling will be the dominant failure mode over fracture, where here σ_{fs} is the fracture strength of the constituent material. This critical wall thickness-to-radius transition will range between $(t/a)_{crit} \approx 0.0161 - 0.0262$ depending on the exact mechanical properties of the constituent Al_2O_3 (68).

There are four characteristic deformation signatures observed in the hollow nanolattices that are repeated across all topologies: gradual ductile-like failure, intermittent ductility with periodic strain bursts, multiple catastrophic strain bursts, and a single catastrophic strain burst. The transitions between these behaviors occur at approximately the same t/a values across all four topologies tested. Samples are observed to undergo gradual ductile-like failure when they have a $t/a \geq 0.02$, which coincides well with the transition into a shell buckling-dominated failure. The post-yield stress-strain profile of the ductile-like samples either plateaus (Figure 31A), which corresponds to a uniform crushing of the entire structure, or exhibits periodic

oscillations in the stress (Figure 31 D, G and J), which corresponds to a localized layer-by-layer failure. Both failure types are observed in all the different topologies to varying degrees, with octet-truss samples showing the most demonstrable plateauing behavior. Samples with $0.02 \leq t/a \leq 0.03$ are observed to have an intermittent ductile-like behavior with non-linear loading sections followed by small strain bursts (Figure 31B), which implies that this t/a ratio range is a transition region between shell buckling and fracture behavior. In these samples, the non-linear loading sections correspond to local shell buckling events, and the strain bursts correspond to brittle failure events in a layer of the sample.

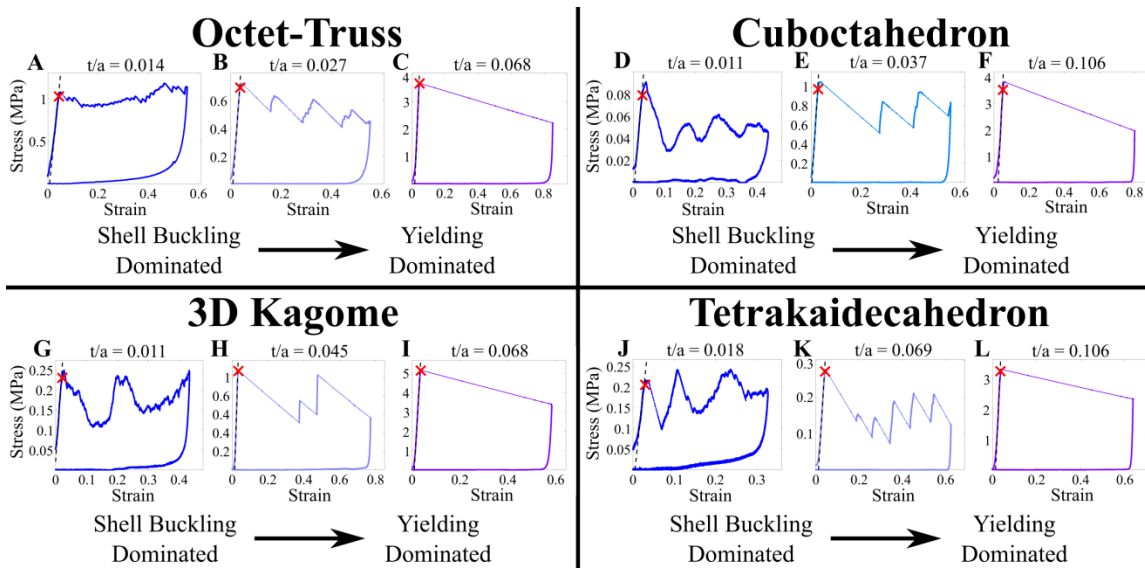


Figure 31: Stress-strain curves of different hollow Al_2O_3 nanolattice topologies.

These stress-strain plots show the transition between shell buckling-dominated and yielding-dominated failure for octet-truss (A-C), cuboctahedron (D-F), 3D Kagome (G-I), and tetrakaidecahedron (J-L) nanolattice topologies. The dashed lines and red X indicate the measured Young's modulus and yield strength respectively for each sample.

Samples with a larger $t/a > 0.03$ experience either multiple small strain bursts or a single large strain burst to failure (Figure 31 C, E, F, H, I, K, and L). These samples are strongly in a fracture-dominated failure regime, and all the strain bursts occur rapidly and with little to no recovery of the structure after yielding. There is no distinct range of t/a values or λ_h values that corresponds to the transition between having multiple strain bursts and a single catastrophic

strain burst, but in general samples that have a lower t/a value or a higher λ_h value are more likely to experience multiple strain bursts. This implies that the existence of a single strain burst or multiple strain bursts is likely due to a combination of structural parameters and imperfections in the samples.

These behaviors are similar to ones that have been described earlier in Section 3.3, and a more complete description of the behavior observed in the octet-trusses can be found there. A full list of the samples tested and their corresponding observed failure modes in the hollow samples can be found in Table 3–Table 6, and examples of the compression of different topologies can be found in Movie 18–Movie 21.

5.4.3 Discussion on Recoverability

A recoverability figure of merit, the percent strain recovery φ_r , will be used here in order to better characterize the recovery of different nanolattice topologies and different material systems. This is defined here to be the ratio between the strain recovered upon unloading and the maximum strain a sample is subjected to. This is equivalently defined as the maximum strain minus the residual strain divided by the maximum strain. Expressed as an equation, this becomes

$$\varphi_r = \frac{\varepsilon_{recovered}}{\varepsilon_{max}} = \frac{\varepsilon_{max} - \varepsilon_{residual}}{\varepsilon_{max}} \quad (51)$$

This ratio means that if a sample is compressed to 50% strain and recovers to 95% of the original height, it will have a φ_r of 90%, and if a sample is compressed to 50% strain and recovers to 55% of the original height, it will have a φ_r of 10%. This ratio is defined to minimize the effect of variations in maximum applied strain on the recoverability of the samples.

All the polymer samples were observed to have recoveries upon unloading of between $\varphi_r = 25\% - 86\%$, with an additional $\varphi_r = 5 - 15\%$ after being allowed to settle for 1-2 hours.

The additional recovery arises due to the viscoelastic nature of the constituent polymer. The percent strain recovered generally correlates with the relative density, with structures that have lower relative densities recovering more on average. The structures with the highest relative densities also recovered slightly more than average, but there is not a strict relationship between recoverability and relative density (Figure 32A). There is also a slight correlation between slendernesses and recoverability; samples with a higher slenderness recovered more on average, but there was a very weak correlation (Figure 32B). There wasn't a notable deviation in the recoverability of any of the topologies except for the tetrakaidecahedron, which had higher average recoverability, although this may be related to the lower average relative density of the samples. A full list of the polymer recoverabilities can be found in Table 7.

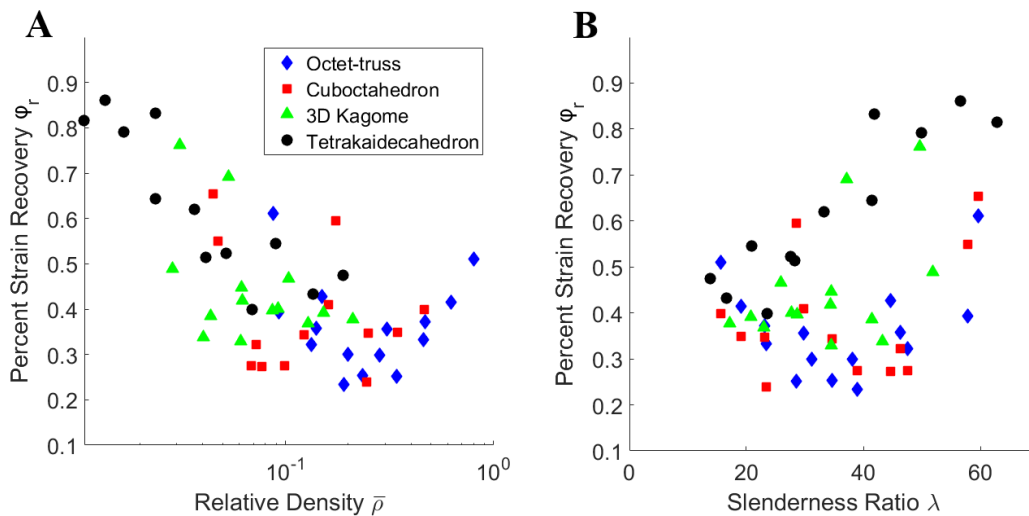


Figure 32: Recoverability of polymer nanolattice topologies.

A) Percent strain recovery ϕ_r versus the relative density $\bar{\rho}$ plotted on a log scale for all of the nanolattice topologies. B) Percent strain recovery ϕ_r versus the slenderness ratio λ also for all of the nanolattice topologies.

The recoverability of the polymer samples can be explained by considering two factors: the localization of strain in the beams and the localization of strain in the full nanolattices. In samples with beams that have a high slenderness, the beams are more likely to undergo buckling-dominated failure. Buckling is an elastic phenomenon, but high local strains in a post-buckled beam can lead to plastic deformation. If a beam is highly slender it will likely buckle and remain

entirely in the elastic regime throughout its deformation; if a beam is less slender but still undergoes buckling it is more likely to have high local stresses in its post-buckled state, leading to permanent plastic strain and less recovery. Buckling also generally localizes itself to an entire layer in the nanolattices. This leads to high local strains and as a result less global recovery. The greatest amount of permanent strain in a structure is observed to occur in regions that have localized collapse (Figure 34). If beams in a sample are less slender there will inherently be more plastic deformation, but the strain distribution in the samples may be more uniform, thereby leading to better recovery. This is likely the cause of the improved recovery of the samples with the highest relative density. Examples of the compression of different polymer nanolattices from each of the four topologies tested with their corresponding φ_r can be found in Figure 34.

All the hollow Al_2O_3 samples were observed to have recoveries upon unloading between $\varphi_r = 2\% - 92\%$. This recoverability was observed to strongly correlate with the t/a ratio of the samples, with samples that have $t/a < 0.02$ generally exhibiting much higher recovery than samples with $t/a > 0.02$. While there are still samples that have $t/a < 0.02$ that don't exhibit a significant recovery, all samples that had $\varphi_r \geq 50\%$ fell within the $\frac{t}{a} < 0.02$ regime (Figure 33A). There was a general correlation of relative density with the recoverability (Figure 33B), but that correlation likely arises because of the strong connection between relative density and the wall thickness to radius ratio of the structure (Appendix B). There was a weak correlation between slenderness and relative density, and structures with a lower slenderness had a slightly higher average recoverability, although the effect is minimal (Figure 33C). The recoverability was not observed to vary significantly between different topologies with the same t/a . A full list of the recoverability of the samples tested can be found in Table 3-Table 6.

The failure of samples with a $t/a < 0.02$ is primarily dominated by shell buckling. Shell buckling is an elastic phenomenon, and in theory, samples that strictly undergo shell buckling with no plastic yielding or fracture should experience 100% recovery. In real samples, shell buckling leads to local stress concentrations that cause cracking in the shell, particularly near the nodes (Section 3.6). If the t/a ratio is sufficiently small to prevent a complete fracture of the node in the post-buckled state, the structure will be able to recover. The biggest factor that will inhibit the recoverability of a shell buckling-dominated structure is the localization of strain during compression. A greater amount of strain localization during compression leads to locally failed regions that experience more cracking and an effective reduced recovery (Figure 34 B and F). When strains are more evenly distributed throughout the samples, there will be less local failure and a better global recovery after compression (Figure 34 D and H). The degree of strain localization can loosely be correlated with the slenderness ratio λ_h , as samples with more slender beams are more likely to have failure localize in the structure. Examples of the compression of different thin-walled hollow nanolattices from each of the four topologies tested with their corresponding φ_r can be found in Figure 34.

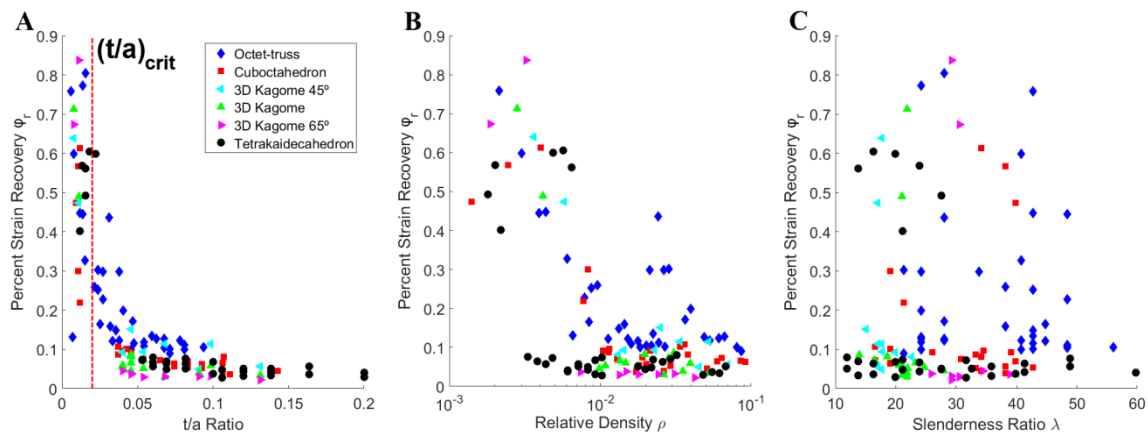


Figure 33: Recoverability of hollow Al_2O_3 nanolattice topologies.

A) Percent strain recovery φ_r versus the t/a ratio of the beams for all of the nanolattice topologies B) Percent strain recovery φ_r versus the relative density $\bar{\rho}$ plotted on a log scale for all of the nanolattice topologies. C) Percent strain recovery φ_r versus the slenderness ratio λ also for all of the nanolattice topologies.

As the t/a ratio becomes greater, samples are less likely to experience shell buckling, and if they do, the shells are more likely to experience local cracking in their post-buckled states, leading to less recovery. In samples with t/a well outside of the shell buckling-dominated failure regime, there is still some marginal observed recovery (Figure 33A). This arises because even in structures that are yielding-dominated there can be a small number of beams that undergo shell buckling. This marginal recovery manifests in the stress-strain data as a small non-linear region in the unloading region, as seen most pronounced in Figure 31B. A more in-depth discussion on the recovery of hollow Al_2O_3 samples can be found in Section 3.6.

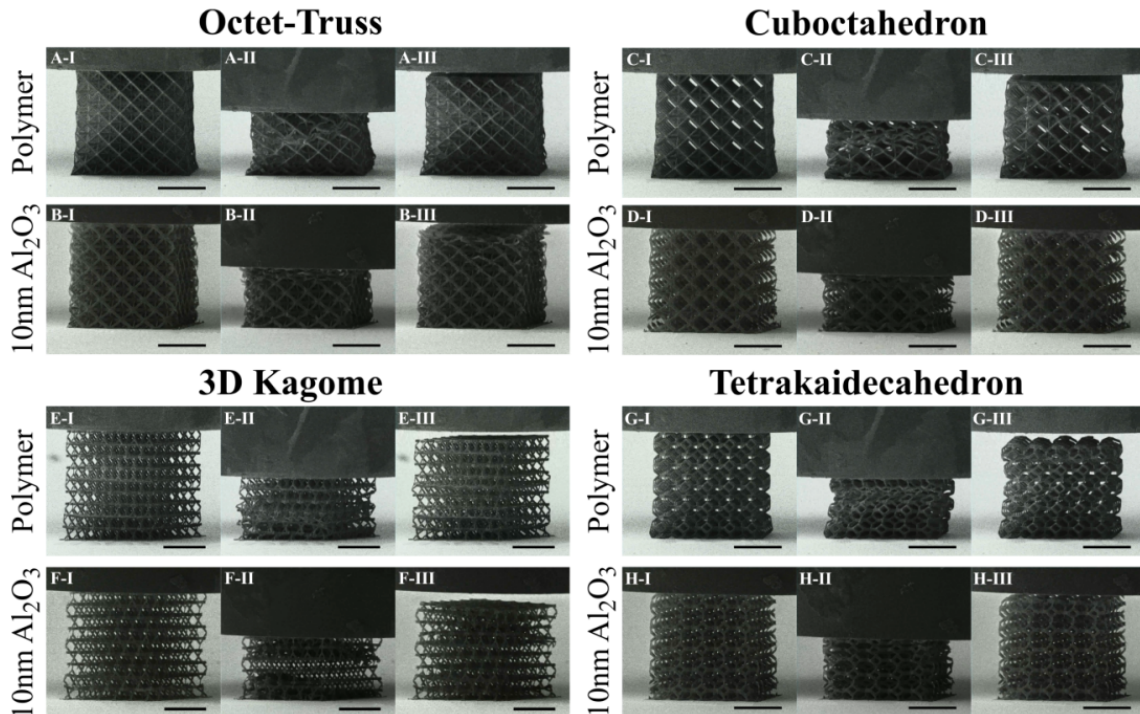


Figure 34: Compression of various polymer and thin-walled Al_2O_3 nanolattice topologies.

The figures above are still frames from videos of the compression of the four different nanolattice topologies and two material systems tested in this work. Each set of three images represents the uncompressed, fully compressed, and fully unloaded state. The structure and parameters are as follows: A1-AIII) polymer octet-truss, $10\mu\text{m}$ unit cell, $\phi_r = 83.8\%$; B1-BIII) Al_2O_3 octet-truss, $10\mu\text{m}$ unit cell, $\phi_r = 76.2\%$; C1-CIII) polymer cuboctahedron, $10\mu\text{m}$ unit cell, $\phi_r = 81.1\%$; D1-DIII) Al_2O_3 cuboctahedron, $10\mu\text{m}$ unit cell, $\phi_r = 91.3\%$; E1-EIII) polymer 3D Kagome, $4\mu\text{m}$ unit cell, $\phi_r = 78.7\%$; F1-FIII) Al_2O_3 3D Kagome, $4\mu\text{m}$ unit cell, $\phi_r = 68.1\%$; G1-GIII) polymer tetraikaidecahedron, $10\mu\text{m}$ unit cell, $\phi_r = 72.6\%$; H1-HIII) Al_2O_3 tetraikaidecahedron, $10\mu\text{m}$ unit cell, $\phi_r = 91.5\%$. All scale bars are $20\mu\text{m}$.

5.5. Strength and Stiffness Scaling with Relative Density

5.5.1. Strength and Stiffness of Rigid and Non-Rigid Topologies

As has been discussed in previous sections, the strength and stiffness of a cellular solid can be best characterized using the mechanical properties of the constituent material and the relative density of the sample. Here, stiffness and strength will scale with relative density as

$$E = BE_s\bar{\rho}^m \quad (52)$$

$$\sigma_y = C\sigma_{ys}\bar{\rho}^n \quad (53)$$

In these equations, E_s and σ_{ys} are the Young's modulus and yield strength of the constituent material respectively, B and C are proportionality constants, and n and m are scaling constants (74). In the analytic formulation of these equations for different topologies, structures are assumed to have slender, pin-jointed beams with relative densities scaling as $\bar{\rho} \propto (R/L)^2$. In structures that are rigid, it is assumed that the strength and stiffness are dominated by uniaxial compression and tension of beams (stretching-dominated). The strength and stiffness of a unit cell with beams in uniaxial compression will scale as $\sigma_y \propto (R/L)^2$ and $E \propto (R/L)^2$, which gives rise to a linear scaling of strength and stiffness with relative density ($m = n = 1$) and proportionality constants of $B = C = 0.3$ (78). In structures that are non-rigid, it is assumed that the strength and stiffness are dominated by bending of the beams (bending-dominated). The strength and stiffness of a unit cell with beams in bending will scale as $\sigma_y \propto (R/L)^3$ and $E \propto (R/L)^4$, which gives rise to scaling constants of $m = 2$ and $n = 3/2$ and proportionality constants of $B = C = 1$ (74).

The strength and stiffness scaling relationships of the nanolattices in this work across all topologies and material systems fail to match those that are predicted analytically for their

respective rigidities. An in-depth explanation for the measurement of the mechanical properties of polymer and Al_2O_3 nanolattices can be found in Appendix C. In the polymer samples, the stiffness scaling constants range between $m = 1.41$ (3D Kagome) and $m = 1.83$ (cuboctahedron), and the strength scaling constants range between $n = 1.63$ (tetrakaidecahedron) and $n = 1.92$ (cuboctahedron). In the hollow Al_2O_3 samples, the stiffness scaling constants range between $m = 1.46$ (3D Kagome) and $m = 1.73$ (tetrakaidecahedron), and the strength scaling constants range between $n = 1.45$ (3D Kagome) and $n = 1.77$ (tetrakaidecahedron). The scaling and proportionality constants for all the topologies and material systems tested in this work are shown in Table 2. Despite the small variations in the scaling constants for each of the topologies, the strength and stiffness data for each material system are observed to effectively collapse onto each other, as shown in Figure 35. This is due to the fact that for each larger or smaller scaling constant, there is a respective smaller or larger proportionality constant that counteracts it, effectively causing all of the strength and stiffness data to converge in the tested range of relative densities.

Material	Topology	<i>B</i>	<i>m</i>	<i>C</i>	<i>n</i>
Polymer	Octet-truss	0.815	1.77	1.313	1.88
	Cuboctahedron	1.092	1.83	1.588	1.92
	3D Kagome	0.427	1.41	0.973	1.68
	Tetrakaidecahedron	0.566	1.60	0.835	1.63
Al_2O_3	Octet-truss	0.387	1.63	1.139	1.71
	Cuboctahedron	0.519	1.69	0.823	1.64
	3D Kagome 45°	0.149	1.55	0.387	1.55
	3D Kagome	0.262	1.46	0.435	1.45
	3D Kagome 65°	1.797	1.65	3.039	1.77
	Tetrakaidecahedron	0.953	1.73	0.669	1.55

Table 2: Scaling and proportionality constants for different nanolattice topologies.

Scaling constants (m and n) and the proportionality constants (B and C) of the stiffness and strength scaling relationships respectively for each topology and each material system tested.

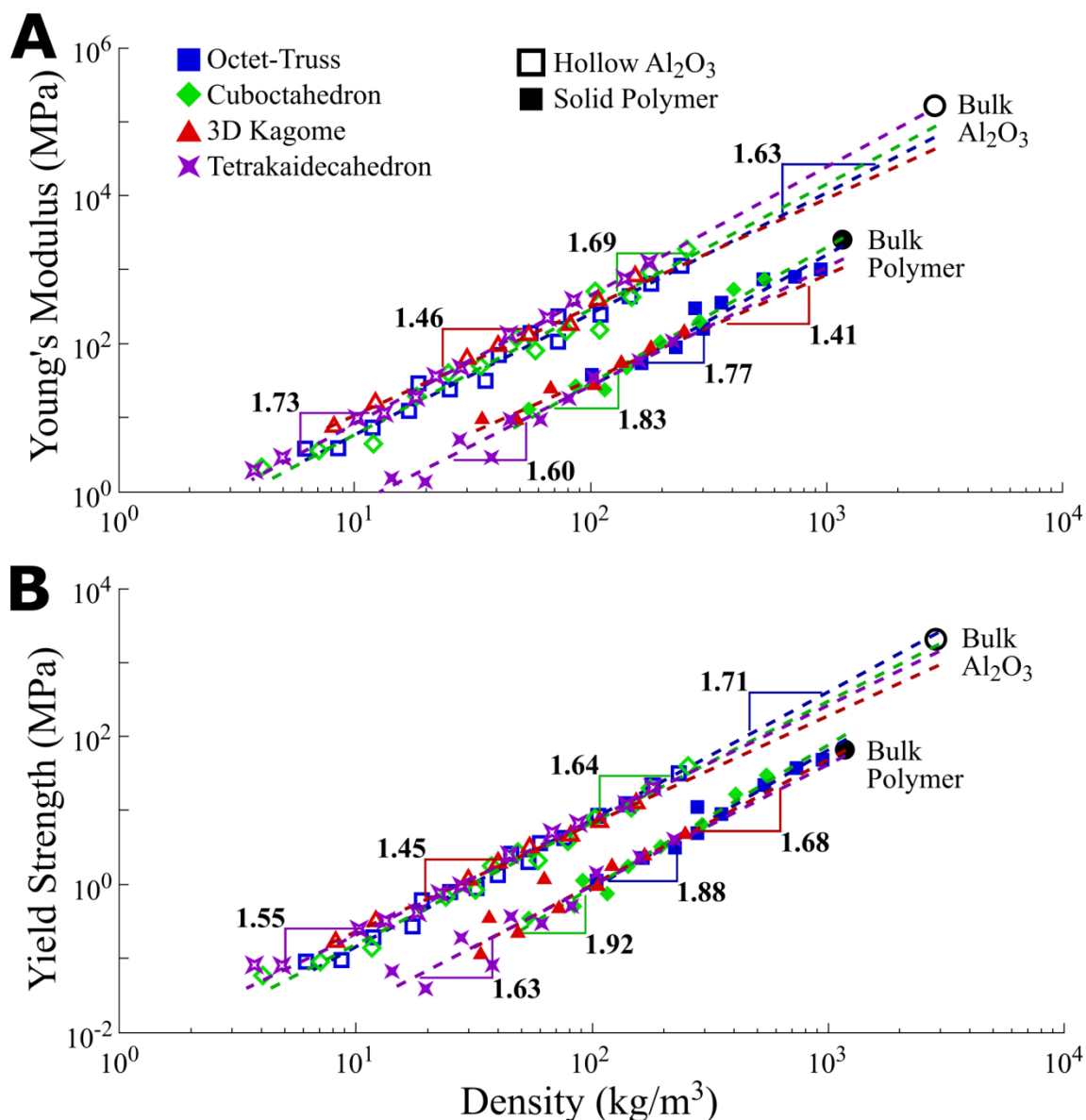


Figure 35: Strength and stiffness vs. density of different nanolattice topologies.

Logarithmic plots of A) the Young's modulus vs. relative density and B) yield strength vs relative density of every sample tested from all four regular topologies and both material systems. The values of the fully dense constituent materials are also plotted. Trend lines for each set of samples are meant to graphically illustrate the scaling relationships from Table 2.

From these results, it is apparent that in the range of relative densities tested for both material systems there is little to no correlation between the rigidity of the samples and the strength and stiffness scaling. The 3D Kagome and tetrakaidecahedron samples, which have the two lowest rigidities, also generally have lowest scaling coefficient values. In no case do the octet-truss samples, the only fully rigid topology, have the lowest scaling coefficient values.

None of the topologies approach a linear scaling with relative density for strength or stiffness, and none appear to approach the analytical scaling for a purely bending-dominated solid.

The convergence of the strength and stiffness data of the four regular topologies suggests that there are common underlying deformation and failure mechanisms in each of the structures. The mechanical properties of a lattice structure can be understood by characterizing the behavior of the constituent beams and nodes. In a structure with rigid (non-pin-jointed) nodes, all beams will be subject to a combination of bending and stretching, and the stiffness will scale as

$$E \propto C_1(R/L)^2 + C_2(R/L)^4 \quad (54)$$

Here, the first term is the contribution to stiffness from stretching and the second term is the contribution from bending. The contribution to stiffness from stretching and bending will depend on the slenderness in two ways. First, the slenderness of the beams will affect the node behavior; low slenderness beams will have nodes that act as a stiff elastic boundary, while slender beams will have nodes that act more like ideal pin-joints. Having less slender beams will also result in a larger volume contribution from the node, which will lead to an increased stiffness of the structure. Second, the magnitude of the beam slenderness will determine the relative contribution from the higher order terms; the stiffness of a structure with low slenderness beams will have a higher contribution from the quartic bending term, while for slender beams the quadratic term will dominate.

In order to determine the scaling relationship between stiffness and relative density, the relative density must first be fully defined. As is shown derived in Appendix B, for any lattice with circular beams, the relative density will scale as

$$\bar{\rho} \propto C_3(R/L)^2 + C_4(R/L)^3 \quad (55)$$

The stiffness follows a quartic scaling while the relative density follows a cubic scaling, showing that there is inherently a non-linear relationship between the two. For structures with less slender beams, the higher order terms will play a more dominant role (Figure 50A). Relating the stiffness and relative density using a power law relationship as $E \propto \bar{\rho}^n$ will result in a scaling constant between $1 \leq n \leq 2$. For a structure with more slender beams, the higher order terms of relative density can be ignored and the relationship will converge to the analytical relationships for stretching and bending dominated structures shown before.

All of the samples tested in this work have relatively low slenderness values, meaning they are likely in a regime where the traditional analytic linear scaling relationships break down. In collaboration with Greg Phlipot and Carlos Portela, fully meshed finite element (FE) simulations were run on octahedron samples with solid beams and a wide range of slenderness values (Figure 36). From these, it is shown that FE octahedra with low slenderness beams (high relative density) have stiffness values that closely match experimental results. These higher density FE samples also quantitatively reproduce the scaling relations found experimentally. For FE samples with highly slender beams (low relative density), there is a transition to a linear scaling between stiffness and relative density that matches well with analytic predictions for rigid topologies. This transition in scaling behavior arises because the features in highly slender samples qualitatively reproduce the assumptions that are made in the derivation of the analytical stiffness scaling relationships. This analysis was done for structures with solid beams, but a similar argument can be made for structures with hollow beams, with the stiffness and relative density proportionalities modified to account for their dependence on wall thickness.

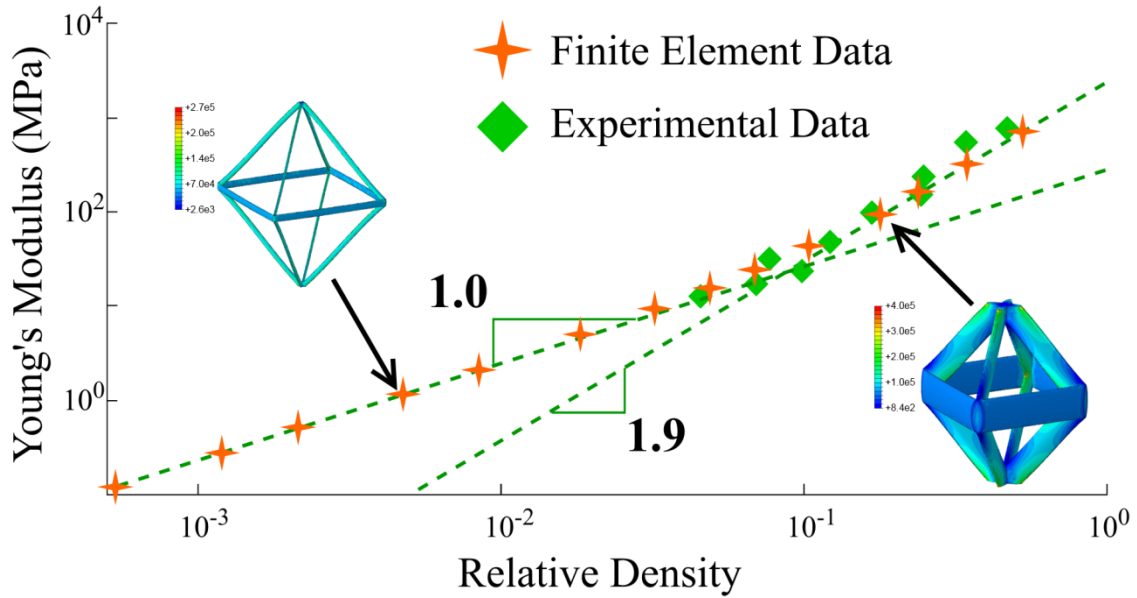


Figure 36: Stiffness of experimental data and FEM data for polymer octahedron nanolattices.

This figure shows the transition in stiffness-density scaling behavior from a linear relationship at low densities to a nearly quadratic scaling relationship at high densities.

The strength scaling with relative density can be explained in part using a similar proportionality analysis as was shown for the stiffness, but it will be influenced by additional factors like stress concentrations and buckling failure modes. The experimental scaling relationships between strength and relative density fall below what is analytically predicted for even a bending-dominated structure, suggesting that simply considering bending and stretching of the beams is inadequate. The strength of a buckling-dominated structure is known to scale with relative density as $\sigma_y \propto \bar{\rho}^{2.5}$ (109). As discussed in previous sections, beam buckling in the polymer structures is a dominant failure mode for many of the samples tested. While there was no indication that the strength scaling followed the analytical buckling-dominated relationship, the strength of the lower density samples was likely affected by it, and there may have simply been an insufficient range of relative densities tested to fully observe a manifestation of it.

The stress concentrations near the nodes of the samples are likely the major factor that affects the strength. All of the beams terminate at the nodes at a sharp angle, meaning there will

inherently be stress concentrations. For a beam in bending with a fixed boundary, the highest moment and corresponding highest stress will be at the fixed boundary, which in this case is the node, meaning there will be additional stress concentrations at the node from bending. In polymer samples, failure is often observed to initiate near the nodes, and in the hollow samples, nearly all of the deformation and failure occurs at or near the nodes. There is currently no work that fully investigates the effect of stress concentrations near nodes on the strength of lattice structures, and it is a subject that merits a much more in-depth analysis to fully understand. Regardless of the exact mechanism, the strong coalescence of the strength data across the range of relative densities tested suggests that there is common failure mechanism between the different topologies that governs the strength behavior.

There are many additional factors that will affect the exact strength and stiffness of a nanolattice. These include imperfections like waviness in the beams, misalignment at the nodes, improper measurement of the sample dimensions which leads to incorrect relative density calculations, variable effects of different wall thicknesses, and different material properties of the polymer given different laser exposures. Many of these factors require a much more in-depth analysis to fully quantify the effect of, and while there is no attempt to do so in this work, they are important factors to consider in the scope of the results shown here.

5.5.2. The Effect of Angle Changes on Strength and Stiffness

Three variants of hollow 3D Kagome lattices were tested to study the effect of changing the angles of the beams on the strength and stiffness scaling. These three had tetrahedron face-edge angles of 45° , 54.7° (regular tetrahedron), and 65° , and were designed with their respective compression or elongation axis in the z-direction. CAD models of the three unit cells can be shown in Figure 37A.

The strength and stiffness of a structure with varying beam angles has been studied both analytically and experimentally (7, 15, 110), and it has been found that for a structure with a beam angle of θ from the plane perpendicular to the compression axis, they will follow a scaling relationship of

$$E = BE_s \bar{\rho}^m \sin^4(\theta) \quad (56)$$

$$\sigma_y = C\sigma_{ys} \bar{\rho}^n \sin^2(\theta) \quad (57)$$

From these equations, there should be no deviation of the scaling behavior with changes in angle but instead only a change in the magnitude of the scaling data. The effect of the angle change should also be a more amplified in the stiffness data than the strength data. For the angle range tested here, these equations predict the 45° 3D Kagome samples will be 1.8 times more compliant and 1.3 times weaker than the regular samples, and the 65° samples should be 1.5 times stiffer and 1.2 times stronger than the regular samples.

These predictions are very well matched by the experimental results found here. There were some small variations between the scaling coefficients of the three topologies, but they generally followed the same scaling law behavior. The 65° samples were stiffer and stronger than the regular samples on average, and the 45° samples were weaker and more compliant on average. As seen in Figure 37, the increase or decrease in the stiffness data with angle changes was more pronounced than the change in strength. At very low densities, the 65° sample strength began to converge with that of the regular samples, but that may be due simply to an increased effect of imperfections. The scaling and proportionality constants for each of the 3D Kagome geometries can be found in Table 2, and a full list of the structural parameters and mechanical data can be found in Table 5.

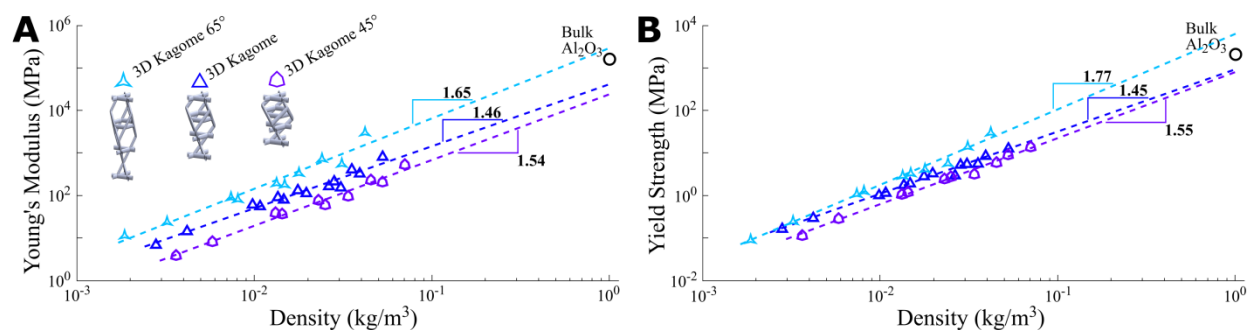


Figure 37: Strength and stiffness vs. density of 3D Kagome lattices with varying angle.

Logarithmic plots of A) the Young's modulus vs. relative density and B) yield strength vs relative density of all 3D Kagome samples tested in this work.

5.5.3. The Role of Imperfections – Missing Beams

To study the role of imperfections in nanolattices, polymer octet-truss samples were made with beams that were removed randomly from the structure (16.7%, 33.3%, and 50% removed), randomly only from the diagonal beams (25%, 50%, and 75% removed), and randomly only from the horizontal beams (50% and 100% removed). Examples of some of these are found in Figure 39A. All of the samples were made with an $8\mu\text{m}$ unit cell and with beams of slenderness $\lambda \approx 46$, meaning they are in a buckling-dominated failure regime. In an octet-truss structure, the horizontal beams make up 1/3 of the sample and diagonal beams make up 2/3, so removing 100% of the horizontal beams equates to removing 33.3% of the total beams in the structure. Equivalent percentages of different types of beams were removed from the sample to study their respective role in governing the mechanical properties. In the analytical formulation of an octet-truss structure, the strength and stiffness are governed by uniaxial tension and compression of the horizontal and diagonal beams respectively, and by systematically removing horizontal and diagonal beams it is possible to study their relative contribution to the mechanical properties.

As seen in Figure 38, a removal of any of the beams leads to a rapid decrease in both the strength and the stiffness of the structure, and the removal of identical percentages of different

types of beams elicits a very similar mechanical response. The full octet-truss sample (0% beams removed) is observed to undergo a single large buckling failure event. Periodically removing larger numbers of the beams results in a gradually smaller initial burst with either periodic buckling oscillations or a plateauing behavior afterward. Removing 50% of the beams in the structure results in the elimination of any bursting behavior, and the subsequent deformation is ductile-like with a plateau in the stress. Removing 50% of the beams in an octet-truss sample results in a structure with the same number of beams as a cuboctahedron; the mechanical properties of the missing beam samples are much lower than they would be in an equivalently dense cuboctahedron, which are observed to be similar to that of an octet-truss with the same slenderness of the beams (Figure 30). The absence of burst behavior in the octet-truss samples with 50% of the beams removed suggests that local bending is dominating the deformation and precluding the occurrence of buckling. This likely occurs due to poor load transfer in the missing beam samples caused by the stochastic nature of the structure.

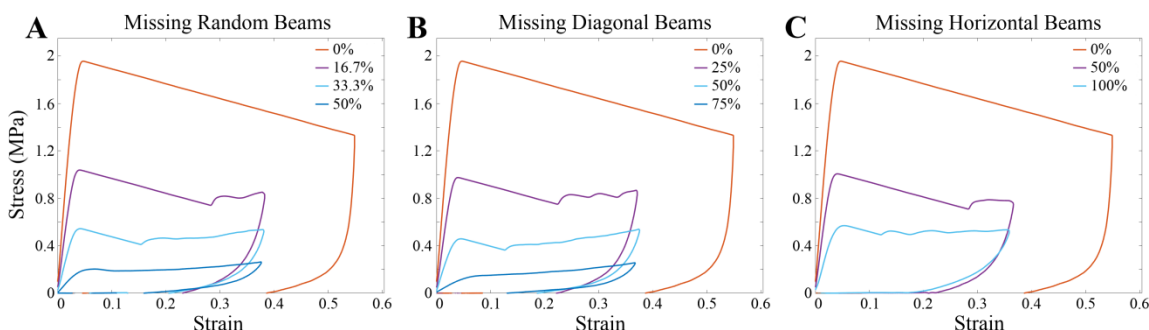


Figure 38: Stress-strain data of polymer octet-trusses with missing beams

Stress-strain plots of the three classes of octet-truss structures with missing beams. A) Randomly missing, B) missing diagonal beams and C) missing horizontal beams.

Plotting the strength and modulus against the relative density of each of the missing beam samples reveals the relative influence of the horizontal and diagonal beams on the mechanical performance. As can be seen in Figure 39, for samples with a high percentage of removed beams, removing the diagonally oriented beams has a more significant effect on the mechanical

properties, but for low percentages of beams removed, the relative influence of removing beams from diagonal or horizontal regions is much less significant. Diagonal beams are more closely aligned with the compression axis and are responsible for the load transfer to horizontal beams. The octet-truss structure is highly redundant, so when only a few beams are removed there are still enough diagonal beams to effectively transfer the load. When a large percentage of the diagonal beams are removed, there is poor load transfer vertically in the structure and bending begins to dominate the deformation. This also suggests that structures with less redundancy, like the tetrakaidecahedron, would be much more sensitive to missing beam imperfections.

The strength and stiffness scaling trends with relative density for the missing beam samples range between $n = 3.0 - 3.8$ for the strength scaling and $m = 3.1 - 4.3$ for the stiffness scaling, meaning the mechanical performance of structures with randomly removed bars degrades much more quickly than that of periodic structures. This also supports the argument that beams in the samples are underutilized due to the stochastic nature of the structure. A full list of the structures tested and their mechanical properties can be found in Table 8.

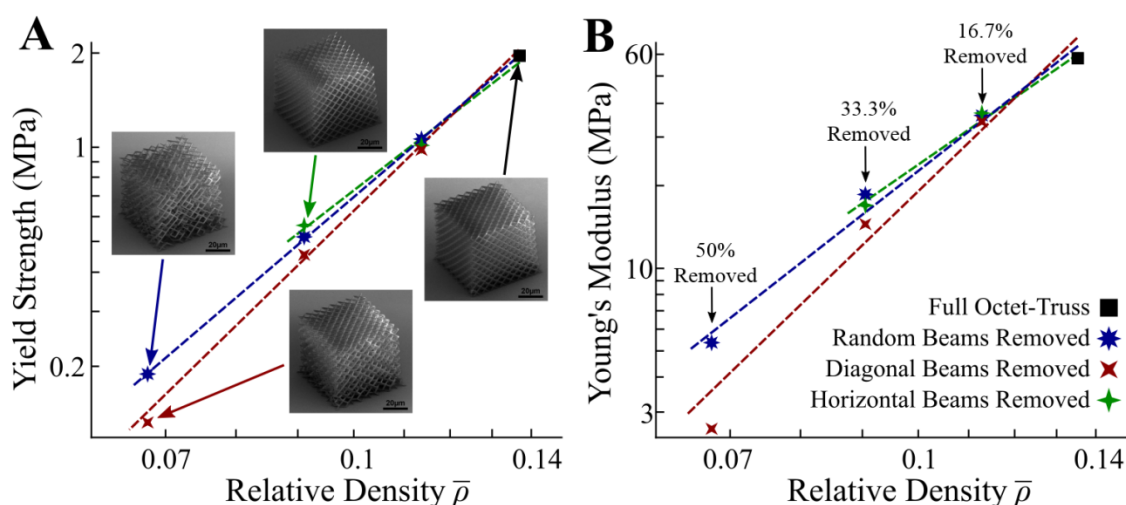


Figure 39: Strength and modulus of polymer octet-trusses with missing beams

A) Yield strength vs. relative density and B) Young's modulus vs. relative density of polymer octet-truss samples with beams that have been randomly removed from the entire structure, only the diagonal beams, and only the horizontal beams. Trend lines are fit to show the scaling behavior.

5.5.4. The Role of Imperfections – Offset Nodes

To further study the role of imperfections in nanolattices, polymer octet-truss samples were made with randomly offset nodes. The magnitude of the offset was controlled by a uniform random distribution between 0 and a prescribed maximum; the prescribed maximum offsets were made in 0.5 μm increments from 0 to 4 μm . Examples of these are shown in Figure 41A. The direction of the offsets were made to be random in all except the topmost and bottommost nodes of the samples, which were only allowed to displace in the x and y directions to mitigate the effect of misalignments with the indenter tip during compression. Samples were made with an 8 μm unit cell the same beam dimension as in the missing node samples. The exact slenderness of the beams will vary in the samples because the offset of the nodes results in variable beam lengths, but the average slenderness in each sample will remain comparable. The connectivity and relative density are effectively identical across different offset node samples. While there have been no analytic formulations on the role of offset node imperfections on 3D octet-truss structures, modeling has been done previously and predicted little to no change in the stiffness and a sigmoid decrease before a plateau in the strength (12).

As seen in Figure 40, increasing the degree of the offset in the samples results in a gradual decrease in the yield strength but causes no significant deviation in the stiffness. The lower offset samples fail via a single large buckling event that manifests as a strain burst. As the degree of offset increases, the magnitude of the initial burst event decreases and samples experience additional smaller buckling events with some post-burst densification. If samples were made with larger degrees of offset nodes the burst behavior may gradually be eliminated, but the maximum offset in the samples tested here is $\sim 71\%$ of the beam length, so increasing the

offset further may result in a change in the topology from an unforeseen intersection of beams or an elimination of some beams entirely due to intersecting nodes.

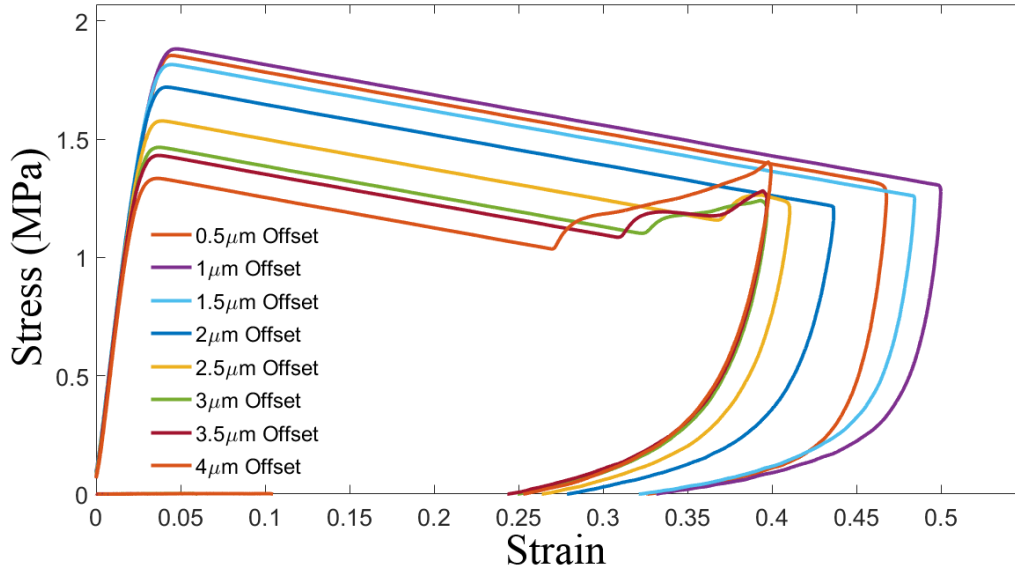


Figure 40: Stress-strain data of offset-node octet-trusses.

Representative stress vs. strain plots of polymer octet-trusses with varying degrees of nodal offsets.

Plotting the yield strength and Young's modulus against the relative offset (max offset/beam length), it is more apparent that the modulus is almost entirely unaffected by the offset, and the variations in stiffnesses are statistically insignificant. The strength experiences a sigmoidal decrease, with initially very little change then a more significant decrease and finally a slight plateau toward higher offsets. The strength of the sample with the largest maximum offset is $\sim 22\%$ lower than the strength of the sample with the least amount of offset. Stiffness is a purely elastic property; from these results it is apparent that it is primarily affected by the topology, connectivity, and relative density of the samples and it is relatively insensitive to nodal offset imperfections. The stiffness of a lattice structure is governed primarily by beam bending, compression, and tension, and the average contribution from each of these isn't as affected by changes in nodal positions. The strength is more sensitive to stress concentrations and will be reduced if even a small number of beams in the sample are subject to higher stresses from

additional bending. Failure is also observed to localize to whole layers in samples that are buckling-dominated, so if local beams have higher slendernesses it may result in the earlier initiation of buckling, thereby reducing the strength of the whole sample.

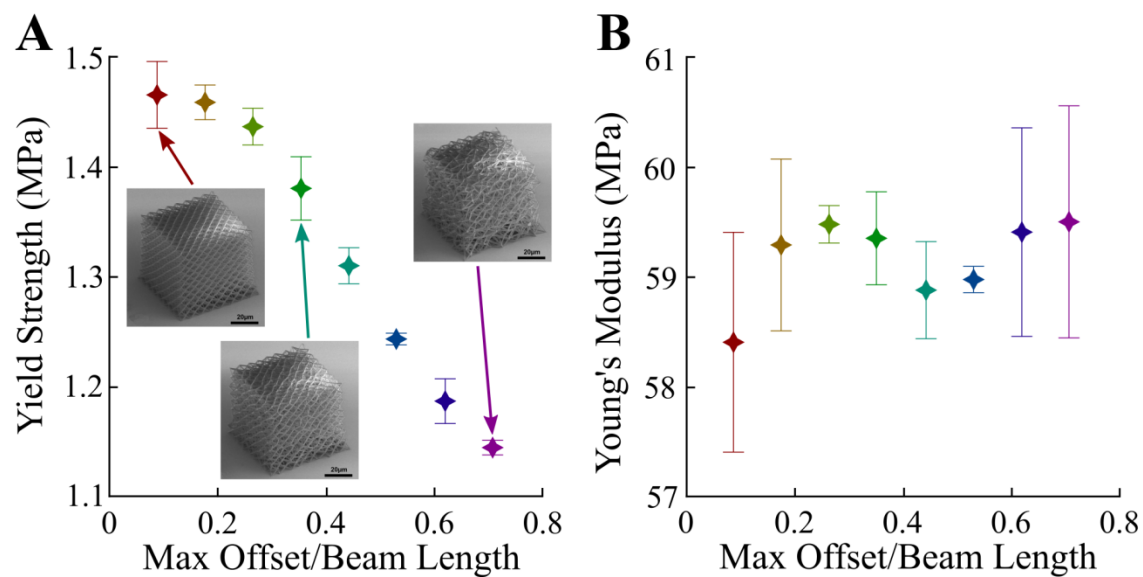


Figure 41: Strength and modulus of offset-node polymer octet-trusses.

A) Yield strength vs. relative nodal offset and B) Young's modulus vs. relative nodal offset of polymer octet-truss samples with offset nodes.

Chapter 6: Summary and Outlook

This dissertation is a review of some of the progress that has been made in the creation of new materials developed through the integration of nanomaterials into 3D nanoarchitectures. It has been shown here that it is possible to reliably incorporate high strength nanomaterials into a 3D architected material with features as small as 5nm. This is primarily accomplished through the use of two-photon lithography, which is used to create polymer 3D truss scaffolds with micro- and nanoscale features, in combination with atomic layer deposition (ALD), which allows for a conformal thin-film deposition of ceramics like titanium nitride and aluminum oxide. Ceramics experience size-affected strengthening due to a statistical reduction in the number of intrinsic flaws when their thickness is reduced; the nanoscale ceramics used in this work are sufficiently small that their strengths approach the theoretical limits of material strength.

The combination of high strength nanomaterials and architecture allows for the exploitation of mechanical phenomena that give rise to novel material properties. Here, shell buckling in hollow thin walled ceramic tubes is used to create ductile and recoverable ceramic metamaterials. In a bulk ceramic, the low relative strength to modulus ratio makes it prohibitively difficult to make thin-walled hollow tube lattices that are able to have shell buckling as a dominant failure mechanism. By using nanoscale ceramics with enhanced strength, it becomes possible to utilize shell buckling as a reliable design feature. Shell buckling is observed throughout the course of this work in numerous nanolattice topologies, and it is consistently used to bring about ductile-like behavior and recoverability in what would otherwise be an intrinsically brittle material.

The fabrication techniques employed here allowed for the design and creation of structures with arbitrary geometries, enabling the study of many previously unexplored architectures. In the course of this work, hierarchical nanolattices were designed and fabricated for the first time. They were demonstrated to have enhanced recoverability and a near linear scaling of strength and stiffness with relative density, all despite not having any optimization in their design. Four types of periodic lattices with varying degrees of rigidity were also studied, and their strength and stiffness were found to be nearly identical when normalized across relative densities, showing a marked deviation from their predicted strength and stiffness scaling with relative density. This suggests a need to reevaluate currently existing scaling relationships for cellular solids and reconsider new architectures that may engender enhanced mechanical property relationships.

I believe the work presented here demonstrates the incredible potential of nanoarchitectures to make new materials with unprecedented mechanical properties. There is now the capability to reliably create three-dimensional architectures with features well into the nanosized regime. There are two major obstacles that nanoarchitected materials currently face: the ability to create them on large scale (i.e. the ability to scale them up), and the ability to efficiently optimize their mechanical properties. To the first point, without the ability to scale up fabrication, nanoarchitected materials will likely be relegated to niche engineering applications. These “niche” applications may be far reaching, especially as the technological world continues to miniaturize, but unless large scale samples can be made, many of the new material properties discovered here and elsewhere may simply remain laboratory novelties. To the second point, there is a demonstrable gap in our knowledge of both nanomaterials and architecture that must be overcome in order to efficiently design new nanoarchitected materials. There is and has been a

large body of effort toward understanding the mechanics of nanomaterials, but this must now be extended to study the mechanics of nanomaterials with complex architecture. Topology optimization techniques exist and have been shown to be incredibly useful and versatile, but new computational techniques must be developed that accurately capture the complexity of nanoarchitected systems while remaining computationally efficient. I hope the work presented here proves to be a useful foundation for the further design and fabrication of nanoarchitected materials, but there is much progress to be made before the large scale utilization of nanoarchitected materials in real world engineering applications.

Appendices

Appendix A. Nanolattice Design Methodologies

Periodic Lattice Design

A majority of the samples fabricated in this work were periodic lattices; these are lattices that can be characterized by a single repeating unit cell that has been patterned in space. A range of different unit cells have been designed and fabricated in this work, some of which are shown in Figure 42 below. A majority of these unit cells were designed as cubic unit cells for simplicity of patterning, but some, like the 3D Kagome lattice, were designed with hexagonal symmetry.

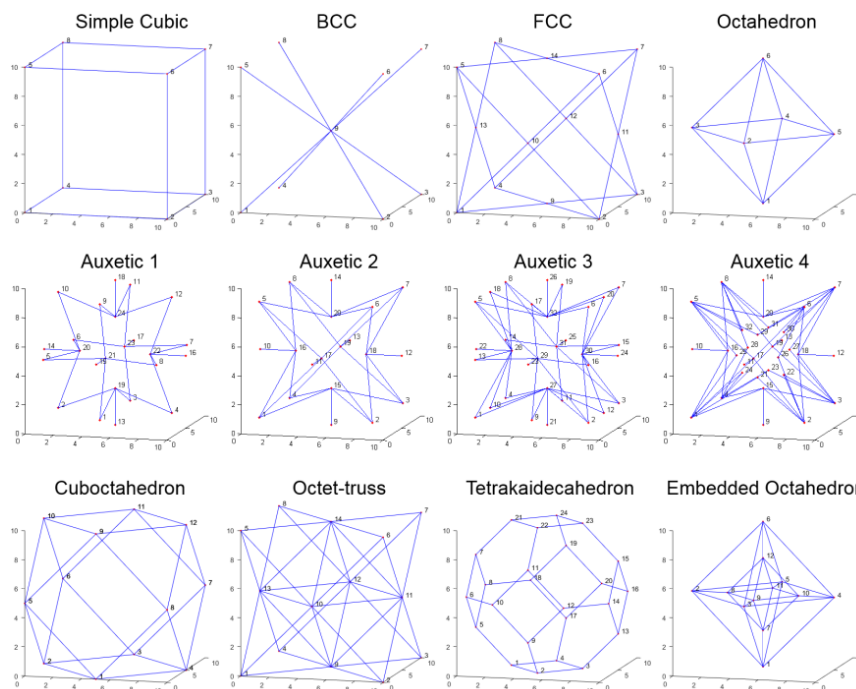


Figure 42: Single Unit Cell Designs.

The figures above are examples of unit cells with cubic symmetry that can easily be tessellated in 3D.

The fabrication capabilities provided by the Nanoscribe system used in this work allow for arbitrary writing in three-dimensions and are not limited to the layer-by-layer fabrication that most 3D printing systems are. As such, periodic lattices created with this system can be fabricated in a number of ways. The simplest fabrication method is to take single unit cells and

pattern them one at a time in their symmetry directions. This is a slow and inefficient fabrication method, but it is very versatile because any unit cell can easily be substituted in. If a unit cell has a beam that lies on its outermost face, it will be double written using this fabrication scheme, but it is possible to write a method that finds and eliminates double written beams. This fabrication scheme is shown in Figure 43 below.

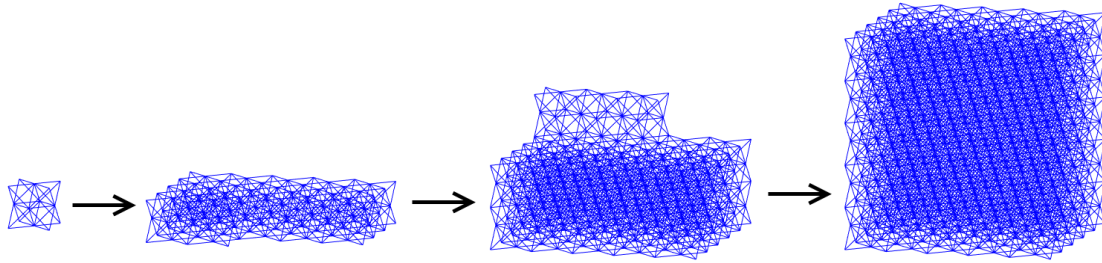


Figure 43: Periodic Lattice Fabrication - Tessellation.

This figure shows the design scheme for creating an octet-truss periodic lattice by tessellating a single unit cell.

A more efficient but more individualized design scheme is a “layer-by-layer” type fabrication. In this, beams that are connected in a straight line are written as one continuous element and the structure is gradually built up in layers starting at the bottom. This fabrication scheme eliminates the inefficiencies in the fabrication of tessellating a single unit cell because fewer pauses are made between writing individual beam segments. It also automatically eliminates redundant beam elements. The downside is that the method is not conducive to substituting a different base unit cell and each lattice generally must be individually designed. An example of this fabrication process can be seen in Figure 44 below.

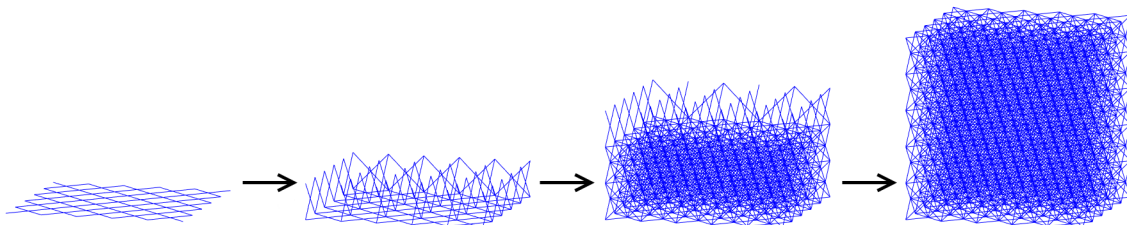


Figure 44: Periodic Lattice Fabrication – “Layer-by-Layer”.

This figure shows the design scheme for creating an octet-truss periodic lattice by writing connected beams as a single element and writing an entire layer of sample at once.

Hierarchical Lattice Design

A hierarchical lattice is defined here to be one that is composed of beams that have a lattice substructure, i.e. a hierarchical lattice is one with beams made of beams. The hierarchical order of a lattice is defined as the number of distinct structural length scales that it contains; as an example, a regular periodic lattice is a 1st order structure, a lattice made of lattices is 2nd order, a lattice made of lattices made of lattices is 3rd order, etc. Defining hierarchical lattices under this schema allows for the creation of lattices of arbitrary order and therefore arbitrary complexity. As a means of limiting the number of potential designs, hierarchical lattices in this work are created using repeating unit cells with cubic symmetry.

The hierarchical nanolattices fabricated in this work are designed using a recursive method, meaning their final structure is dependent on the structure that is defined in each previous step, effectively allowing the structure to have infinite dimensionality. The design scheme for a hierarchical lattice takes place in the following steps: (1) an array of unit cells are defined; (2) the first unit cell in the array is designated the primary structure; (3) the second unit cell in the array is designated the secondary structure and is patterned N times along the length of the primary structure; (4) the resulting hierarchical unit cell is designated the new primary structure and the third unit cell in the array is patterned N times along the length of it; (5) this process is repeated until the designated order of hierarchy is reached. If the hierarchical order of the lattice is greater than the number of unit cells in an array, the array will be looped through. Secondary unit cells that are patterned along the beams of the primary structure are placed one at a time; an illustration of the fabrication of an octahedron-of-octahedra is shown in Figure 45A. To ensure the rigidity of the constituent hierarchical beams, reinforcing beams are often added

after the tessellation of the secondary unit cell, examples of which are shown in Figure 45 B and C below.

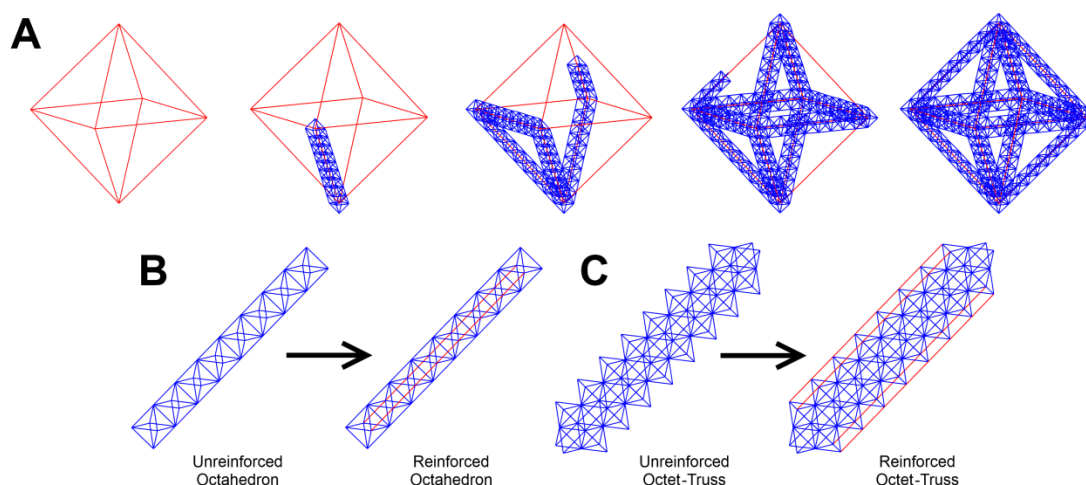


Figure 45: Hierarchical nanolattice design process.

A) Construction of an octahedron-of-octahedra unit cell. B) Example of unreinforced vs. reinforced octahedron fractal beam. C) Example of unreinforced vs. reinforced octet-truss fractal beam.

This design scheme is sufficiently general to create a wide range of hierarchical unit cells with varying topology, slenderness, and hierarchical order. Examples of a range of example unit cells fabricated are shown in Figure 46. Once hierarchical unit cells have been created, they can be tessellated in 3D in the same manner described for the periodic lattices to create a hierarchical lattice structure.

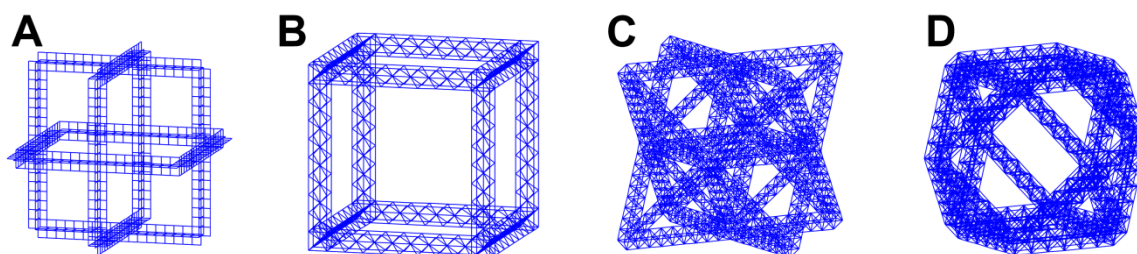


Figure 46: Hierarchical nanolattice unit cells.

Example geometries of: A) a cage of crosses, B) a cube of reinforced-BCC unit cells, C) an octet-truss of octahedra, and D) a cuboctahedron of embedded-octahedra.

Layer-by-Layer Design

Another fabrication method developed in the course of this work is layer-by-layer writing. In this, a lattice structure is defined and its beams are sliced for writing in a layer-by-

layer fashion. Once a lattice structure has been created, a series of x-y planes are defined at evenly spaced intervals along the z-axis. Individual beams are checked for whether they intersect with a given plane; if they are found to intersect, the angle that they intersect at is determined. A circular beam with diameter R that intersects a plane at angle θ will have an elliptical cross section with semi-minor axis R and semi-major axis $R/\sin(\theta)$. Once the intersections have been determined, an elliptical profile is written for each beam centered at the intersection point of the beam with the plane. The elliptical profiles are then filled (hatched) with horizontal lines. Any beams that are found to lie in the x-y plane and are within a certain distance of the given slicing plane are taken, their beam width at that particular height is calculated, and a series of horizontal lines is written to fill them. This x-y plane slicing is repeated until the maximum height of the sample is reached. An example of this process for a single octet-truss unit cell is shown in Figure 47 below.

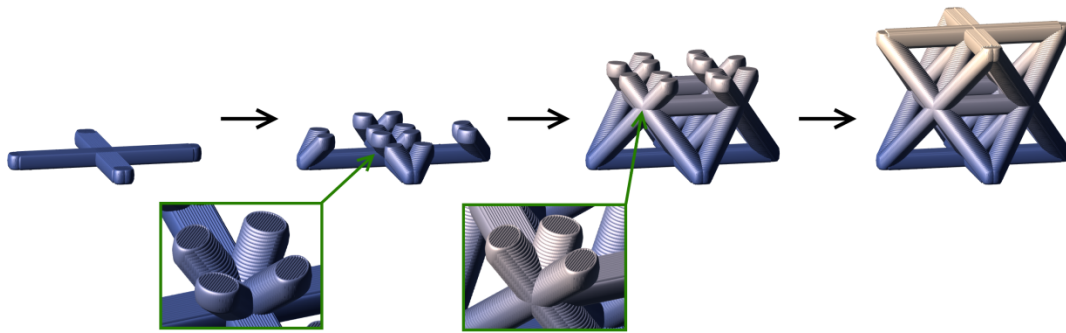


Figure 47: Layer-by-layer Nanolattice Fabrication.

Still images showing the layer-by-layer fabrication of an octet-truss unit cell with circular beams.

One major consideration that must be made when writing with two-photon lithography is that the constituent building block of the samples is an elliptical voxel. Writing a perfect circular beam with an elliptical voxel is effectively impossible, but methods can be taken to ensure that the resulting beam is more circular than it would have been otherwise. In order to write a circular beam of radius R with a circular voxel of radius r , a circle must be written with radius $R - r$. In

order to write a circular beam of radius R at an angle θ with respect to the horizontal plane using a vertically oriented elliptical voxel with semi-major and semi-minor axes of a and b , an ellipse must be written with semi-major and semi-minor axes $R - b$ and $(R - c)/\sin(\theta)$ respectively, where here c is the angle corrected height of the ellipse, which can be shown to be $c = \sqrt{a^2 \cos^2(\theta) + b^2 \sin^2(\theta)}$. An example of this concept is shown in Figure 48. Regardless of the exact correction, an elliptical beam patterned to approximate a circle will always have some overshoot; as the aspect ratio of the ellipse increases and the height approaches the radius of the circle, the beam will get progressively more rectangular.

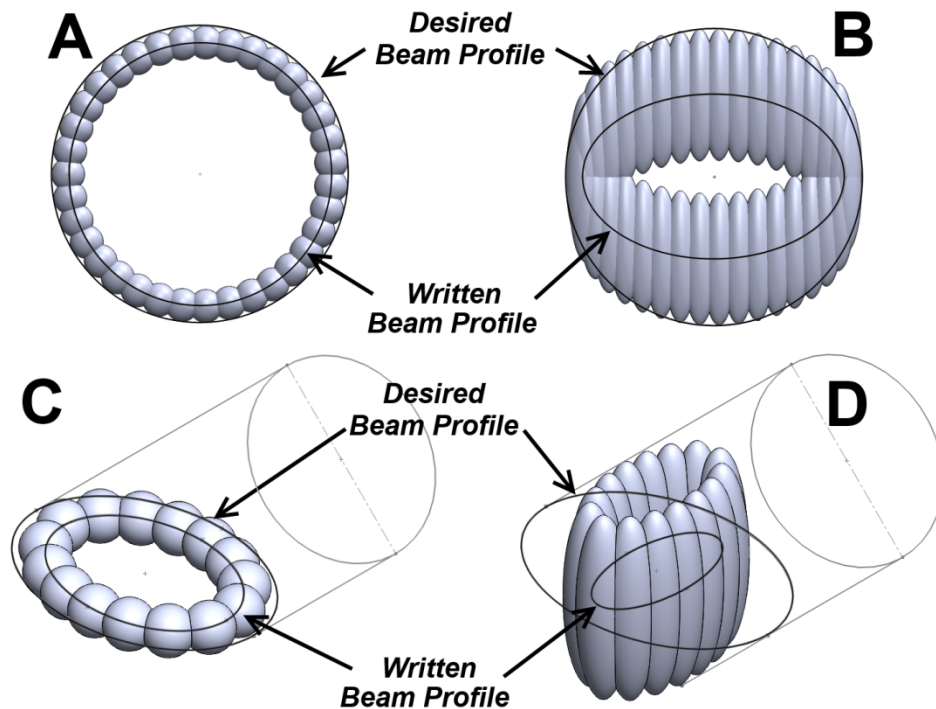


Figure 48: Writing Circular Beams with Elliptical Voxels.

A) Writing a circular horizontal beam with a spherical voxel vs. B) a circular horizontal beam with an elliptical voxel. C) Writing a circular diagonal beam with a circular voxel vs. D) a circular diagonal beam with an elliptical voxel.

Appendix B. Analytic Calculation of Relative Density

It is possible to derive an analytical expression for the relative density of a circular beam lattice. If we assume there are N beams with radius R and length L that form a cubic unit cell with width W , the relative density can be estimated to be

$$\bar{\rho} = \frac{N\pi R^2 L}{W^3} \quad (58)$$

For small tube radius to length (R/L) ratios this equation is approximately correct, but as the R/L increases the nodal interference has a greater effect on the relative density and the equation will be inaccurate. The interference area between circular tubes at a node is a cylindrical wedge (Figure 49), the volume of which can be found to be $V = \frac{2}{3}hR^2$. For two beams that intersect at an angle θ , the height of the cylindrical wedge is $h = R \cot(\theta/2)$. While it would be possible to sum all the cylindrical wedge interferences between beams, there are additional wedge-wedge interferences that are difficult to account for. However, all these interferences scale as R^3 , so a corrected version of relative density can be expressed as

$$\bar{\rho} = \frac{N\pi R^2 L - CR^3}{W^3} \quad (59)$$

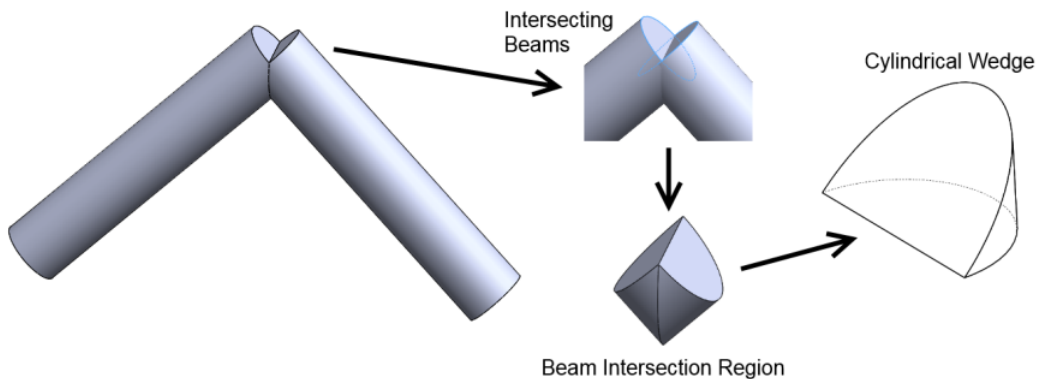


Figure 49: Beam Nodal Interference

Illustration showing the interference of two cylindrical beams forms a cylindrical wedge.

Here, C is a constant that accounts for the sum of all the nodal interferences. For hollow structures, there are additional factors that must be included. The correction for hollow cylinders and spheres with a wall thickness t , respectively, are $f\left(\frac{t}{R}\right) = 2\left(\frac{t}{R}\right) - \left(\frac{t}{R}\right)^2$, and $g\left(\frac{t}{R}\right) = 3\left(\frac{t}{R}\right) - 3\left(\frac{t}{R}\right)^2 - \left(\frac{t}{R}\right)^3$. If we include these in the relative density, we get the modified equation.

$$\bar{\rho}_h = \frac{N\pi R^2 L f\left(\frac{t}{R}\right) - CR^3 g\left(\frac{t}{R}\right)}{W^3} \quad (60)$$

We will now look at an example unit cell with an inscribed octahedron (Figure 50A). There are 12 beams in the structure at 6 identical nodes with beams that meet at 60° and 90° angles with respect to each other. The unit cell is cubic, and we can take it to have width L . All the beams therefore have a length $L/\sqrt{2}$. We can define the relative density to be

$$\bar{\rho} = \frac{12\pi R^2 \left(\frac{L}{\sqrt{2}}\right) - CR^3}{L^3} \quad (61)$$

Here, $C \cong 61.82$, which accounts for the intersections at the 6 corners, the two types of angles, and the number of intersections at each corner. We can also define the density of the hollow structure (Figure 50B) to be

$$\bar{\rho}_h = \frac{12\pi R^2 \left(\frac{L}{\sqrt{2}}\right) f\left(\frac{t}{R}\right) - CR^3 g\left(\frac{t}{R}\right)}{L^3} \quad (62)$$

This is a cubic equation, and by taking a derivative we can find a critical radius where the relative density is at a maximum. This occurs at

$$R_c = \frac{4\sqrt{2}\pi L + Ct}{2C} \quad (63)$$

The maximum possible radius of the structure before multiple beams begin to overlap is $R_{max} = L/2\sqrt{6}$, so this critical radius may be outside of the possible range of relative densities ($t < R < L/2\sqrt{6}$).

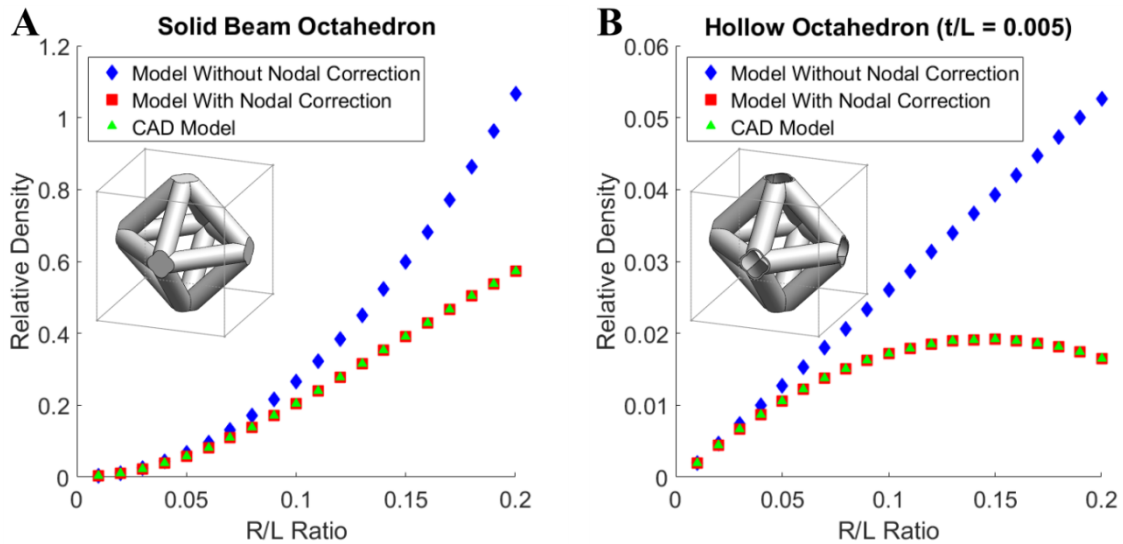


Figure 50: Octahedron Unit Cell Relative Density

Analytical models for the relative density of an octahedron unit cell. A) shows the relative density for a unit cell with solid beams, and B) shows the relative density for a unit cell with hollow beams both with and without corrections for nodal interferences.

Appendix C. Data Analysis Methods

The data obtained from nanolattice compression experiments performed in this work has a wide range of stress-strain responses, and as such, it is necessary to formulate a consistent method to measure meaningful Young's modulus (E) and yield strength (σ_y) data. In every sample tested, the stress-strain data was comprised of a toe region, a linear region, and a failure region. The toe region is a non-linear segment of data at the beginning of loading, and in this work it generally corresponds to slight misalignments and imperfections between the sample and the indenter axis. For each sample, a subset of stress-strain data was taken starting at the beginning of loading and going to the onset of failure (shown in blue in Figure 51). The maximum slope of this data subset is measured and taken to be the Young's modulus E . This is done to mitigate the effect of the toe region on the stiffness measurement. In polymer samples, or any sample with ductile yielding, a line with slope E is taken with a 0.02% strain offset from the obtained Young's modulus fit, and the intersection of this line and the stress-strain data is taken to be the yield strength σ_y (Figure 51A). In hollow Al_2O_3 samples, or any sample with a brittle yielding, the yield strength is taken to be the peak stress before failure (Figure 51B).

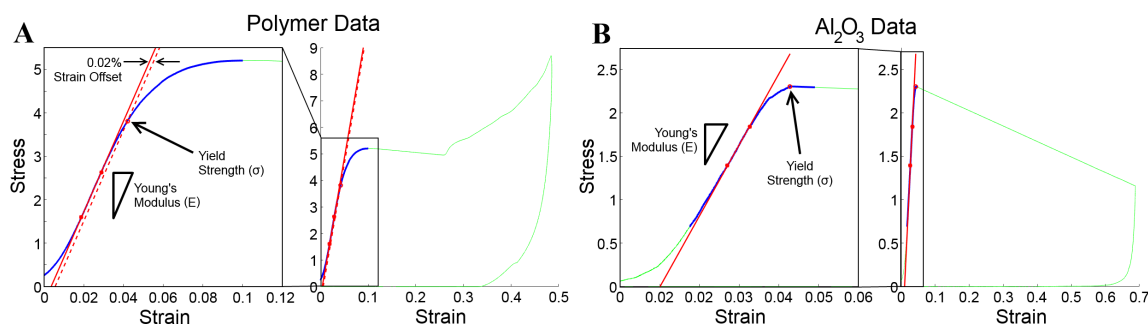


Figure 51: Yield Strength and Young's Modulus Measurement.

The Young's modulus and yield strength measurement for A) a polymer nanolattice and B) a hollow Al_2O_3 nanolattice.

The biggest factor that impacts the reliability stress-strain data is the compliance of the indenter loading spring. Most nanoindenters are designed to operate in a small displacement

region where the loading spring compliance is linear and can easily be subtracted. In this work, samples were tested to large displacements, which, in samples with a low peak load, resulted in a noticeable non-linear contribution to the stress from the loading spring compliance. This spring compliance had to be corrected in order to properly analyze the data. The samples that were most affected by indenter spring compliances were those tested in-situ with the InSEM (SEMentor) system, which has a much smaller travel range than the G200 nanoindenter. In order to correct for the spring compliance, a curve was fit to the unloading region of the sample after the indenter had lost contact and this fit was subtracted from the original stress data. The exact type of fit depended on the displacement range that was tested, but it was generally between a quadratic and a cubic fit. To determine the correct fit, different weights of quadratic and cubic fits were made to the unloading data until the corrected stress-strain data looked reasonable. While this does mean that the magnitude of the stress at the largest displacement values may be inaccurate, the Young's modulus and yield strength are unlikely to be significantly affected, and the stress-strain behavior after the onset of failure is only studied qualitatively to understand the response of the sample.

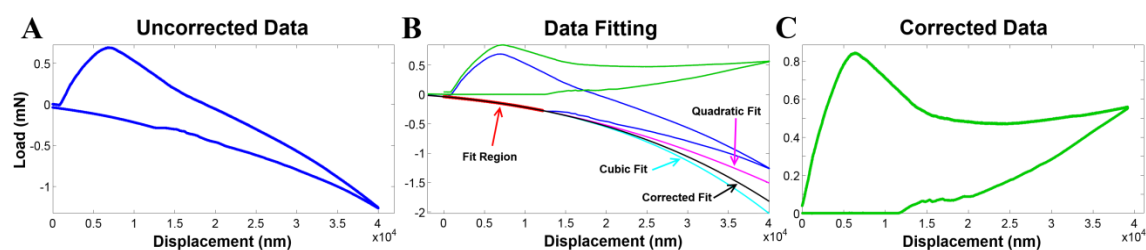


Figure 52: Spring Correction for a Highly Compliant Sample

A) The uncorrected stress-strain data from a nanolattice compression experiment. B) Plot showing different fits to the unloading data. C) The corrected stress-strain data.

Appendix D. Slenderness Ratio Formulations

The slenderness ratio of a beam is the most important dimensionless geometric parameter in determining mechanical performance. It can be defined as

$$\lambda = \sqrt{\frac{AL^2}{I}} \quad (64)$$

Here, A is the cross sectional area, L is the length, and I is the area moment of inertia of a beam. In a beam with a non-circular cross-section, there can be multiple area moments of inertia, leading to multiple slenderness ratios. In this work, due to the elliptical cross section of the 1st order beams and non-uniform cross section of the higher order beams, we will calculate the slenderness in the x and y-directions and take the maximum of those two slenderness ratios to be the slenderness of the beam.

There are multiple hierarchical orders of beams in each sample, and there are a corresponding number of slenderness ratios. The slenderness ratios for each beam have a subscript denoting their order: λ_1 is a 1st order slenderness, λ_2 is a 2nd order slenderness, and λ_n is an nth order slenderness. For higher order beams, there is a non-uniform cross sectional area and area moment of inertia. A majority of the load is carried by the 1st order beams that are oriented along the axis of the 2nd order beam (Figure 26), so for simplification, those will be the only ones used in the area and area moment of inertia calculations.

The area moment of inertia of a beam with moment of inertia I_0 and area A that has a center of gravity a distance r away from the principal axis of rotation can be found to be $I = I_0 + Ar^2$. For the hierarchical beams in this work, there are multiple beams whose center of

gravity is not at the principal axis of rotation. The area moment of inertia of these beams can be calculated to be

$$I = \sum_{k=1}^b I_k + A_k r_k^2 \quad (65)$$

The calculations for 1st, 2nd, and 3rd order solid and hollow beams are shown below.

1st Order Beam

In the samples fabricated in this work, the characteristic length dimension is the size of a unit cell L . For octahedron and octet unit cells, the beam length can be found to be $L_1 = L/\sqrt{2}$. For an elliptical beam with major axis a and minor axis b (Figure 53A), the area and area moments of inertia can be found to be

$$A_1 = \pi ab \quad (66)$$

$$I_{1x} = \frac{\pi}{4} a^3 b \quad (67)$$

$$I_{1y} = \frac{\pi}{4} a^3 b \quad (68)$$

From here, the slenderness ratios can be calculated to be

$$\lambda_{1x} = \frac{L\sqrt{2}}{a} \quad (69)$$

$$\lambda_{1y} = \frac{L\sqrt{2}}{b} \quad (70)$$

For a hollow beam with a wall thickness t (Figure 53B), the area and area moment of inertia to a first order approximation with wall thickness can be found to be

$$A_{1h} = \pi t(a + b) \quad (71)$$

$$I_{1xh} = \frac{\pi}{4} a^2 t(a + 3b) \quad (72)$$

$$I_{1yh} = \frac{\pi}{4} b^2 t (3a + b) \quad (73)$$

From here, the slenderness ratios can be calculated to be

$$\lambda_{1xh} = \frac{L\sqrt{2}}{a} \sqrt{\frac{a+b}{a+3b}} \quad (74)$$

$$\lambda_{1yh} = \frac{L\sqrt{2}}{b} \sqrt{\frac{a+b}{3a+b}} \quad (75)$$

2nd Order Octahedron Beam

For a 2nd order octahedron beam, there are four 1st order beams that are aligned with the 2nd order beam and make up the hierarchical geometry, the dimensions of which can be seen in Figure 53C. A hierarchical beam is made up of N unit cells, and in turn has a length of $L_2 = (N - 1)L/\sqrt{2}$. The $(N - 1)$ term is due to the fact that half of a hierarchical unit cell is shared with the closest neighbor. For a 2nd order hierarchical beam comprised of octahedra with solid 1st order beams, the area and area moment of inertia can be calculated to be

$$A_2 = 4\pi ab \quad (76)$$

$$I_{2x} = 4I_{1x} + 2A_1 \left(\frac{L}{2\sqrt{2}} \right)^2 = \pi ab \left(a^2 + \frac{L^2}{4} \right) \quad (77)$$

$$I_{2y} = 4I_{1y} + 2A_1 \left(\frac{L}{2} \right)^2 = \pi ab \left(b^2 + \frac{L^2}{2} \right) \quad (78)$$

From here, the slenderness ratios can be calculated to be

$$\lambda_{2x} = \sqrt{\frac{8L^2(N-1)^2}{4a^2 + L^2}} \quad (79)$$

$$\lambda_{2y} = \sqrt{\frac{4L^2(N-1)^2}{2b^2 + L^2}} \quad (80)$$

For a 2nd order hierarchical beam comprised of octahedra with hollow 1st order beams, the area and area moment of inertia can be calculated to be

$$A_{2h} = 4\pi t(a + b) \quad (81)$$

$$I_{2xh} = 4I_{1xh} + 2A_{1h} \left(\frac{L}{2\sqrt{2}} \right)^2 = \pi t \left[a^2(a + 3b) + \frac{L^2}{4}(a + b) \right] \quad (82)$$

$$I_{2yh} = 4I_{1yh} + 2A_{1h} \left(\frac{L}{2} \right)^2 = \pi t \left[b^2(3a + b) + \frac{L^2}{2}(a + b) \right] \quad (83)$$

From here, the slenderness ratios can be calculated to be

$$\lambda_{2xh} = \sqrt{\frac{8(a + b)L^2(N - 1)^2}{4a^2(a + 3b) + L^2(a + b)}} \quad (84)$$

$$\lambda_{2yh} = \sqrt{\frac{4(a + b)L^2(N - 1)^2}{2b^2(3a + b) + L^2(a + b)}} \quad (85)$$

2nd Order Octet Beam

For a 2nd order octet beam, there are eight 1st order beams that are aligned with the 2nd order beam and make up the hierarchical geometry, the dimensions of which can be seen in Figure 53D. A hierarchical beam is made up of N unit cells, and in turn has a length of $L_2 = (N - 1)L/\sqrt{2}$. The $(N - 1)$ term is due to the fact that half of a hierarchical unit cell is shared with the closest neighbor. For a 2nd order hierarchical beam comprised of octets with solid 1st order beams, the area and area moment of inertia can be calculated to be

$$A_2 = 8\pi ab \quad (86)$$

$$I_{2x} = 8I_{1x} + 2A_1 \left(\frac{L}{2\sqrt{2}} \right)^2 + 4A_1 \left(\frac{L}{\sqrt{2}} \right)^2 = \pi ab \left(2a^2 + \frac{9L^2}{4} \right) \quad (87)$$

$$I_{2y} = 8I_{1y} + 6A_1 \left(\frac{L}{2} \right)^2 = \pi ab \left(2b^2 + \frac{3L^2}{2} \right) \quad (88)$$

From here, the slenderness ratios can be calculated to be

$$\lambda_{2x} = \sqrt{\frac{16L^2(N-1)^2}{8a^2 + 9L^2}} \quad (89)$$

$$\lambda_{2y} = \sqrt{\frac{8L^2(N-1)^2}{4b^2 + 3L^2}} \quad (90)$$

For a 2nd order hierarchical beam comprised of octets with hollow 1st order beams, the area and area moment of inertia can be calculated to be

$$A_{2h} = 8\pi t(a + b) \quad (91)$$

$$I_{2xh} = 8I_{1xh} + 2A_{1h} \left(\frac{L}{2\sqrt{2}}\right)^2 + 4A_{1h} \left(\frac{L}{\sqrt{2}}\right)^2 = \pi t \left[2a^2(a + 3b) + \frac{9L^2}{4}(a + b) \right] \quad (92)$$

$$I_{2yh} = 8I_{1yh} + 6A_{1h} \left(\frac{L}{2}\right)^2 = \pi t \left[2b^2(3a + b) + \frac{3L^2}{2}(a + b) \right] \quad (93)$$

From here, the slenderness ratios can be calculated to be

$$\lambda_{2xh} = \sqrt{\frac{16(a+b)L^2(N-1)^2}{8a^2(a+3b) + 9L^2(a+b)}} \quad (94)$$

$$\lambda_{2yh} = \sqrt{\frac{8(a+b)L^2(N-1)^2}{4b^2(3a+b) + 3L^2(a+b)}} \quad (95)$$

3rd Order Octahedron Beam

For a 3rd order octahedron beam, there are sixteen 1st order beams that are aligned with the 3rd order beam and make up the hierarchical geometry, the dimensions of which can be seen in Figure 53E. A hierarchical beam is made up of N unit cells, and in turn has a length of $L_3 = (N-1)^2L/\sqrt{2}$. The $(N-1)^2$ term is due to the fact that half of a 2nd order hierarchical unit cell is shared with the closest neighbor. For a 3rd order hierarchical beam comprised of

octahedra-of-octahedra with solid 1st order beams, the area and area moment of inertia can be calculated to be

$$A_3 = 16\pi ab \quad (96)$$

$$I_{3x} = 4I_{2x} + 2A_2 \left(\frac{L(N-1)}{2\sqrt{2}} \right)^2 = \pi ab [4a^2 + L^2 + L^2(N-1)^2] \quad (97)$$

$$I_{3y} = 4I_{2y} + 2A_2 \left(\frac{L(N-1)}{2} \right)^2 = 2\pi ab [2b^2 + L^2 + L^2(N-1)^2] \quad (98)$$

From here, the slenderness ratios can be calculated to be

$$\lambda_{3x} = \sqrt{\frac{8L^2(N-1)^4}{4a^2 + L^2 + L^2(N-1)^2}} \quad (99)$$

$$\lambda_{3y} = \sqrt{\frac{4L^2(N-1)^4}{2b^2 + L^2 + L^2(N-1)^2}} \quad (100)$$

For a 3rd order hierarchical beam comprised of octahedra-of-octahedra with hollow 1st order beams, the area and area moment of inertia can be calculated to be

$$A_{3h} = 16\pi t(a+b) \quad (101)$$

$$I_{3xh} = 4I_{2xh} + 2A_{2h} \left(\frac{L(N-1)}{2\sqrt{2}} \right)^2 = \pi t [4a^2(a+3b) + L^2(a+b)(1+(N-1)^2)] \quad (102)$$

$$I_{3yh} = 4I_{2yh} + 2A_{2h} \left(\frac{L(N-1)}{2} \right)^2 = 2\pi t [2b^2(3a+b) + L^2(a+b)(1+(N-1)^2)] \quad (103)$$

From here, the slenderness ratios can be calculated to be

$$\lambda_{3xh} = \sqrt{\frac{8(a+b)L^2(N-1)^4}{4a^2(a+3b) + L^2(a+b)(1+(N-1)^2)}} \quad (104)$$

$$\lambda_{3yh} = \sqrt{\frac{4(a+b)L^2(N-1)^4}{2b^2(3a+b) + L^2(a+b)(1+(N-1)^2)}} \quad (105)$$

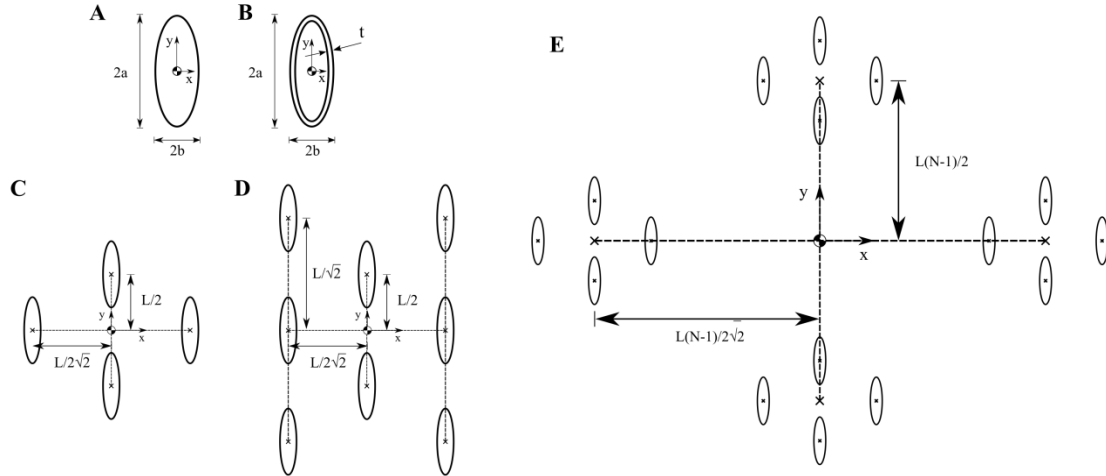


Figure 53: Hierarchical cross-sections.

A) solid 1st order beams, B) hollow 1st order beams, C) 2nd order hierarchical beams comprised of octahedra, D) 2nd order hierarchical beams comprised of octet unit cells, and E) a 3rd order hierarchical beam composed of octahedrons-of-octahedra

Appendix E. Data Tables

Unit Cell Size W (μm)	Wall Thickness t (nm)	Major Axis $2a$ (μm)	Minor Axis $2b$ (μm)	Relative Density $\bar{\rho}$	t/a	Slenderness Ratio λ	Observed Deformation Behavior	Percent Strain Recovery	Young's Modulus (MPa)	Yield Strength (MPa)
5	5	1.08	0.37	0.656%	0.007	24.2	DL	13.2%	29.9	0.60
	10	0.93	0.32	1.204%	0.016	28.0	DL	80.5%	31.7	1.00
		1.08	0.37	1.322%	0.014	24.2	DL	77.3%	29.3	1.13
	20	0.77	0.265	2.120%	0.038	33.8	ID	29.9%	90.9	3.46
		0.93	0.32	2.424%	0.031	28.0	ID	43.7%	95.5	3.63
		1.08	0.37	2.647%	0.027	24.2	ID	29.8%	130.4	4.22
		1.22	0.42	2.853%	0.024	21.3	ID	30.2%	118.6	4.09
	30	0.93	0.32	3.646%	0.047	28.0	SSB	17.2%	217.8	8.15
		1.08	0.37	3.993%	0.041	24.2	MSB	19.9%	312.2	9.25
	40	0.93	0.32	4.876%	0.063	28.0	MSB	12.7%	414.1	12.42
		1.08	0.37	5.336%	0.054	24.2	SSB	11.9%	513.5	14.20
	50	0.93	0.32	6.122%	0.078	28.0	SSB	12.3%	607.2	19.94
		1.08	0.37	6.680%	0.068	24.2	MSB	12.8%	802.1	24.05
	60	1.08	0.37	8.038%	0.081	24.2	SSB	10.0%	1136.5	32.05
1.22		0.42	8.593%	0.071	21.3	SSB	9.0%	1157.7	37.23	
10	5	1.22	0.42	0.214%	0.006	42.7	DL	75.9%	3.8	0.09
	10	1.08	0.37	0.393%	0.014	48.5	DL	44.5%	6.9	0.18
		1.22	0.42	0.435%	0.012	42.7	DL	44.8%	6.6	0.21
	20	1.08	0.37	0.788%	0.027	48.5	ID	22.8%	26.9	0.72
		1.22	0.42	0.875%	0.024	42.7	ID	25.3%	23.1	0.77
		1.37	0.47	0.958%	0.021	38.1	ID	26.0%	22.2	0.81
	30	1.22	0.42	1.323%	0.036	42.7	MSB	14.9%	56.0	1.50
		1.37	0.47	1.446%	0.032	38.1	MSB	15.9%	81.8	2.30
	40	1.08	0.37	1.605%	0.054	48.5	SSB	10.9%	106.9	2.52
		1.22	0.42	1.777%	0.048	42.7	SSB	11.6%	108.0	2.74
	50	1.08	0.37	2.017%	0.068	48.5	SSB	10.5%	148.8	3.67
		1.22	0.42	2.232%	0.060	42.7	SSB	13.5%	161.6	3.99
	60	0.93	0.32	2.178%	0.094	56.0	SSB	10.5%	202.7	3.66
		1.08	0.37	2.437%	0.081	48.5	SSB	11.2%	186.9	4.51
1.22		0.42	2.689%	0.071	42.7	SSB	10.2%	269.6	11.73	
15	10	1.92	0.66	0.300%	0.008	40.7	DL	59.9%	3.8	0.10
	20	1.92	0.66	0.604%	0.015	40.7	DL	32.7%	12.2	0.26
	30	1.75	0.6	0.839%	0.025	44.8	ID	16.5%	25.1	0.50
	40	1.75	0.6	1.130%	0.033	44.8	MSB	12.2%	51.1	0.95
	50	1.92	0.66	1.527%	0.038	40.7	MSB	12.3%	69.7	1.49
	60	1.92	0.66	1.839%	0.045	40.7	SSB	10.0%	101.9	2.16

Table 3: Hollow Al_2O_3 Octet-truss Data

List of hollow Al_2O_3 octet-truss structures fabricated, their relative densities, t/a and slenderness ratios, observed deformation behavior, percent strain recovery (final strain/maximum strain), Young's modulus, and yield strength.

Key: DL = ductile-like deformation; ID = intermittent ductile-like behavior with some bursts; MSB = multiple strain bursts; SSB = single catastrophic strain burst.

Unit Cell Size W (μm)	Wall Thickness t (nm)	Major Axis $2a$ (μm)	Major Axis $2a$ (μm)	Relative Density $\bar{\rho}$	t/a	Slenderness Ratio λ	Observed Deformation Behavior	Percent Strain Recovery	Young's Modulus (MPa)	Yield Strength (MPa)
5	10	1.22	0.42	0.774%	0.012	21.3	DL	22.0%	29.1	0.59
		1.37	0.47	0.831%	0.011	19.1	DL	30.0%	32.4	0.70
	40	1.37	0.47	3.366%	0.043	19.1	SSB	10.2%	419.3	9.22
		1.57	0.54	3.622%	0.037	16.6	MSB	10.8%	492.6	9.81
	70	1.37	0.47	5.928%	0.074	19.1	SSB	6.4%	831.2	19.67
		1.57	0.54	6.359%	0.065	16.6	SSB	7.3%	1018.5	20.43
	100	1.37	0.47	8.539%	0.106	19.1	SSB	6.5%	1817.7	38.52
		1.57	0.54	9.106%	0.093	16.6	MSB	6.2%	2076.5	39.50
8	10	1.22	0.42	0.403%	0.012	34.1	DL	61.3%	4.4	0.14
	50	1.36	0.465	1.902%	0.054	30.8	SSB	7.5%	88.9	2.04
		1.60	0.55	2.140%	0.045	26.1	SSB	9.3%	85.1	2.47
	90	1.22	0.42	3.796%	0.107	34.1	SSB	8.2%	155.6	6.17
	120	1.22	0.42	5.118%	0.143	34.1	SSB	4.5%	420.9	11.16
10	10	1.37	0.47	0.246%	0.011	38.1	DL	56.7%	3.5	0.093
	40	1.57	0.54	1.132%	0.037	33.2	MSB	8.8%	45.0	1.13
	70	1.22	0.42	1.808%	0.083	42.7	SSB	5.4%	86.8	2.39
		1.37	0.47	2.014%	0.074	38.1	SSB	5.7%	73.8	2.54
	100	1.37	0.47	2.639%	0.106	38.1	SSB	4.0%	132.5	3.67
	100	1.57	0.54	2.922%	0.093	33.2	SSB	5.3%	153.9	3.93
12	10	1.57	0.54	0.140%	0.009	39.8	DL	47.4%	2.1	0.062
	50	1.60	0.55	1.041%	0.045	39.1	MSB	9.2%	32.8	0.70
		1.81	0.6225	1.150%	0.040	34.6	MSB	9.7%	39.6	0.76
	90	1.57	0.54	1.293%	0.083	39.8	MSB	7.0%	66.5	1.86
	120	1.57	0.54	1.736%	0.111	39.8	SSB	3.7%	133.6	3.20

Table 4: Hollow Al_2O_3 Cuboctahedron Data

List of hollow Al_2O_3 cuboctahedron structures fabricated, their relative densities, t/a and slenderness ratios, observed deformation behavior, percent strain recovery (final strain/maximum strain), Young's modulus, and yield strength.

Key: DL = ductile-like deformation; MSB = multiple strain bursts; SSB = single catastrophic strain burst.

Diagonal Beam Angle	Unit Cell Size W (μm)	Wall Thickness t (nm)	Major Axis $2a$ (μm)	Minor Axis $2b$ (μm)	Relative Density $\bar{\rho}$	t/a	Slenderness Ratio λ	Observed Deformation Behavior	Percent Strain Recovery	Young's Modulus (MPa)	Yield Strength (MPa)	
45°	4	10	1.34	0.488	0.580%	0.011	17.0	DL	47.4%	8.6	0.29	
		50	1.36	0.465	2.300%	0.054	17.8	SSB	9.4%	78.8	2.53	
			1.60	0.55	2.503%	0.045	15.1	SSB	15.1%	60.1	2.78	
		90	1.34	0.488	5.252%	0.098	17.0	SSB	11.5%	212.3	9.02	
	120	1.34	0.488	7.028%	0.131	17.0	SSB	5.7%	535.5	14.04		
	6	10	1.94	0.706	0.363%	0.008	17.7	DL	64.0%	4.0	0.12	
		50	1.60	0.55	1.320%	0.045	22.6	MSB	8.2%	40.2	1.07	
			1.81	0.6225	1.429%	0.040	20.0	SSB	9.3%	37.1	1.23	
		90	1.94	0.706	3.378%	0.068	17.7	SSB	11.4%	99.3	3.19	
	120	1.94	0.706	4.524%	0.091	17.7	SSB	5.0%	232.1	6.02		
	54.7° (Regular)	3	50	1.21	0.465	2.820%	0.054	16.5	SSB	7.2%	214.9	5.67
				1.41	0.55	3.065%	0.045	14.0	SSB	8.6%	163.7	5.81
4		10	1.20	0.488	0.419%	0.011	21.1	DL	48.9%	15.3	0.31	
		50	1.21	0.465	1.766%	0.054	22.0	SSB	5.1%	138.9	2.95	
			1.41	0.55	1.966%	0.045	18.6	SSB	8.1%	112.9	3.28	
		90	1.20	0.488	3.928%	0.098	21.1	SSB	5.9%	340.3	9.16	
120		1.20	0.488	5.292%	0.131	21.1	SSB	3.3%	840.1	13.14		
5		50	1.41	0.55	1.355%	0.045	23.3	SSB	6.5%	94.4	1.92	
			1.58	0.6225	1.472%	0.040	20.6	SSB	6.0%	85.9	2.07	
6		10	1.68	0.706	0.280%	0.008	21.9	DL	71.2%	7.1	0.17	
		50	1.41	0.55	0.985%	0.045	27.9	MSB	4.6%	64.0	1.08	
			1.58	0.6225	1.081%	0.040	24.7	MSB	5.4%	60.1	1.20	
		90	1.68	0.706	2.630%	0.068	21.9	MSB	2.9%	167.9	3.12	
120		1.68	0.706	3.538%	0.091	21.9	SSB	3.9%	419.8	5.85		
65°		4	10	1.00	0.488	0.324%	0.011	29.3	DL	83.7%	23.9	0.26
			50	1.00	0.465	1.340%	0.054	30.6	SSB	3.0%	205.4	3.02
	1.15			0.55	1.490%	0.045	25.9	SSB	3.8%	193.3	3.48	
	90		1.00	0.488	3.103%	0.098	29.3	SSB	3.3%	582.1	14.95	
	120	1.00	0.488	4.208%	0.131	29.3	SSB	1.2%	3218.2	32.26		
	6	10	1.35	0.706	0.186%	0.008	30.5	DL	67.4%	11.4	0.095	
		50	1.15	0.55	0.742%	0.045	38.9	MSB	3.7%	93.5	1.14	
			1.27	0.6225	0.813%	0.040	34.4	MSB	4.6%	87.7	1.36	
		90	1.35	0.706	1.786%	0.068	30.5	SSB	3.1%	352.1	4.35	
	120	1.35	0.706	2.416%	0.091	30.5	SSB	1.1%	771.3	6.09		

Table 5: Hollow Al_2O_3 3D Kagome Data

List of hollow Al_2O_3 45°, 54.7°(regular tetrahedron), and 65° 3D Kagome structures fabricated, their relative densities, t/a and slenderness ratios, observed deformation behavior, percent strain recovery (final strain/maximum strain), Young's modulus, and yield strength.

Key: DL = ductile-like deformation; MSB = multiple strain bursts; SSB = single catastrophic strain burst.

Unit Cell Size W (μm)	Wall Thickness t (nm)	Major Axis $2a$ (μm)	Minor Axis $2b$ (μm)	Relative Density $\bar{\rho}$	t/a	Slenderness Ratio λ	Observed Deformation Behavior	Percent Strain Recovery	Young's Modulus (MPa)	Yield Strength (MPa)
5	10	0.66	0.225	0.485%	0.022	19.9	DL	59.9%	9.5	0.29
		0.80	0.275	0.570%	0.018	16.3	DL	60.5%	16.8	0.31
		0.95	0.325	0.644%	0.015	13.8	DL	56.2%	21.2	0.39
	45	0.66	0.225	2.231%	0.100	19.9	SSB	6.9%	223.3	5.03
		0.80	0.275	2.590%	0.082	16.3	MSB	6.3%	361.1	5.25
		0.95	0.325	2.921%	0.069	13.8	MSB	7.0%	394.3	6.91
		1.09	0.375	3.220%	0.060	12.0	MSB	8.0%	394.4	7.16
	90	0.66	0.225	4.822%	0.200	19.9	SSB	2.9%	754.5	12.02
		0.80	0.275	5.530%	0.164	16.3	SSB	3.7%	967.8	17.10
		0.95	0.325	6.173%	0.138	13.8	SSB	3.4%	1502.3	19.45
		1.09	0.375	6.744%	0.120	12.0	SSB	5.2%	1355.1	25.40
	10	10	0.95	0.325	0.180%	0.015	27.6	DL	49.2%	2.0
1.09			0.375	0.202%	0.013	23.9	DL	56.8%	2.3	0.079
1.24			0.425	0.220%	0.012	21.1	DL	40.1%	3.4	0.089
45		0.66	0.225	0.607%	0.100	39.8	MSB	3.9%	22.5	0.53
		0.80	0.275	0.718%	0.082	32.6	MSB	5.1%	34.2	0.79
		0.95	0.325	0.825%	0.069	27.6	MSB	5.0%	38.4	0.91
		1.09	0.375	0.928%	0.060	23.9	MSB	6.7%	46.5	1.03
90		1.24	0.425	1.028%	0.053	21.1	MSB	7.4%	57.6	1.11
		0.95	0.325	1.774%	0.138	27.6	SSB	5.2%	109.8	2.08
		1.09	0.375	1.982%	0.120	23.9	SSB	4.4%	126.6	2.48
		1.24	0.425	2.185%	0.106	21.1	SSB	4.8%	178.3	3.30
15		45	0.80	0.275	0.330%	0.082	48.9	MSB	7.6%	8.5
	0.95		0.325	0.384%	0.069	41.4	MSB	6.5%	11.2	0.28
	1.09		0.375	0.434%	0.060	35.9	MSB	5.7%	12.6	0.31
	1.24		0.425	0.484%	0.053	31.6	MSB	7.3%	14.7	0.37
	90	0.66	0.225	0.611%	0.200	59.8	MSB	4.1%	16.3	0.31
		0.80	0.275	0.719%	0.164	48.9	MSB	5.7%	20.2	0.44
		0.95	0.325	0.825%	0.138	41.4	MSB	4.3%	35.8	0.65
		1.09	0.375	0.925%	0.120	35.9	SSB	3.2%	39.7	0.80
		1.24	0.425	1.026%	0.106	31.6	SSB	2.9%	42.7	0.94

Table 6: Hollow Al_2O_3 Tetrakaidecahedron Data

List of hollow Al_2O_3 Tetrakaidecahedron structures fabricated, their relative densities, t/a and slenderness ratios, observed deformation behavior, percent strain recovery (final strain/maximum strain), Young's modulus, and yield strength.

Key: DL = ductile-like deformation; MSB = multiple strain bursts; SSB = single catastrophic strain burst.

Cell Type	Unit Cell Size L (μm)	Major Axis $2a$ (μm)	Minor Axis $2b$ (μm)	Relative Density $\bar{\rho}$	Slenderness Ratio λ	Observed Deformation Behavior	Percent Strain Recovery	Young's Modulus (MPa)	Yield Strength (MPa)
Octet-Truss	4	1.52	0.38	30.65%	29.80	D	35.6%	377.4	12.42
		1.96	0.49	46.62%	23.14	D	37.2%	882.4	28.26
		2.38	0.59	62.55%	19.04	D	41.5%	807.9	38.49
		2.90	0.73	80.30%	15.58	D	51.0%	1039.3	49.47
	6	1.52	0.38	14.90%	44.70	SB+D	42.7%	73.0	2.750
		1.96	0.49	23.48%	34.71	D	25.4%	151.3	5.227
		2.38	0.59	34.12%	28.56	D	25.2%	303.3	11.50
		2.90	0.73	45.77%	23.37	D	33.3%	578.2	22.48
	8	1.52	0.38	8.74%	59.60	SB	61.2%	36.7	1.168
		1.96	0.49	13.98%	46.28	SB	35.8%	65.2	2.348
		2.38	0.59	19.91%	38.08	SB+D	30.0%	104.4	3.811
		2.90	0.73	28.28%	31.16	D	29.9%	187.6	6.459
10	1.96	0.49	9.25%	57.85	SB	39.4%	31.1	1.043	
	2.38	0.59	13.28%	47.59	SB	32.2%	42.3	1.523	
	2.90	0.73	19.07%	38.96	SB+D	23.4%	71.4	2.757	
	1.52	0.38	16.08%	29.80	D	41.0%	106.5	3.380	
Cuboctahedron	4	1.96	0.49	24.98%	23.14	D	34.7%	237.6	8.111
		2.38	0.59	34.35%	19.04	D	34.9%	554.9	17.32
		2.90	0.73	46.41%	15.58	D	39.9%	756.1	29.37
		1.52	0.38	7.69%	44.70	SB	27.3%	32.26	1.101
	6	1.96	0.49	12.22%	34.71	SB	34.3%	48.11	1.708
		2.38	0.59	17.35%	28.56	D	59.5%	90.54	2.980
		2.90	0.73	24.40%	23.37	D	23.9%	150.0	5.405
		1.52	0.38	4.48%	59.60	SB	65.4%	12.53	0.357
	8	1.96	0.49	7.20%	46.28	SB	32.3%	17.68	0.540
		1.96	0.49	4.73%	57.85	SB	54.9%	13.01	0.369
		2.38	0.59	6.84%	47.59	SB	27.4%	16.87	0.530
		2.90	0.73	9.86%	38.96	SB	27.5%	24.79	0.784
3D Kagome	3	1.29	0.32	5.33%	37.21	SB	69.2%	32.91	1.168
		1.85	0.46	10.33%	25.93	SB+D	46.7%	54.56	1.775
		2.31	0.58	15.29%	20.75	D	39.2%	88.85	2.974
		2.79	0.70	21.04%	17.19	D	37.8%	143.3	4.976
	4	1.29	0.32	3.11%	49.61	SB	76.2%	14.18	0.371
		1.85	0.46	6.11%	34.58	SB	33.0%	18.12	0.554
		2.31	0.58	9.18%	27.67	SB+D	40.0%	28.04	0.981
		2.79	0.70	12.87%	22.92	D	36.9%	51.36	1.881
	5	1.85	0.46	4.03%	43.22	SB	33.8%	9.88	0.240
		2.31	0.58	6.12%	34.58	SB	44.7%	16.07	0.444
		2.79	0.70	8.63%	28.65	SB	39.7%	28.40	0.994
		1.85	0.46	2.85%	51.86	SB	48.8%	6.31	0.117
6	2.31	0.58	4.35%	41.50	SB	38.5%	9.51	0.207	
	2.79	0.70	6.18%	34.38	SB	41.9%	17.75	0.452	
	1.00	0.25	4.14%	28.28	SB+D	51.4%	11.41	0.458	
	1.35	0.34	8.92%	20.95	D	54.5%	35.12	1.453	
Tetrakaidecahedron	5	1.70	0.43	13.56%	16.64	D	43.2%	59.05	2.457
		2.05	0.51	18.84%	13.80	D	47.5%	107.5	4.061
		1.00	0.25	1.36%	56.57	SB	86.2%	1.71	0.087
		1.35	0.34	2.38%	41.90	SB	83.3%	5.21	0.186
	10	1.70	0.43	3.65%	33.28	SB	62.0%	8.20	0.257
		2.05	0.51	5.17%	27.59	SB	52.3%	9.49	0.306
		2.40	0.60	6.93%	23.57	SB	39.8%	18.44	0.558
		1.35	0.34	1.08%	62.85	SB	81.5%	1.33	0.041
	15	1.70	0.43	1.67%	49.91	SB	79.2%	1.33	0.041
		2.05	0.51	2.38%	41.39	SB	64.4%	2.89	0.079

Table 7: Polymer Nanolattice Data

List of solid polymer structures fabricated, their relative densities, slenderness ratios, observed deformation behavior, percent strain recovery (final strain/maximum strain), Young's modulus, and yield strength.

Key: D = densification; SB = strain bursts; SB+D = strain bursts then densification

Bar Type Removed	Percentage Removed	Relative Density	Young's Modulus (MPa)	Yield Strength (MPa)	m	n
None	0%	13.53%	58.16	1.951	-	-
Horizontal	50%	11.27%	36.34	1.012	3.09	3.03
	100%	9.02%	16.96	0.558		
Diagonal	25%	11.27%	34.18	1.014	4.26	3.81
	50%	9.02%	14.47	0.454		
	75%	6.76%	2.58	0.132		
All	17%	11.27%	36.01	1.049	3.46	3.35
	33%	9.06%	18.50	0.527		
	50%	6.76%	5.315	0.189		

Table 8: Missing Bar Polymer Octet-truss Data.

List of solid polymer octet-truss structures fabricated with randomly removed bars, their relative densities, Young's modulus, yield strength, and stiffness and strength vs density scaling coefficients m and n .

Normalized Node Offset (Offset/Beam Length)	Young's Modulus (MPa)	Yield Strength (MPa)
0.088	58.40	1.466
0.177	59.28	1.459
0.265	59.47	1.436
0.354	59.35	1.381
0.442	58.87	1.310
0.530	58.97	1.243
0.619	59.40	1.186
0.707	59.50	1.144

Table 9: Offset Node Polymer Octet-truss Data.

List of solid polymer octet-truss structures fabricated with offset-nodes, their relative densities, Young's modulus, and yield strength.

Composition	Geometry	Unit Cell Size L (μm)	Fractal Number N	Major Axis a (μm)	Relative Density	Observed Failure Mode	Young's Modulus (MPa)	Yield Strength (MPa)	H_{12}	λ_{avg}
Solid Polymer	Octahedron -of- Octahedra	8	10	0.753	1.03%	EB	1.63	0.069	1.42	30.4
		8	15	0.753	0.45%	GB	0.66	0.023	0.91	37.4
		8	20	0.753	0.25%	GB	0.38	0.009	0.67	44.4
		12	10	0.753	0.48%	1L + EB	0.64	0.018	2.11	39.4
		12	15	0.753	0.21%	EB	0.28	0.0073	1.36	46.5
		12	20	0.753	0.12%	EB + GB	0.14	0.0031	1.00	53.5
	Octahedron -of-Octets	8	10	0.753	2.10%	2L + EB	2.92	0.109	2.43	25.2
		8	15	0.753	0.95%	1L + EB/GB	1.24	0.045	1.56	29.3
		8	20	0.753	0.53%	1L + EB/GB	0.68	0.024	1.15	33.3
		12	10	0.753	0.98%	2L + EB	1.18	0.025	3.64	34.1
12		15	0.753	0.44%	2L + EB	0.45	0.011	2.34	38.2	
Composite	Octahedron -of- Octahedra	8	10	0.773	1.12%	CC	7.28	0.440	1.33	29.4
		8	15	0.773	0.49%	CC	2.97	0.137	0.86	36.4
		8	20	0.773	0.27%	PC	1.61	0.050	0.63	43.4
		12	10	0.773	0.52%	BC	2.97	0.126	1.99	37.8
		12	15	0.773	0.23%	PC	1.40	0.051	1.28	44.9
		12	20	0.773	0.13%	PC	0.79	0.021	0.94	51.9
	Octahedron -of-Octets	8	10	0.773	2.28%	CC	13.91	0.606	2.29	24.1
		8	15	0.773	1.03%	CC	5.93	0.262	1.47	28.2
		8	20	0.773	0.58%	CC	3.21	0.161	1.08	32.3
		12	10	0.773	1.07%	CC	5.61	0.180	3.43	32.5
Hollow Al_2O_3	Octahedron -of- Octahedra	8	10	0.773	0.089%	1L + CNC/EB	2.02	0.049	0.89	23.6
		8	15	0.773	0.039%	1L + CNC/EB	0.92	0.021	0.57	30.6
		8	20	0.773	0.022%	EB	0.51	0.011	0.42	37.5
		12	10	0.773	0.043%	1L + CNC	0.90	0.018	1.32	29.3
		12	15	0.773	0.019%	EB	0.44	0.008	0.85	36.3
		12	20	0.773	0.010%	EB	0.23	0.004	0.63	43.3
	Octahedron -of-Octets	8	10	0.773	0.182%	2L + CNC	2.72	0.065	1.52	18.5
		8	15	0.773	0.084%	2L + EB	1.46	0.031	0.98	22.5
		8	20	0.773	0.049%	2L + EB	0.91	0.018	0.72	26.6
		12	10	0.773	0.088%	1L + CNC	1.48	0.024	2.27	24.0
12	15	0.773	0.040%	2L + EB/CNC	0.38	0.010	1.46	28.1		
12	20	0.773	0.024%	1L + EB	0.36	0.006	1.08	32.2		

Table 10: 2nd Order Hierarchical Half-cell Data

Full list of fabricated 2nd order half-cell geometries with corresponding relative density, observed failure modes, Young's modulus, yield strength, and slenderness ratios.

Key: 1L = 1st layer collapse; 2L = 2nd layer collapse; EB = Euler buckling (1st order beams); GB = Global buckling (2nd order beams); CC = Catastrophic collapse; BC = Brittle crushing; PC = Partial collapse; CNC = Central node crushing

Composition	Unit Cell Size L (μm)	Fractal Number N	Major Axis a (μm)	Relative Density	Observed Failure Mode	Young's Modulus (MPa)	Yield Strength (MPa)	H_{12}	H_{13}	H_{23}	λ_{avg}
Solid Polymer	8	5	1.180	2.32%	EB1	3.90	0.144	3.47	9.90	2.85	17.8
	3	10	0.670	0.36%	EB2	0.34	0.014	1.05	1.74	1.66	21.4
Composite	8	5	1.025	1.83%	CC	14.48	0.487	3.97	11.39	2.87	19.7
			1.200	2.50%	CC	28.62	0.804	3.41	9.73	2.85	17.5
	3	10	0.480	0.21%	PCC+R	0.78	0.031	1.43	2.42	1.70	24.9
Hollow Al_2O_3	8	5	1.225	0.18%	1L+CNC	1.26	0.033	2.15	2.14	1.00	15.1
	3	10	0.480	0.047%	EB2	0.26	0.0078	0.92	0.89	0.97	24.1

Table 11: 3rd Order Hierarchical Half-cell Data

Full list of fabricated 3rd order octahedron half-cell geometries with corresponding relative density, observed failure modes, Young's modulus, yield strength, and slenderness ratios.

Key: 1L = 1st layer collapse; EB1 = Euler buckling (1st order beams); EB2 = Euler buckling (2nd order beams); CC = Catastrophic collapse; BC = Brittle crushing; PCC = Partial catastrophic collapse; CNC = Central node crushing.

Composition	Unit Cell Size L (μm)	Fractal Number N	Major Axis a (μm)	Relative Density	Observed Failure Mode	Young's Modulus (MPa)	Yield Strength (MPa)	H_{12}	λ_{avg}
Solid Polymer	8	10	0.733	1.03%	EB	2.47	0.100	1.51	31.7
	6	15	0.533	0.50%	GB	1.13	0.028	0.87	36.8
	4	20	0.333	0.33%	GB	1.09	0.026	0.54	41.0
Composite	8	10	0.773	1.12%	CC	11.38	0.440	1.33	29.4
	6	15	0.573	0.55%	CC	6.51	0.223	0.75	34.4
Hollow Al_2O_3	8	10	0.773	0.09%	EB + NR	0.83	0.026	0.89	23.7
	6	15	0.573	0.053%	EB + PR	0.60	0.016	0.51	29.5
	4	20	0.373	0.047%	EB + NR	0.38	0.010	0.31	34.7

Table 12: 2nd Order Hierarchical Nanolattice Data

Full list of fabricated 2nd order octahedron full-lattice geometries with corresponding relative density, observed failure modes, Young's modulus, yield strength, and slenderness ratios.

Key: EB = Euler buckling (1st order beams); GB = Global buckling (2nd order beams); CC = Catastrophic collapse; NR = No recovery; PR = Partial recovery.

Appendix F. Movies

Movie 1

In-situ video of a uniaxial compression test on a titanium nitride octahedron nanolattice unit cell. Video is played at 5 times the actual speed.

Movie 2

In-situ video of the first round of 10 cyclic compression loading cycles on a titanium nitride octahedron nanolattice unit cell. Video is played at 15 times the actual speed.

Movie 3

In-situ video of the second round of 10 cyclic compression loading cycles on a titanium nitride octahedron nanolattice unit cell. Video is played at 15 times the actual speed.

Movie 4

In-situ video of the third round of 10 cyclic compression loading cycles on a titanium nitride octahedron nanolattice unit cell. Video is played at 15 times the actual speed

Movie 5

In-situ compression video (played at 40x speed) of a thin-walled nanolattice ($5\mu\text{m}$ unit cell, 10nm wall thickness, $t/a = 0.0133$) to $\sim 40\%$ strain. Deformation is homogenous and localized to shell buckling events near the nodes. The nanolattice demonstrates an almost complete recovery after compression.

Movie 6

In-situ compression video (played at 40x speed) of a nanolattice in the transition regime between thin- and thick-walled ($5\mu\text{m}$ unit cell, 20nm wall thickness, $t/a = 0.0233$). The nanolattice is compressed to $\sim 55\%$ strain. It can be seen that strain bursts are associated with brittle failure events, and ductile-like deformation coincides with local buckling in the beams. The nanolattice partially recovers after compression.

Movie 7

In-situ compression video (played at 20x speed) of a thick-walled nanolattice ($5\mu\text{m}$ unit cell, 60nm wall thickness, $t/a = 0.0667$). There is a single strain burst event to $\sim 85\%$ strain correlating with the catastrophic failure of the nanolattice, and no subsequent recovery after compression.

Movie 8

In-situ compression experiment on an octahedron-of-octets 2nd order polymer half-cell with $L = 8\mu m$ and $N = 15$. The sample is displaced uniaxially to 50% strain at a rate of $10^{-3} s^{-1}$, and shows recovery to 85% of the original height after unloading. The sample is ductile throughout the compression experiment.

Movie 9

In-situ compression experiment on an octahedron-of-octets 2nd order core-shell ceramic-polymer composite half-cell with $L = 8\mu m$ and $N = 15$. The sample is compressed at a strain rate of $10^{-3} s^{-1}$ until the onset of brittle failure, wherein the sample catastrophically fails and demonstrates no recovery.

Movie 10

In-situ compression experiment on an octahedron-of-octets 2nd order hollow Al_2O_3 half-cell with $L = 8\mu m$ and $N = 15$. The sample is displaced uniaxially to 50% strain at a rate of $10^{-3} s^{-1}$, and shows recovery to 90% of the original height after unloading. The sample displays ductile-like behavior throughout the compression experiment with a serrated load-displacement curve.

Movie 11

In-situ compression experiment on an octahedron-of-octahedra-of-octahedra 3rd order polymer half-cell with $L = 8\mu m$ and $N = 5$. The sample is displaced uniaxially to 50% strain at a rate of $10^{-3} s^{-1}$, and shows recovery to 88% of the original height after unloading. The sample is ductile throughout the compression experiment.

Movie 12

In-situ compression experiment on an octahedron-of-octahedra-of-octahedra 3rd order core-shell ceramic-polymer composite half-cell with $L = 8\mu m$ and $N = 5$. The sample is compressed at a strain rate of $10^{-3} s^{-1}$ until the onset of brittle failure, wherein the sample catastrophically fails and demonstrates no recovery.

Movie 13

Cyclic in-situ compression experiment on an octahedron-of-octahedra-of-octahedra 3rd order hollow Al_2O_3 half-cell with $L = 8\mu m$ and $N = 5$. The sample is displaced uniaxially to 50% strain at a rate of $10^{-3} s^{-1}$, and shows recovery to 98% of the original height after unloading

during the first cycle, with nearly 100% recovery for each subsequent cycle. The sample displays ductile-like behavior throughout the compression experiment.

Movie 14

In-situ compression experiment on a polymer octet-truss nanolattice with a $L = 10\mu m$ unit cell. The sample is compressed to approximately 50% strain and shows a $\varphi_r = 83.8\%$ percent strain recovery.

Movie 15

In-situ compression experiment on a polymer cuboctahedron nanolattice with a $L = 10\mu m$ unit cell. The sample is compressed to approximately 50% strain and shows a $\varphi_r = 81.1\%$ percent strain recovery.

Movie 16

In-situ compression experiment on a polymer 3D Kagome nanolattice with a $L = 4\mu m$ unit cell. The sample is compressed to approximately 50% strain and shows a $\varphi_r = 78.7\%$ percent strain recovery.

Movie 17

In-situ compression experiment on a polymer tetrakaidecahedron nanolattice with a $L = 10\mu m$ unit cell. The sample is compressed to approximately 50% strain and shows a $\varphi_r = 72.6\%$ percent strain recovery.

Movie 18

In-situ compression experiment on a hollow Al_2O_3 octet-truss nanolattice with a $L = 10\mu m$ unit cell and $t = 10nm$ wall thickness. The sample is compressed to approximately 50% strain and shows a $\varphi_r = 76.2\%$ percent strain recovery.

Movie 19

In-situ compression experiment on a hollow Al_2O_3 cuboctahedron nanolattice with a $L = 10\mu m$ unit cell and $t = 10nm$ wall thickness. The sample is compressed to approximately 50% strain and shows a $\varphi_r = 91.3\%$ percent strain recovery.

Movie 20

In-situ compression experiment on a hollow Al_2O_3 3D Kagome nanolattice with a $L = 4\mu\text{m}$ unit cell and $t = 10\text{nm}$ wall thickness. The sample is compressed to approximately 50% strain and shows a $\varphi_r = 68.1\%$ percent strain recovery.

Movie 21

In-situ compression experiment on a hollow Al_2O_3 tetrakaidecahedron nanolattice with a $L = 10\mu\text{m}$ unit cell and $t = 10\text{nm}$ wall thickness. The sample is compressed to approximately 50% strain and shows a $\varphi_r = 91.5\%$ percent strain recovery.

References

1. M. Ashby, Designing architected materials, *Scr. Mater.* **68**, 4–7 (2013).
2. L. J. Gibson, M. F. Ashby, *Cellular Solids: Structure and Properties* (Cambridge University Press, Cambridge, ed. 2, 1999).
3. P. F. Becher, Microstructural Design of Toughened Ceramics, *J. Am. Ceram. Soc.* **74**, 255–269 (1991).
4. T. Bitzer, *Honeycomb Technology: Materials, Design, Manufacturing, Applications And Testing* (1997).
5. D. Zenkert, *An Introduction to Sandwich Construction* (Engineering Materials Advisory Services, 1995).
6. A. G. Evans, J. W. Hutchinson, N. A. Fleck, M. F. Ashby, H. N. G. Wadley, in *Progress in Materials Science*, (2001), vol. 46, pp. 309–327.
7. A. J. Jacobsen, W. Barvosa-Carter, S. Nutt, Micro-scale Truss Structures formed from Self-Propagating Photopolymer Waveguides, *Adv. Mater.* **19**, 3892–3896 (2007).
8. A. Bertsch, H. Lorenz, P. Renaud, 3D microfabrication by combining microstereolithography and thick resist UV lithography, *Sensors Actuators, A Phys.* **73**, 14–23 (1999).
9. H.-B. Sun, S. Matsuo, H. Misawa, Three-dimensional photonic crystal structures achieved with two-photon-absorption photopolymerization of resin, *Appl. Phys. Lett.* **74**, 786–788 (1999).
10. M. Campbell, D. Sharp, M. Harrison, R. Denning, A. Turberfield, Fabrication of photonic crystals for the visible spectrum by holographic lithography, *Nature* **404**, 53–6 (2000).
11. T. A. Schaedler *et al.*, Ultralight Metallic Microlattices, *Science* **334**, 962–965 (2011).
12. X. Zheng *et al.*, Ultralight, ultrastiff mechanical metamaterials, *Science* **344**, 1373–1377 (2014).
13. S. C. Han, J. W. Lee, K. Kang, A New Type of Low Density Material: Shellular, *Adv. Mater.* **27**, 5506–5511 (2015).
14. J. Bauer, S. Hengsbach, I. Tesari, R. Schwaiger, O. Kraft, High-strength cellular ceramic composites with 3D microarchitecture, *Proc. Natl. Acad. Sci.* **111**, 2453–2458 (2014).
15. L. C. Montemayor, J. R. Greer, Mechanical Response of Hollow Metallic Nanolattices: Combining Structural and Material Size Effects, *J. Appl. Mech.* **82**, 1–10 (2015).
16. J. Bauer, A. Schroer, R. Schwaiger, O. Kraft, Approaching theoretical strength in glassy carbon nanolattices, *Nat. Mater.* **8** (2016).

17. X. Wendy Gu, J. R. Greer, Ultra-strong architected Cu meso-lattices, *Extrem. Mech. Lett.* **2**, 7–14 (2015).
18. T. Bückmann *et al.*, Tailored 3D mechanical metamaterials made by dip-in direct-laser-writing optical lithography., *Adv. Mater.* **24**, 2710–4 (2012).
19. S. Krödel, T. Delpero, A. Bergamini, P. Ermanni, D. M. Kochmann, 3D Auxetic Microlattices with Independently Controllable Acoustic Band Gaps and Quasi-Static Elastic Moduli *Adv. Eng. Mater.* **16**, 1–17 (2013).
20. M. Kadic, T. Bückmann, N. Stenger, M. Thiel, M. Wegener, On the practicability of pentamode mechanical metamaterials, *Appl. Phys. Lett.* **100**, 191901 (2012).
21. T. Bückmann, M. Thiel, M. Kadic, R. Schittny, M. Wegener, An elasto-mechanical unfeelability cloak made of pentamode metamaterials., *Nat. Commun.* **5**, 4130 (2014).
22. T. Bückmann, M. Kadic, R. Schittny, M. Wegener, Mechanical metamaterials with anisotropic and negative effective mass-density tensor made from one constituent material, *Phys. Status Solidi Basic Res.* **4**, 1–4 (2015).
23. S. B. Hutchens, A. Needleman, J. R. Greer, A microstructurally motivated description of the deformation of vertically aligned carbon nanotube structures, *Appl. Phys. Lett.* **100**, 121910 (2012).
24. S. Pathak *et al.*, Higher recovery and better energy dissipation at faster strain rates in carbon nanotube bundles: an in-situ study, *ACS Nano* **6**, 2189–97 (2012).
25. A. Cao, P. L. Dickrell, W. G. Sawyer, M. N. Ghasemi-Nejhad, P. M. Ajayan, Super-compressible foamlike carbon nanotube films, *Science* **310**, 1307–10 (2005).
26. M. Mecklenburg *et al.*, Aerographite: ultra lightweight, flexible nanowall, carbon microtube material with outstanding mechanical performance., *Adv. Mater.* **24**, 3486–90 (2012).
27. B. Hatton, L. Mishchenko, S. Davis, K. H. Sandhage, J. Aizenberg, Assembly of large-area, highly ordered, crack-free inverse opal films., *Proc. Natl. Acad. Sci. U. S. A.* **107**, 10354–9 (2010).
28. J. K. Pikul, S. Ozerinc, R. Zhang, P. V. Braun, W. P. King, Micro Architected Porous Material with High Strength and Controllable Stiffness, *2016 IEEE 29th Int. Conf. Micro Electro Mech. Syst.* , 451–454 (2016).
29. N. Kröger, Prescribing diatom morphology: toward genetic engineering of biological nanomaterials., *Curr. Opin. Chem. Biol.* **11**, 662–9 (2007).
30. K. Sandhage, M. Dickerson, Novel, Bioclastic Route to Self-Assembled, 3D, Chemically Tailored Meso/Nanostructures: Shape-Preserving Reactive Conversion of Biosilica (Diatom) Microshells, *Adv. Mater.* **14**, 429–433 (2002).
31. R. Lakes, Materials with structural hierarchy, *Nature* **361**, 511–515 (1993).

32. M. Sundaram, G. Ananthasuresh, Gustave Eiffel and his optimal structures, *Resonance* **14**, 849–865 (2009).
33. R. S. Farr, Y. Mao, Fractal space frames and metamaterials for high mechanical efficiency, *EPL* **84**, 14001 (2008).
34. A. Ajdari, B. H. Jahromi, J. Papadopoulos, H. Nayeb-Hashemi, A. Vaziri, Hierarchical honeycombs with tailorable properties, *Int. J. Solids Struct.* **49**, 1413–1419 (2012).
35. R. Oftadeh, B. Haghpanah, D. Vella, A. Boudaoud, A. Vaziri, Optimal Fractal-Like Hierarchical Honeycombs, *Phys. Rev. Lett.* **113**, 104301 (2014).
36. H. N. G. Wadley, Multifunctional periodic cellular metals, *Philos. Trans. R. Soc. A* **364**, 31–68 (2006).
37. G. W. Kooistra, V. Deshpande, H. N. G. Wadley, Hierarchical Corrugated Core Sandwich Panel Concepts, *J. Appl. Mech.* **74**, 259 (2007).
38. G. Li, Y. Fang, Failure Mode Analysis and Performance Optimization of the Hierarchical Corrugated Truss Structure, *Adv. Mech. Eng.* **2014**, 1–11 (2014).
39. R. Farr, Fractal design for an efficient shell strut under gentle compressive loading, *Phys. Rev. E* **76**, 056608 (2007).
40. D. Rayneau-Kirkhope, Y. Mao, R. Farr, Ultralight fractal structures from hollow tubes, *Phys. Rev. Lett.* **109**, 2–5 (2012).
41. D. Rayneau-Kirkhope, Y. Mao, R. Farr, Optimization of fractal space frames under gentle compressive load, *Phys. Rev. E* **87**, 063204 (2013).
42. D. Rayneau-Kirkhope, Y. Mao, R. Farr, J. Segal, Hierarchical space frames for high mechanical efficiency: Fabrication and mechanical testing, *Mech. Res. Commun.* **46**, 41–46 (2012).
43. M. A. Meyers, P.-Y. Chen, A. Y.-M. Lin, Y. Seki, Biological materials: Structure and mechanical properties, *Prog. Mater. Sci.* **53**, 1–206 (2008).
44. P. Fratzl, R. Weinkamer, Nature's hierarchical materials, *Prog. Mater. Sci.* **52**, 1263–1334 (2007).
45. M. A. Meyers, J. McKittrick, P.-Y. Chen, Structural biological materials: critical mechanics-materials connections, *Science* **339**, 773–779 (2013).
46. T. R. Society, R. Society, B. Sciences, Mechanical properties of mother of pearl in tension, **196**, 443–463 (2013).
47. S. Askarinejad, N. Rahbar, J. H. Prevost, I. a Aksay, Toughening mechanisms in Bioinspired Multilayered Materials, *J. R. Soc. Interface* **12**, 20140855 (2015).
48. S. Weiner, H. D. Wagner, The material bone: structure-mechanical function relations., *Annu. Rev. Mater. Sci.* **28**, 271–298 (1998).

49. S. Kamat, X. Su, R. Ballarini, A. H. Heuer, Structural basis for the fracture toughness of the shell of the conch *Strombus gigas*, *Nature* **405**, 1036–1040 (2000).
50. W. Yang *et al.*, Natural flexible dermal armor, *Adv. Mater.* **25**, 31–48 (2013).
51. M. Sarikaya, I. A. Aksay, Nacre of abalone shell: a natural multifunctional nanolaminated ceramic-polymer composite material, *Results Probl. Cell Differ.* **19**, 1–26 (1992).
52. R. K. Nalla, J. H. Kinney, R. O. Ritchie, Mechanistic fracture criteria for the failure of human cortical bone., *Nat. Mater.* **2**, 164–168 (2003).
53. J. Aizenberg *et al.*, Skeleton of *Euplectella* sp.: structural hierarchy from the nanoscale to the macroscale., *Science* **309**, 275–278 (2005).
54. J. C. Weaver *et al.*, Hierarchical assembly of the siliceous skeletal lattice of the hexactinellid sponge *Euplectella aspergillum*, *J. Struct. Biol.* **158**, 93–106 (2007).
55. C. E. Hamm *et al.*, Architecture and material properties of diatom shells provide effective mechanical protection, *Nature* **421**, 841–843 (2003).
56. L. J. Gibson, Biomechanics of cellular solids., *J. Biomech.* **38**, 377–99 (2005).
57. Z. H. Aitken, S. Luo, S. N. Reynolds, C. Thaulow, J. R. Greer, Microstructure provides insights into evolutionary design and resilience of *Coscinodiscus* sp. frustule, *Proc. Natl. Acad. Sci.* **113**, 201519790 (2016).
58. W. Robinson, R. Goll, Fine skeletal structure of the radiolarian *Callimitra carolotae* Haeckel, *Micropaleontology* **24**, 432–439 (1978).
59. J.-Y. Kim, J. R. Greer, Tensile and compressive behavior of gold and molybdenum single crystals at the nano-scale, *Acta Mater.* **57**, 5245–5253 (2009).
60. J. R. Greer, J. T. M. De Hosson, Plasticity in small-sized metallic systems: Intrinsic versus extrinsic size effect, *Prog. Mater. Sci.* **56**, 654–724 (2011).
61. D. Jang, J. R. Greer, Transition from a strong-yet-brittle to a stronger-and-ductile state by size reduction of metallic glasses, *Nat. Mater.* **9**, 215–219 (2010).
62. D. Z. Chen *et al.*, Nanometallic glasses: size reduction brings ductility, surface state drives its extent, *Nano Lett.* **13**, 4462–4468 (2013).
63. D. Jang, L. R. Meza, F. Greer, J. R. Greer, Fabrication and deformation of three-dimensional hollow ceramic nanostructures, *Nat. Mater.* **12**, 893–898 (2013).
64. J. Bauer *et al.*, Push-to-pull tensile testing of ultra-strong nanoscale ceramic-polymer composites made by additive manufacturing, *Extrem. Mech. Lett.* **3**, 105–112 (2015).
65. H. Gao, B. Ji, I. L. Jager, E. Arzt, P. Fratzl, Materials become insensitive to flaws at nanoscale : Lessons from nature, *Proc. Natl. Acad. Sci. U. S. A.* **100**, 5597–5600 (2003).
66. H. Gao, S. Chen, Flaw Tolerance in a Thin Strip Under Tension, *J. Appl. Mech.* **72**, 732

- (2005).
67. R. Andrievski, Physical-mechanical properties of nanostructured titanium nitride, *Nanostructured Mater.* **9**, 607–610 (1997).
 68. M. Berdova *et al.*, Mechanical assessment of suspended ALD thin films by bulge and shaft-loading techniques, *Acta Mater.* **66**, 370–377 (2014).
 69. C. Yan *et al.*, Ultrahard diamond single crystals from chemical vapor deposition, *Phys. Status Solidi* **201**, R25–R27 (2004).
 70. X. Rao *et al.*, Preparation and mechanical properties of a new Zr – Al – Ti – Cu – Ni – Be bulk metallic glass, *Mater. Lett.* , 279–283 (2001).
 71. X. W. Gu, Z. Wu, Y.-W. Zhang, D. J. Srolovitz, J. R. Greer, Microstructure versus flaw: mechanisms of failure and strength in nanostructures, *Nano Lett.* **13**, 5703–5709 (2013).
 72. X. W. Gu *et al.*, Size-dependent deformation of nanocrystalline Pt nanopillars, *Nano Lett.* **12**, 6385–6392 (2012).
 73. V. S. Deshpande, M. F. Ashby, N. A. Fleck, Foam topology: bending versus stretching dominated architectures, *Acta Mater.* **49**, 1035–1040 (2001).
 74. N. A. Fleck, V. S. Deshpande, M. F. Ashby, Micro-architected materials: past, present and future, *Proc. R. Soc. A Math. Phys. Eng. Sci.* **466**, 2495–2516 (2010).
 75. R. G. Hutchinson, N. A. Fleck, The structural performance of the periodic truss, *J. Mech. Phys. Solids* **54**, 756–782 (2006).
 76. C. Tekog̃lu, L. J. Gibson, T. Pardoen, P. R. Onck, Size effects in foams: Experiments and modeling, *Prog. Mater. Sci.* **56**, 109–138 (2011).
 77. S. Pellegrino, C. R. Calladine, Matrix Analysis of Statically and Kinematically Indeterminate Frameworks, *Int. J. Solids Struct.* **22**, 409–428 (1986).
 78. V. Deshpande, Effective properties of the octet-truss lattice material, *J. Mech. Phys. Solids* **49**, 1747–1769 (2001).
 79. S. P. Timoshenko, *Theory of Elasticity* (McGraw-Hill Book Company, New York, ed. 1, 1934).
 80. S. P. Timoshenko, J. M. Gere, *Theory of Elastic Stability* (McGraw-Hill Book Company, New York, ed. 2, 1961).
 81. P. G. Sanders, J. a. Eastman, J. R. Weertman, Elastic and tensile behavior of nanocrystalline copper and palladium, *Acta Mater.* **45**, 4019–4025 (1997).
 82. R. M. Jones, *Buckling of Bars Plates and Shells* (Bull Ridge Publishing, Blacksburg, ed. 1, 2006).
 83. K. H. Law, L. Gardner, Lateral instability of elliptical hollow section beams, *Eng. Struct.*

- 37, 152–166 (2012).
84. C. Li, C. Q. Ru, A. Mioduchowski, Torsion of the central pair microtubules in eukaryotic flagella due to bending-driven lateral buckling, *Biochem. Biophys. Res. Commun.* **351**, 159–64 (2006).
 85. R. C. McCann, P. V. R. Suryanarayana, Experimental study of curvature and frictional effects on buckling, *Offshore Technol. Conf.* (1994).
 86. P. V. R. Suryanarayana, R. C. McCann, "An experimental study of buckling and post-buckling of laterally constrained rods, *J. Energy Resour. Technol.* **117**, 115–124 (1995).
 87. Y. K. Akimov, Field of Application of Aerogels (Review), *Instruments Exp. Tech.* **46**, 287–299 (2003).
 88. S. Kumar, D. E. Wolfe, M. a. Haque, Dislocation shielding and flaw tolerance in titanium nitride, *Int. J. Plast.* **27**, 739–747 (2011).
 89. J. F. Shackelford, W. Alexander, *Materials Science and Engineering Handbook* (CRC Press, Inc., Boca Raton, ed. 3, 2000).
 90. M. A. Meyers, K. K. Chawla, *Mechanical Behavior of Materials* (Prentice-Hall, Inc., New Jersey, ed. 1, 1998).
 91. H. S. Kim, M. B. Bush, The effects of grain size and porosity on the elastic modulus of nanocrystalline materials, *Nanostructured Mater.* **11**, 361–367 (1999).
 92. S. M. George, Atomic layer deposition: an overview., *Chem. Rev.* **110**, 111–31 (2010).
 93. W. D. Kingery, H. K. Bowen, D. R. Uhlmann, *Introduction to Ceramics* (John Wiley & Sons, Ney York, ed. 2nd, 1976).
 94. M. D. Groner, F. H. Fabreguette, J. W. Elam, S. M. George, Low-temperature Al₂O₃ Atomic Layer Deposition, *Chem. Mater.* **16**, 639–645 (2004).
 95. M. Ritala *et al.*, Perfectly conformal TiN and Al₂O₃ films deposited by atomic layer deposition, *Chem. Vap. Depos.* **5**, 7–9 (1999).
 96. L. R. Meza, J. R. Greer, Mechanical characterization of hollow ceramic nanolattices, *J. Mater. Sci.* **49**, 2496–2508 (2013).
 97. L. Valdevit, A. J. Jacobsen, J. R. Greer, W. B. Carter, T. M. Pollock, Ed. Protocols for the Optimal Design of Multi-Functional Cellular Structures: From Hypersonics to Micro-Architected Materials, *J. Am. Ceram. Soc.* **94**, s15–s34 (2011).
 98. H. G. Allen, P. S. Bulson, *Background to buckling* (McGraw-Hill Book Company, Berkshire, England, 1980).
 99. V. S. Deshpande, N. A. Fleck, M. F. Ashby, Effective properties of the octet-truss lattice material, *J. Mech. Phys. Solids* **49**, 1747–1769 (2001).

100. G. Ju, S. Kyriakides, Bifurcation and localization instabilities in cylindrical shells under bending—II. Predictions, *Int. J. Solids Struct.* **29**, 1143–1171 (1992).
101. A. Torrents, T. A. Schaedler, A. J. Jacobsen, W. B. Carter, L. Valdevit, Characterization of nickel-based microlattice materials with structural hierarchy from the nanometer to the millimeter scale, *Acta Mater.* **60**, 3511–3523 (2012).
102. L. Valdevit, S. W. Godfrey, T. A. Schaedler, A. J. Jacobsen, W. B. Carter, Compressive strength of hollow microlattices: Experimental characterization, modeling, and optimal design, *J. Mater. Res.* **28**, 2461–2473 (2013).
103. K. J. Maloney *et al.*, Microlattices as architected thin films: Analysis of mechanical properties and high strain elastic recovery, *APL Mater.* **1**, 022106 (2013).
104. B. Ilic, S. Krylov, H. G. Craighead, Young's modulus and density measurements of thin atomic layer deposited films using resonant nanomechanics, *J. Appl. Phys.* **108**, 1–11 (2010).
105. S.-H. Jen, J. A. Bertrand, S. M. George, Critical tensile and compressive strains for cracking of Al₂O₃ films grown by atomic layer deposition, *J. Appl. Phys.* **109**, 084305 (2011).
106. M. K. Tripp *et al.*, The mechanical properties of atomic layer deposited alumina for use in micro- and nano-electromechanical systems, *Sensors Actuators A Phys.* **130-131**, 419–429 (2006).
107. L. R. Meza, S. Das, J. R. Greer, Strong, lightweight, and recoverable three-dimensional ceramic nanolattices, *Science* **345**, 1322–1326 (2014).
108. J. C. Maxwell, On reciprocal figures and diagrams of forces, *Philos. Mag.* **4**, 250–261 (1864).
109. L. Valdevit, S. W. Godfrey, T. a. Schaedler, A. J. Jacobsen, W. B. Carter, Compressive strength of hollow microlattices: Experimental characterization, modeling, and optimal design, *J. Mater. Res.* **28**, 2461–2473 (2013).
110. V. Deshpande, Collapse of truss core sandwich beams in 3-point bending, *Int. J. Solids Struct.* **38**, 6275–6305 (2001).